University of Bayreuth – Micrometeorology & Disturbance ecology

Master Thesis

Late-frost limitation of European beech in the Fichtelgebirge mid-range mountains, Germany

Judith Eisenbacher

Student number: 1583330

supervised by

Prof. Dr. Christoph Thomas

Prof. Dr. Anke Jentsch

Bayreuth, March 29, 2021

Abstract

For the last two hundred years, the forestry sector in Central Europe has largely relied on Norway spruce (*Picea abies* (L.) Karst.). In the face of climate warming, though, the meteorological conditions in Central Europe are changing, causing spruce die-off due to drought stress and insect outbreaks. Tree species composition in Central Europe's forests will have to change, with European beech (*Fagus sylvatica* L.) being a promising alternative, as it constitutes the potential natural vegetation of most of Central Europe's land area. However, at the higher altitudes of mid-range mountains, beech is currently deemed to be limited by spring late frost events, deterring foresters from endeavors to diversify the spruce forests in these areas. This thesis aims at determining whether beech is currently late-frost limited at the summit of Schneeberg, the highest summit of Fichtelgebirge mountains with an elevation of 1051 m above sea level, and at assessing whether special sites such as block fields influence the microclimate of their surroundings, mitigating frost events and thereby enabling beech growth in high altitudes. Mobile air and surface temperature measurements were conducted during four late-frost events in spring 2019 near the summit of Schneeberg in the proximity of a granitic block field. Additionally, stationary air temperature measurements allowed for a comparison of the Schneeberg temperature regime to lower-elevation, beech-covered sites at Buchberg and Rauher Kulm, with the latter representing a second block field study area. Neither of the two investigated block fields exhibited the cold-air drainage flow and air temperature inversion typical for such sites, probably because they were too small for the expected microclimate to develop. The block field at Schneeberg was the warmest part of the summit area during night, but did not alleviate the frost temperatures in the surrounding forest up to the investigated distance of 50 m from the edge of the block field. The lowest air temperatures were found at the locations of the only four beech trees growing in the vicinity of the block field. It is concluded that the block field neither positively nor negatively affects the survival of beech at Schneeberg summit, and that beech is currently not late-frost limited in the Fichtelgebirge mountain range.

Zusammenfassung

In den letzten zweihundert Jahren hat die Forstwirtschaft in Mitteleuropa weitgehend auf der Fichte (*Picea abies* (L.) Karst.) basiert. Im Zuge der Klimaerwärmung verändern sich die meteorologischen Bedingungen in Mitteleuropa jedoch zu Ungunsten der Fichte, welche zunehmend aufgrund von Trockenstress und Insektenbefall abstirbt. Die Baumartenzusammensetzung in den Wäldern Mitteleuropas wird sich ändern müssen, wobei die Rotbuche (*Fagus sylvatica* L.) eine vielversprechende Alternative darstellt, da sie die potenzielle natürliche Vegetation des größten Teils der mitteleuropäischen Landfläche ausmacht. In den höheren Lagen der Mittelgebirge gilt die Buche jedoch derzeit als durch Spätfrostereignisse im Frühjahr limitiert, was die Förster von Bemühungen abhält, die Fichtenwälder in diesen Gebieten zu diversifizieren. Ziel dieser Arbeit ist es, festzustellen, ob die Buche am Gipfel des Schneebergs, der mit 1051 m über dem Meeresspiegel höchsten Erhebung des Fichtelgebirges, derzeit spätfrostlimitiert ist und ob Sonderstandorte wie zum Beispiel Blockhalden das Mikroklima ihrer Umgebung dahingehend beeinflussen, dass sie Frostereignisse abmildern und damit das Wachstum der Buche in hohen Lagen ermöglichen. Mobile Luft- und Oberflächentemperaturmessungen wurden während vier Spätfrostereignissen im Frühjahr 2019 in Gipfelnähe des Schneebergs in der Umgebung einer granitischen Blockhalde durchgeführt. Zusätzlich ermöglichten stationäre Lufttemperaturmessungen einen Vergleich des Schneeberg-Temperaturregimes mit den tiefer gelegenen, buchendominierten Standorten am Buchberg und Rauhen Kulm, wobei letzterer ein zweites Blockhalden-Untersuchungsgebiet darstellt. Keine der beiden untersuchten Blockhalden wies die für solche Standorte typischen Kaltluftabflussströmungen und Lufttemperaturinversionen auf, vermutlich da die Blockhaldenfläche nicht für eine Entwicklung des erwarteten Mikroklimas ausreichte. Die Blockhalde am Schneeberg war in der Nacht der wärmste Teil des Gipfelbereichs, milderte aber die Frosttemperaturen im umgebenden Wald bis zur untersuchten Distanz von 50 m, gemessen vom Rand der Blockhalde, nicht ab. Die kältesten Lufttemperaturen wurden an den Standorten der einzigen vier Buchen gefunden, die in der Nähe der Blockhalde wachsen. Es wird gefolgert, dass die Blockhalde das Überleben der Buche am Schneeberggipfel weder positiv noch negativ beeinflusst und dass die Buche im Fichtelgebirge derzeit nicht spätfrostlimitiert ist.

Contents

List of Figures

List of Tables

List of abbreviations and symbols

a.s.l.	above sea level
BBCH	Biologische Bundesanstalt, Bundessortenamt und Chemische Indsturie
GPS	Global Positioning System
Habitats Directive	Council Directive 92/43/EEC on the Conservation of Natural Habitats and of Wild Fauna and Flora
IR	infrared
MRD	multiresolution decomposition
MSA	micro sonic anemometer
MTH	mobile thermohygrometer
RCP	Representative Concentration Pathway
SAC	Special Area of Conservation
STH	stationary thermohygrometer

symbol	explanation	unit
D_T	mean spectrum density	(-)
f	frequency	(s^{-1})
$I\uparrow$	outgoing longwave radiation	($W\,m^{-2}$)
$I\downarrow$	incoming longwave radiation	($W\,m^{-2}$)
$K\uparrow$	reflected shortwave radiation	($W\,m^{-2}$)
$K\downarrow$	global radiation	($W\,m^{-2}$)
m	multiresolution decomposition mode	(-)
M	highest multiresolution decomposition mode	(-)
p	air pressure	(hPa)
p_0	air pressure at sea level	(hPa)
Q_S^*	net radiation	($W\,m^{-2}$)
R^2	square of the Pearson correlation coefficient	(-)
R_T	spatial two-point correlation coefficient (air temperature)	(-)
S	radiant emittance	($W\,m^{-2}$)
T_{air}	air temperature	(°C)
T_{Fi}	air temperature measured by stationary thermohygrometer at location Fi (with $i = 1, ..., 8$)	(°C)
T_{IR}	surface brightness temperature measured by infrared camera	(°C)

symbol	explanation	unit
T_{min}	minimum temperature	(°C)
T_{MTH}	air temperature measured by mobile thermohygrometer	(°C)
$T_{pixel_{x,y}}$	surface brightness temperature at pixel x,y	(°C)
$T_{surface}$	surface brightness temperature	(°C)
$T_{Thermocouple}$	temperature measured by Thermocouple type K sensor of mobile thermohygrometer	(°C)
z	elevation	(m)
z_0	reference elevation	(m)
γ	atmospheric temperature gradient	($\mathrm{K\,m^{-1}}$)
ΔT	temperature difference	(K)
ϵ	emissivity	(-)
Θ	potential temperature	(°C)
κ_L	Poisson constant	(-)
σ_{SB}	Stefan-Boltzmann constant	($\mathrm{W\,m^{-2}\,K^{-4}}$)
σ_T	standard deviation of temperature	(K)
σ_T^2	variance of temperature	($\mathrm{K^2}$)

1. Introduction

1.1. Background

The European beech (*Fagus sylvatica* L., subsequently referred to as beech) is one of the ecologically and economically most important tree species of the temperate forests of Central Europe (Bradshaw and Holmqvist, 1999; Dierschke and Bohn, 2004, Ellenberg, 1996, chap. A I 1). For one, it has a wide physiological as well as ecological acidity and medium soil moisture optimum, enabling it to inhabit a wide range of sites as a climax species (Ellenberg, 1996, chap. B I 2 b). For another, it is extremely shade-tolerant as a sapling, being able to survive in the deep shade induced by mature individuals that causes higher mortalities in competitor species (Petritan et al., 2007). Thus, it often reaches more than 90 % canopy cover (Dierschke and Bohn, 2004) and beech forests make up 74 % of Central Europe's potential natural forest vegetation, only omitting extremely dry, wet, acidic and cold sites as well as sites like block fields which are prone to ground movements; though currently, beech forests only cover 14.8 % of Germany's woodland area (Moning and Müller, 2009). This reduction results from an intensive deforestation and overexploitation of forests until the 19^{th} century and subsequent reforestation with fast-growing coniferous tree species (Spiecker et al., 2004). The distribution area of beech ranges from southern Scandinavia in the north to eastern Poland in the east and to Italy and Greece in the south, with inhabited elevations increasing from north to south (Dierschke and Bohn, 2004). Its elevational limit at the center of its distribution is at approximately 1000 m above sea level (a.s.l.), where it is replaced by Norway spruce (*Picea abies* (L.) Karst., subsequently referred to as spruce) and fir (*Abies alba* Mill.).
In the face of climate change with a predicted warming between 1.0 ± 0.7 K and 3.7 ± 1.1 K (Representative Concentration Pathway; RCP; 2.6–8.5) relative to 1986–2005 (IPCC, 2013), beeches might be able to inhabit significantly higher elevated sites within just one century. With a mean ambient lapse rate of 0.65 K per 100 m of elevation, the worst-case prediction with a warming of 3.7 K could equate to approximately 570 m of ascending distribution limits. Similarly, the lower elevational limit of spruce is also rising due to increasing soil water deficits during spring and summer stemming from an increased vapor pressure deficit caused by high air temperature T_{air}, especially near the surface, and often coinciding low precipitation sums (Vospernik and Nothdurft, 2018), resulting in reduced productivity of spruce at lower sites, which is already visible (Kölling et al., 2007). During the last few decades, bark beetle (*Ips typographus* L.) outbreaks increasing in frequency and magnitude have caused considerable disturbances to spruce forests, especially those located at lower elevations where T_{air} is higher (Marini et al., 2012). With near-surface T_{air} rising and dry summers becoming more frequent, climatic conditions will be favorable to bark beetle development, causing outbreaks to reach higher elevations (Marini et al., 2012; Mezei et al., 2017). In the light of increasing future risk

in cultivation of spruce (Kölling et al., 2007), it is imperative for the forestry sector to adapt species compositions to future conditions. Considering beech's optimal harvesting rotation age is 120 to 140 years (Hofmeister, 2004, p. 249), these adaptations should already be started now. Even near beech's cold distribution limit, where its plantation is not yet considered, forest rejuvenation with young beeches should be encouraged wherever possible, for this area will probably be further inside the ecological tolerance range of beech in a few decades. Then, as soon as climate is less favorable to spruce at these sites, there will be already mature individuals of beech to establish a seedling bank and compensate the deficit caused by withdrawing spruce.

The current limiting factor at higher elevations is the minimum temperature T_{min}, especially during the period of bud break, whereas winter T_{min} and growing-season mean T_{air} are probably not relevant for the distribution limit (Kollas et al., 2014). In the phase of de- and re-allocation of resources, which equals to bud break and leaf fall, trees are especially sensitive to frost. The only partially developed leaves can already be killed by T_{air} of $-2.0\,°C$ (Kadereit et al., 2014, chap. 27.3.1) to $-3.0\,°C$ (Till, 1956). Other studies (Hofmann and Bruelheide, 2015; Vitasse et al., 2014) reported lower minimum T_{air} necessary for damaging leaf tissue; however, since the duration of the artificial frost events ranged from 45 min to 4 h and the phenological stages of the leaves differed between studies, no universal assertions can be made regarding the exact T_{air} and duration of frost necessary for leaf damage. Small trees in particular are prone to late frost events (Ningre and Colin, 2007), with minimum T_{air} usually occurring close to the ground whenever the canopy cover is low. This low T_{air} near the ground is caused by high ground outgoing longwave radiation $I\uparrow$ (positive sign) in combination with low sky incoming longwave radiation $I\downarrow$ (negative sign) leading to a large positive longwave radiation balance at night, which means a net radiation loss (Jordan and Smith, 1995), since the shortwave incoming and reflected radiation, $K\downarrow$ and $K\uparrow$, respectively, both equal $0\,W\,m^{-2}$ during the night (Eq. 1.1).

$$Q_S^* = K\downarrow + K\uparrow + I\downarrow + I\uparrow \tag{1.1}$$

Under a dense canopy, however, T_{air} is usually more moderate during the night due to the strongest radiational cooling taking place in the canopy instead of near the ground (Vickers and Thomas, 2014) and a larger $I\downarrow$ reducing the positive longwave radiation balance, thus mitigating frost damage (Bianchi et al., 2019; Negi et al., 1996). Local adaptations to late frosts are possible, mainly by delaying bud break (Kreyling et al., 2014), but juvenile trees open their buds significantly earlier than mature trees in order to receive almost full sunlight before they are shaded by the crown (Augspurger and Bartlett, 2003). Thus, saplings are most affected by late frost effects (Vitasse et al., 2014), which can include bud damage (Liepe, 1993), forking (Ningre and Colin, 2007), a reduction of canopy density by up to 50 % despite refoliation (Augspurger, 2009) and reduced radial growth by more than 90 % (Dittmar et al., 2006).

Whether damage due to late frost will increase or decrease with ongoing climate change is currently still under debate and depends on the probability of late frost events in combination with changes in tree phenology. Despite near-surface T_{air} rising globally, cold extremes are likely to persist in their current intensity and duration in many regions when viewed as global total, with only their frequency varying regionally (Kodra et al., 2011). Therefore, the future

development of late frost events is most sensitive to changes in the timing of leaf-out (Cannell and Smith, 1986). This timing in turn depends on the chilling time, thermal or forcing time and photoperiodic requirements of the species. Murray et al. (1989) defined chilling as the number of days with T_{air} <5.0 °C since November 1 and thermal time as the number of days with T_{air} >5.0 °C since January 1. Most plants in temperate climates need a specific chilling time followed by a specific thermal time to initiate bud burst in spring, with the two being interconnected: With accumulating chilling days the subsequently required thermal time decreases until it reaches a minimum value when the buds are fully chilled (Caffarra and Donnelly, 2011; Cannell and Smith, 1986). Climate change is likely to affect both: chilling requirements will be met later, while the temperature sums necessary for bud burst will be reached earlier (Kramer, 1994). Therefore, depending on the exact circumstances of tree growth and the requirements of the species, studies come to different conclusions on future late frost damage risk: Cannell and Smith (1986) as well as Hänninen (1991) found frost damage to increase due to high T_{air} in early spring causing earlier bud burst. Leinonen (1996) described a similar effect on Scots pine (*Pinus sylvestris* L.), while according to Fisichelli et al. (2014) earlier leaf-out increased the mortality of broadleaf trees but not of conifers.

On the other hand, Kramer (1994) found T_{min} at the time of bud burst to be higher or constant, causing frost damage risk to decrease. Murray et al. (1989) and Guo et al. (2019) came to similar results, stating that thermal time increased greatly with decreased chilling for beech and apple (*Malus pumila var. domestica* C.K. Schneid.), causing phenology to stay the same or even be delayed. Additionally, bud burst of beech is co-controlled photoperiodically, with shorter photoperiod increasing the thermal time in order to avoid flushing too early (Fu et al., 2019; Heide, 1993; Lenz et al., 2016). Vander Mijnsbrugge et al. (2016) furthermore found summer drought to delay bud burst in the following spring, probably a carry-over effect from delayed senescence in fall to compensate for lost growth time. With droughts likely to increase in intensity and duration as a consequence of climate change (medium confidence; IPCC, 2013), this effect might gain importance in the future, though according to Čehulić et al. (2019), droughts in two subsequent years had opposite effects on the timing of bud burst. Moreover, frost risk can depend on elevation, with forests >800 m a.s.l. in Central Europe at an increased risk, while lower sites do not exhibit any trend (Vitasse et al., 2018). Assessing the frost risk in combination with the timing of leaf-out is further complicated by the fact that older, mature leaves are more frost-resistant than young, newly sprouted leaves (Kadereit et al., 2014, chap. 27.3.1, Menzel et al., 2015). Plants with an earlier leaf-out can therefore even be at an advantage. Additionally, the frost-resistance of an individual depends on water and nutrient supply, with individuals used to drought and individuals with a perfect nutrient availability being more resistant (Kadereit et al., 2014, chap. 27.3.1).

After a late frost event that damaged the leaves, despite not having many dormant buds, beech canopies can recover (Nolè et al., 2018; Zohner et al., 2019). The second greening is initiated especially fast in individuals that started sprouting early in spring during the first flushing period (Menzel et al., 2015). With refoliation in combination with delayed fall senescence, beech is able to compensate ∼30 % of the deficit in growing-season length (Zohner et al., 2019). The stress caused to a plant by a frost event can lead to acclimatization with subsequent

leaves being less frost-sensitive, provided the plant survived the event (Kadereit et al., 2014, chap. 26.2). Beeches' radial growth exhibits low resistance but high resilience to frost damage with no carry-over effects into subsequent years (Príncipe et al., 2017).

Despite all uncertainties concerning the future development of the importance of late frost, it is clear that late frost risk is currently a vital factor for the distribution and survival of broadleaf trees. Since species are especially sensitive to climate near their distribution limit (Farahat and Linderholm, 2018), in these areas sites with a special microclimate might enable extrazonal tree growth in places where large-scale or local climate is limiting. Such special sites can be steep slopes, pure rock or coarse blocky deposits (subsequently called block fields), where competition between adult trees and juveniles might be reduced due to the missing canopy cover, enabling the saplings to receive more light, water and nutrients (Ammer et al., 2008). In addition to the reduced canopy cover, the microclimate of block fields has many exceptional properties with complex interactions of slope, season, time of day, wind and snow conditions, which facilitate studying various climatic conditions in a small area.

In winter, four scenarios are possible: When there is little to no snow cover, cold, dense air descends into the voids between the blocks and freezes water coming from rainfall or snow melt, the so-called Balch effect (Balch, 1900, chap. II; Fig. 1.1 a). However, in strong-wind conditions, T_{air} in the voids rapidly adjusts to the changing T_{air} in the atmosphere down to a considerable depth beneath the block surface (Harris and Pedersen, 1998; Fig. 1.1 b). On the other hand, a thick snow cover prevents the voids from freezing (Růžička et al., 2012) and induces the chimney effect first described by Wakonigg (1996): Small holes in the snow cover allow cold air to enter, replacing the warmer air inside, which rises in between the blocks and escapes through similar holes further up the slope (Fig. 1.1 c). This effect can be large enough to keep the upper end of the slope frost-free all year (Růžička et al., 2012). However, when boulders protrude the snow cover due to strong winds blowing the snow away from the tops of the boulders, the rock acts as a thermal bridge because of its high heat conductivity, increasing the ground cooling (Davesne et al., 2017; Fig. 1.1 d). The ground cooling is further enhanced by the protruding boulders' high surface roughness, as the turbulent heat fluxes are proportional to surface roughness (Davesne et al., 2017). Therefore, while strong winds might prevent the voids from freezing permanently when snow cover is missing, they reduce the insulating effect of a snow cover that is present.

During spring, snow meltwater can refreeze due to the low temperatures between the blocks (Balch, 1900, chap. II, Zacharda et al., 2007) and lead to an increase of the internal block field T_{air} due to the release of latent heat in the process (Zacharda et al., 2007). The chimney effect now works in reverse: cold air still present between blocks sinks downslope through the voids and escapes the bottom of the block field when the melting snow cover no longer prevents it, enabling warmer air to slowly replace it from the top to the bottom (Harris and Pedersen, 1998). In summary, air flow on hill slopes with rocky deposits is mostly comprised of katabic flow during the warm season and anabatic flow during the cold season (Popescu et al., 2017).

If ice has formed in the interior of the voids, it can melt during spring, causing a continuous cold-air seepage at the bottom of the block field (Růžička et al., 2012) due to latent heat being consumed by melting or sublimation of ice and subsequent evaporation (Růžička et al.,

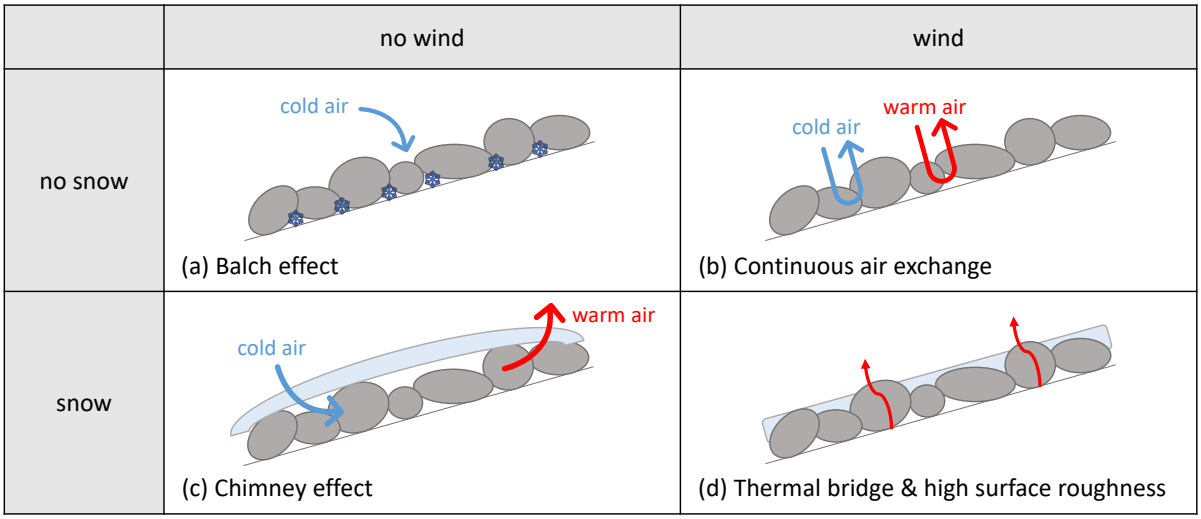

Figure 1.1.: Schematic of common micrometeorological processes near block fields during winter, depending on snow cover and wind.

2015; Wakonigg, 1996). Not all of the ice necessarily melts, though; Popescu et al. (2017) found permafrost at an elevation of ∼1100 m in the Western Romanian Carpathians and both Zacharda et al. (2007) and Stiegler et al. (2014) found ice to be able to persist year-round under blocky material in Central Europe even <1000 m a.s.l., far below the regional limits of mountain permafrost, which lie at ∼2300 m a.s.l. in the Bavarian Alps according to Gude and Barsch (2005) and in the Alps in general at ∼2000 m a.s.l. (Boeckli et al., 2012). It is therefore unclear whether year-round ice can be found in Bavarian mid-range mountains like Fichtelgebirge with its highest peaks at ∼1000 m a.s.l.

The diurnal cycle is characterized by a high solar insolation during daytime because of the missing plant cover, while at night, the high $I\uparrow$ of the block field in combination with low $I\downarrow$ under clear-sky conditions leads to radiative cooling (Kotzé and Meiklejohn, 2017) with cold air pooling close to the ground under weak-wind conditions with stable atmospheric stratification, creating an inversion (Dobrowski, 2011). On steeper slopes, cold air can flow downhill through the voids, enhancing the inversion.

The cold-air seepage at the base of the block field keeps T_{air} low for a long time in spring and summer, creating an extrazonal micro-habitat for the characteristic cold flora of the sub-alpine, boreal and arctic (Dobrowski, 2011; Harris and Pedersen, 1998; Růžička et al., 2015). However, it is as yet unclear whether warm air exhalations at the top of the slope in combination with cold air being drained might have an opposite effect on the upper part of the block field and the area above, enabling more thermophilic, late-frost limited plants like beeches to survive outside of their usual distribution limits.

1.2. Objectives of the thesis

In this thesis, I aim to determine

a) whether beeches are currently late-frost limited at the summit of Schneeberg, whose elevation of 1051 m a.s.l. makes it the highest mountain of Fichtelgebirge, or if and where it would

be possible to increase forest biodiversity by sowing or planting beeches. For this purpose, I will quantify small-scale T_{air} differences at Schneeberg and compare them to large-scale elevation-driven differences to other study sites at Rauher Kulm and Buchberg, and

b) I intend to assess whether special sites such as block fields influence the microclimate of their surroundings due to their exceptional energy and radiation budget, systematically affecting beech rejuvenation. For this, I want to quantify small-scale T_{air} and longwave radiation intensity differences between locations with beeches, open terrain without beeches and block field locations.

1.3. Hypotheses

Based on the objectives and the literature research, the following hypotheses were conceived for time periods with an absence of strong synoptic forcing, when microclimate is expected to be an important driver:

I a) *Small-scale spatial T_{air} differences exceed large-scale, elevation-driven differences in magnitude during nighttime.*
This hypothesis is expected due to the influence of block fields on the microclimate.

I b) *T_{air} at the warmest locations at Schneeberg summit is equal to or higher than T_{air} at the coldest locations at beech-covered reference sites during late frost events.*
This hypothesis follows from I a) and implies that beeches are currently not late-frost limited at the warmest locations of the Schneeberg summit area.

II a) *At night, the block fields cool down further than forested areas.*
This hypothesis is expected due to a strong net radiation loss at the block field stemming from the block field's high thermal conductivity and high longwave emissivity in combination with low $I\downarrow$ because of the missing canopy cover.

II b) *Nighttime T_{air} at the top of the block field is higher than at the bottom of the block field in absence of high wind speeds.*
This inversion is expected due to cold-air drainage between the blocks and pooling near the bottom, especially in ground depressions.

2. Methods

2.1. Locations

The main study site was located at the summit of Schneeberg (50.0524° N, 11.8539° E) in the Fichtelgebirge mid-range mountains in south-eastern Germany (Fig. 2.1). With 1051 m a.s.l., it is the highest elevation of Fichtelgebirge mountains. The summit area was used by the German military until the end of the cold war, keeping the plateau treeless. A micrometeorological weather station (type WS-GP1, Delta-T, Umweltanalytische Produkte GmbH, Ibbenbüren, Germany) was installed on the roof of a former military building at the summit (Fig. 2.2), recording T_{air} and humidity, wind direction and speed as well as short-wave radiation and precipitation since June 2016 at a resolution of 10 min.

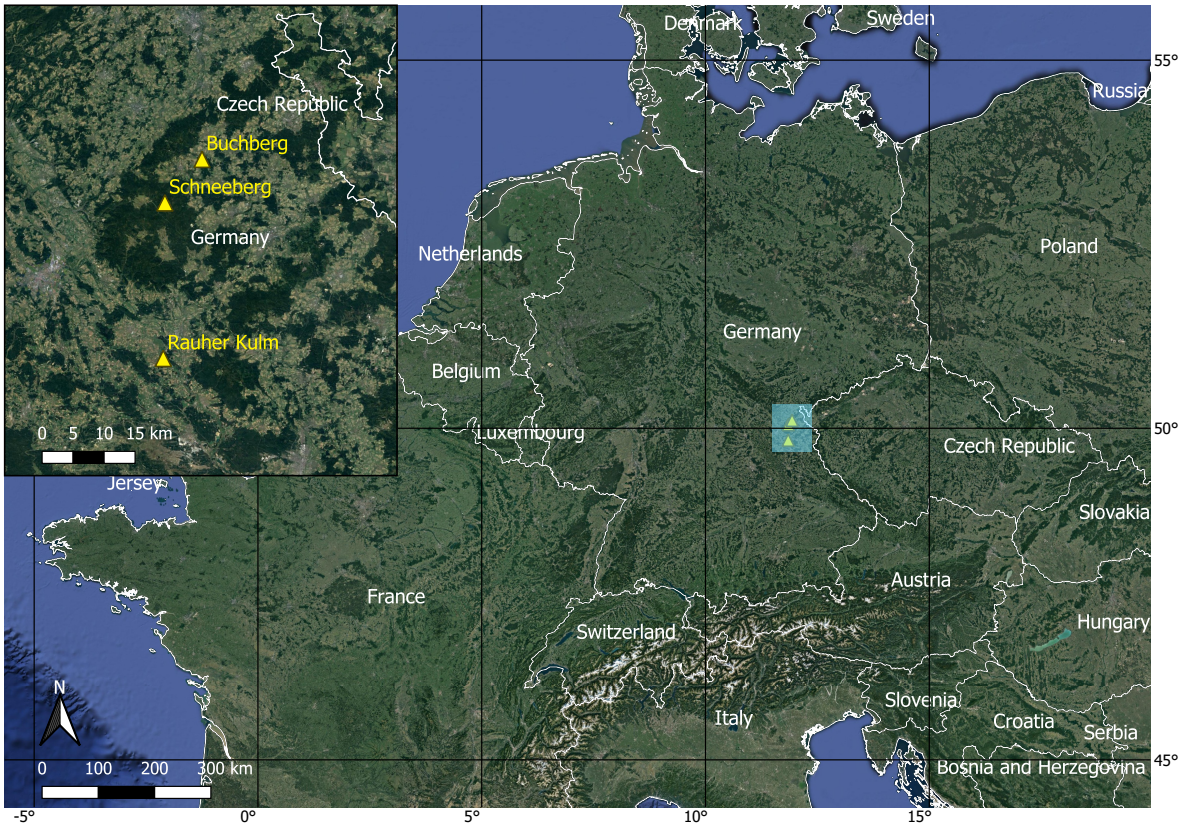

Figure 2.1.: Map of Central Europe with study sites. (Base map: Image Landsat/Copernicus, © 2021 Google, US Dept of State Geographer, © 2021 GeoBasis-DE/BKG. Country borders: © 2018 GADM)

The plateau at the top of Schneeberg consists of open grassland interspersed with small anthropogenic block heaps that were created for nature conservation purposes. The surrounding

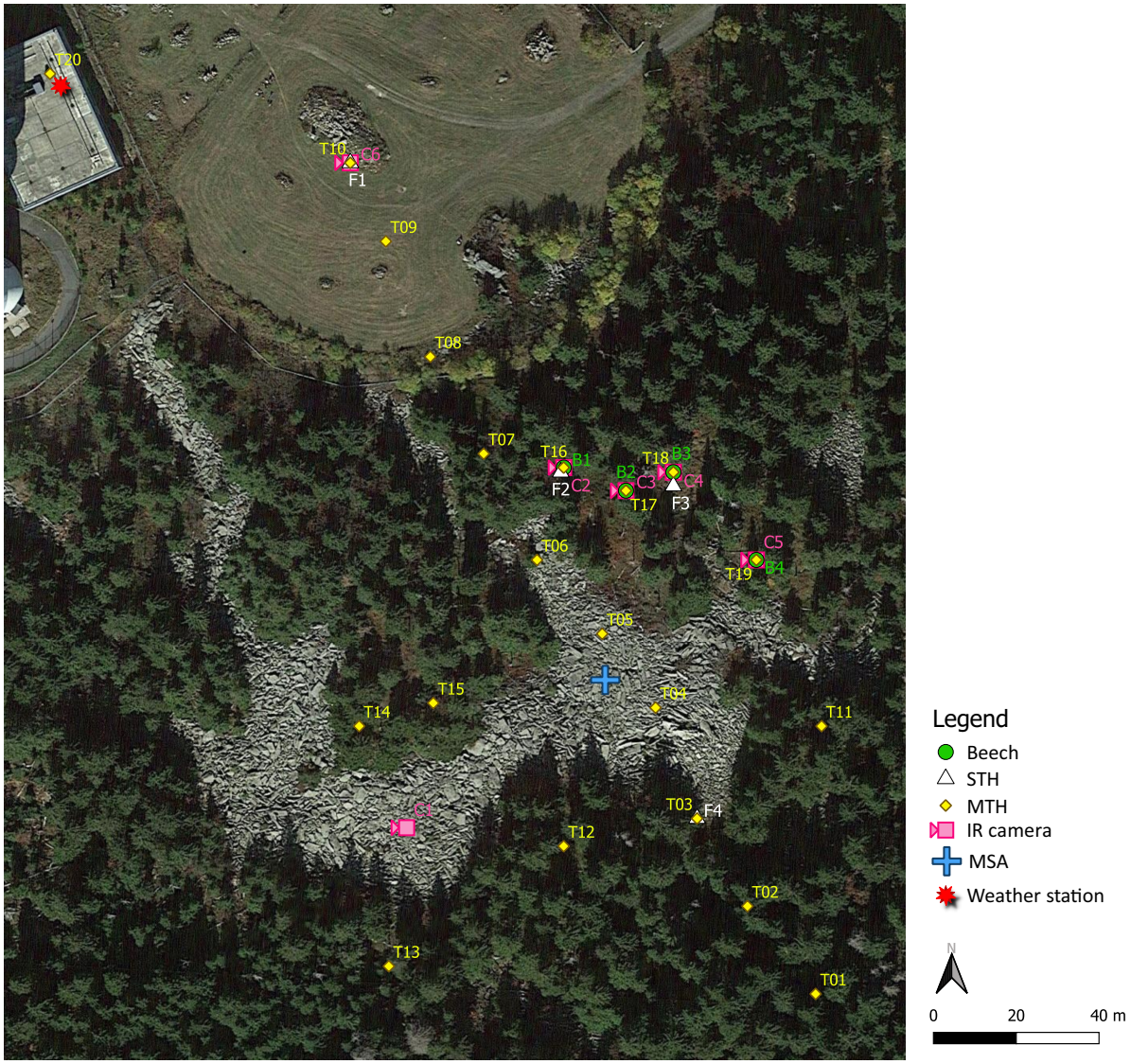

Figure 2.2.: Map of the Schneeberg site with measuring locations of the stationary thermohygrometers (STHs), the mobile thermohygrometer (MTH), the infrared (IR) camera, the micro sonic anemometer (MSA), the weather station and beeches B1 to B4. The summit is located in the top left corner of the map. (Base map: © 2021 Google, © 2021 GeoBasis-DE/BKG)

forest is mainly comprised of spruce and occasional mountain ash (*Sorbus aucuparia* L.) with only few beech saplings near the summit. Directly south of the summit, a granite block field with an area of ∼0.5 ha is located. The blocks have a diameter range of up to several meters. Due to its high plant biodiversity and its function as a habitat and breeding area for capercaillie (*Tetrao urogallus* L.; Hertel, 2009), the summit and parts of the southern flank were appointed as nature conservation area as well as Special Area of Conservation (SAC) under the Council Directive 92/43/EEC on the Conservation of Natural Habitats and of Wild Fauna and Flora (Habitats Directive). Approximately 200 m in elevation lower, near the northern access road, several small beech rejuvenation areas were planted (Fig. 2.3), adding to a larger, older beech area at the southern flank of the mountain.

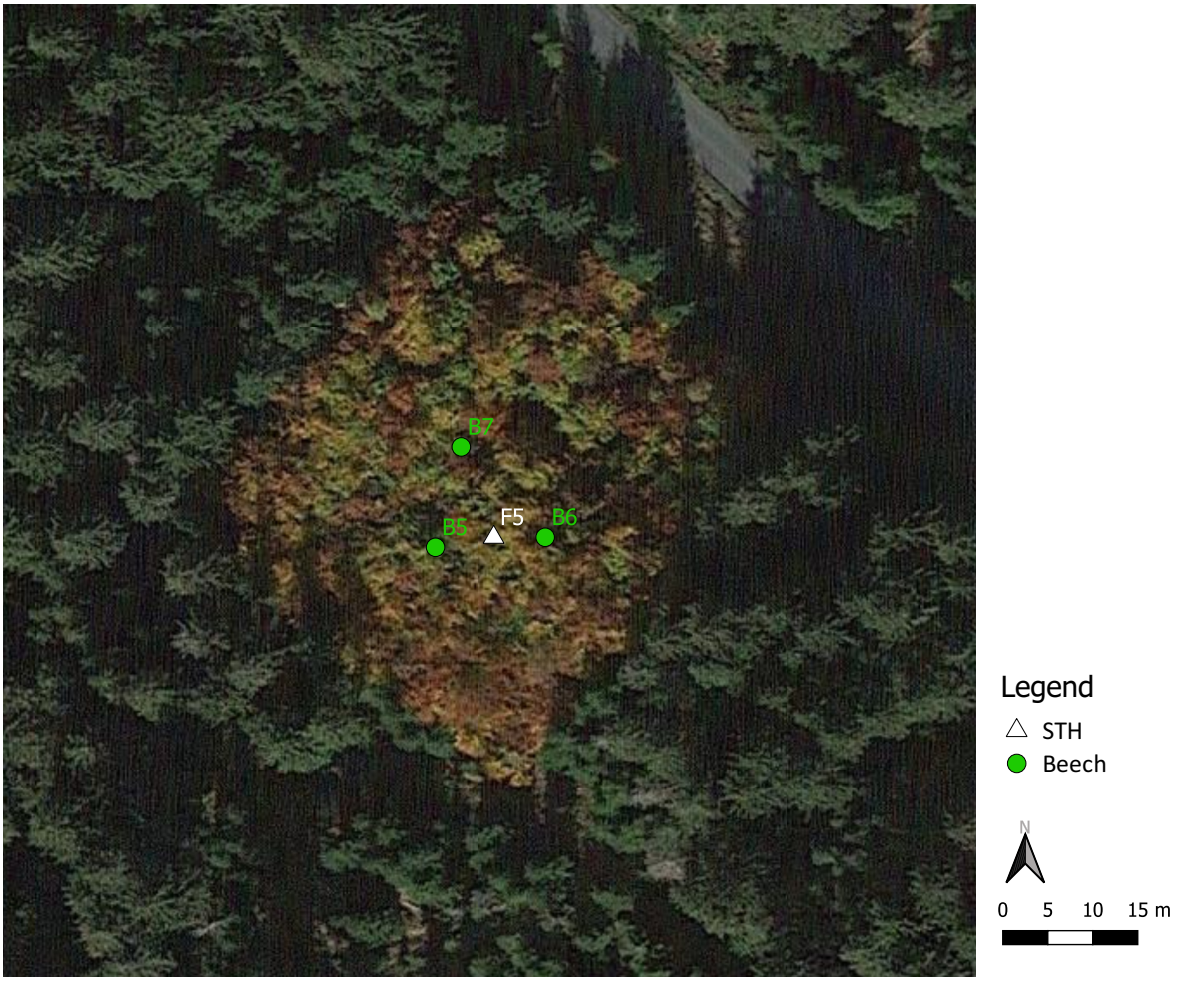

Figure 2.3.: Map of Schneeberg beech plantation with location of installed stationary thermohygrometer (STH) and beeches B5 to B7. (Base map: © 2021 Google, © 2021 GeoBasis-DE/BKG)

Ancillary observations were collected at Rauher Kulm (49.8287° N, 11.8497° E), a 682 m high mountain near Neustadt am Kulm, Germany, south of the Fichtelgebirge mountains. The summit is covered mainly by beech trees and is almost completely surrounded by a steep, open block field of basaltic rock (Fig. 2.4) with an area of ∼3.0 ha, only leaving the east side of the mountain to be covered by forest. Below, a larger mixed beech forest is situated, though interestingly, the first line of trees below the block field is composed of Scots pine, spruce and mountain ash with beeches only occurring a few meters away from the edge. The forest edge

above the block field, however, shows no such pine and spruce distribution; instead, occasional beech and mountain ash individuals even grow in the upper part of the block field.

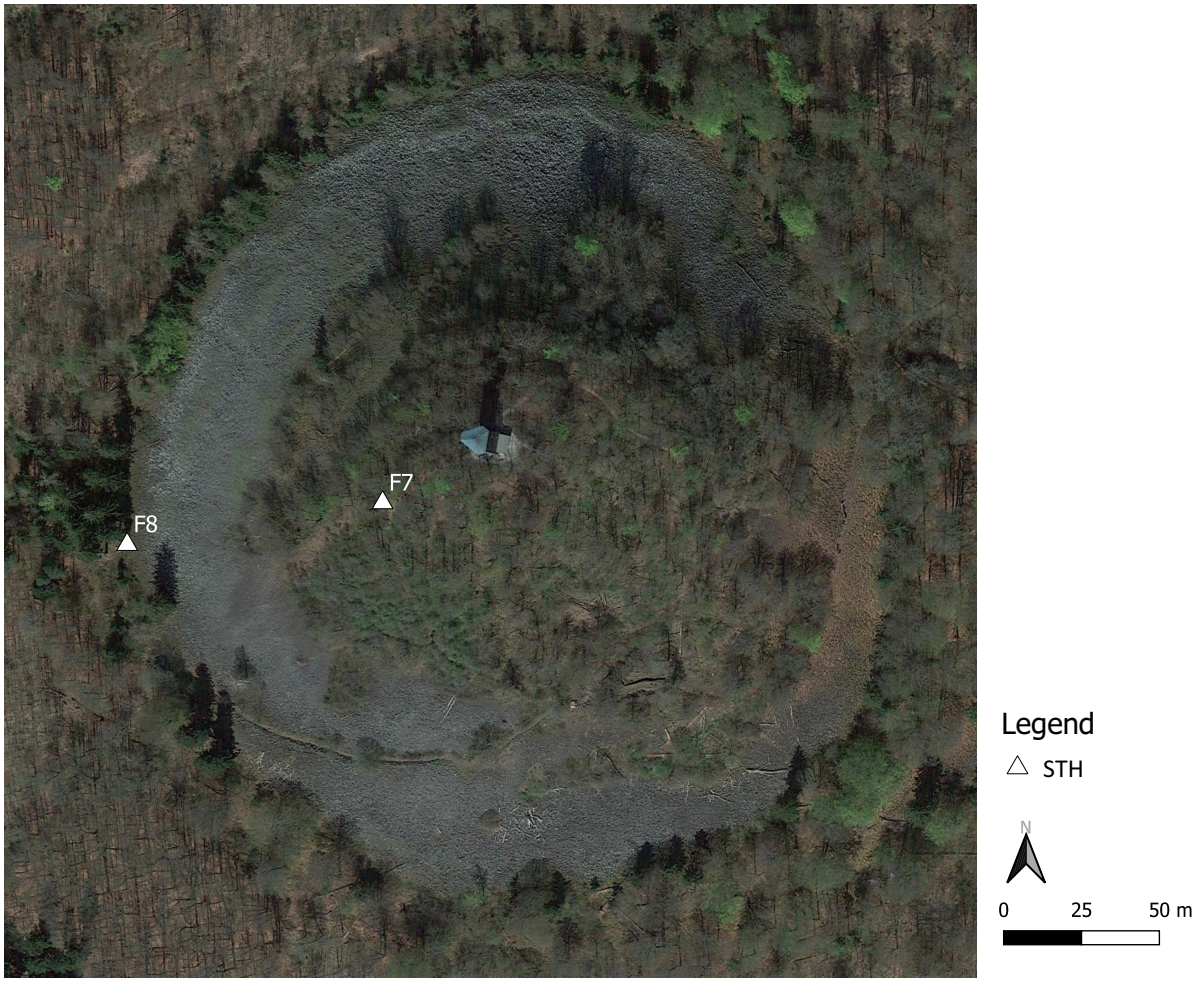

Figure 2.4.: Map of Rauher Kulm measuring site with location of installed stationary thermohygrometers (STHs). (Base map: © 2021 Google, © 2021 GeoBasis-DE/BKG)

The basaltic rock forming the mountain originated 21 million years ago (Strunz, 1975) in an underground volcano which never erupted and has been broken up into individual blocks by frost weathering, with rock diameters in the range of decimeters. The block field, summit and surroundings have been appointed as SAC in order to protect the unique flora and fauna that live on the block field, with a variety of mosses and lichen inhabiting the open rock surface (Vollrath, 1957, chap. III H 1).

A third measurement location was the mountain Buchberg (50.1149° N, 11.9363° E) ∼9 km north-east of Schneeberg. The top of this 674 m high mountain is covered by an old-growth beech forest, while the surrounding forest is mainly comprised of spruce (Fig. 2.5). The summit of Buchberg, too, is an SAC. Despite its considerable age of up to 200–220 years, the beech forest is not rejuvenating, leading to conflicts with the prohibition of deterioration for SACs in the long run. In several bachelor theses, the influence of canopy density and soil depth (Wurm, 2012), game browsing (Reiter, 2012), drought stress (Oesterle, 2015), soil substrate (Schmidt, 2018) and soil pH (Wüst, 2018) was studied, but a definite explanation for the absence of natural regeneration could not yet be found. This thesis will introduce the aspect of possible

late-frost limitation for beech rejuvenation to the list of studies conducted at Buchberg.

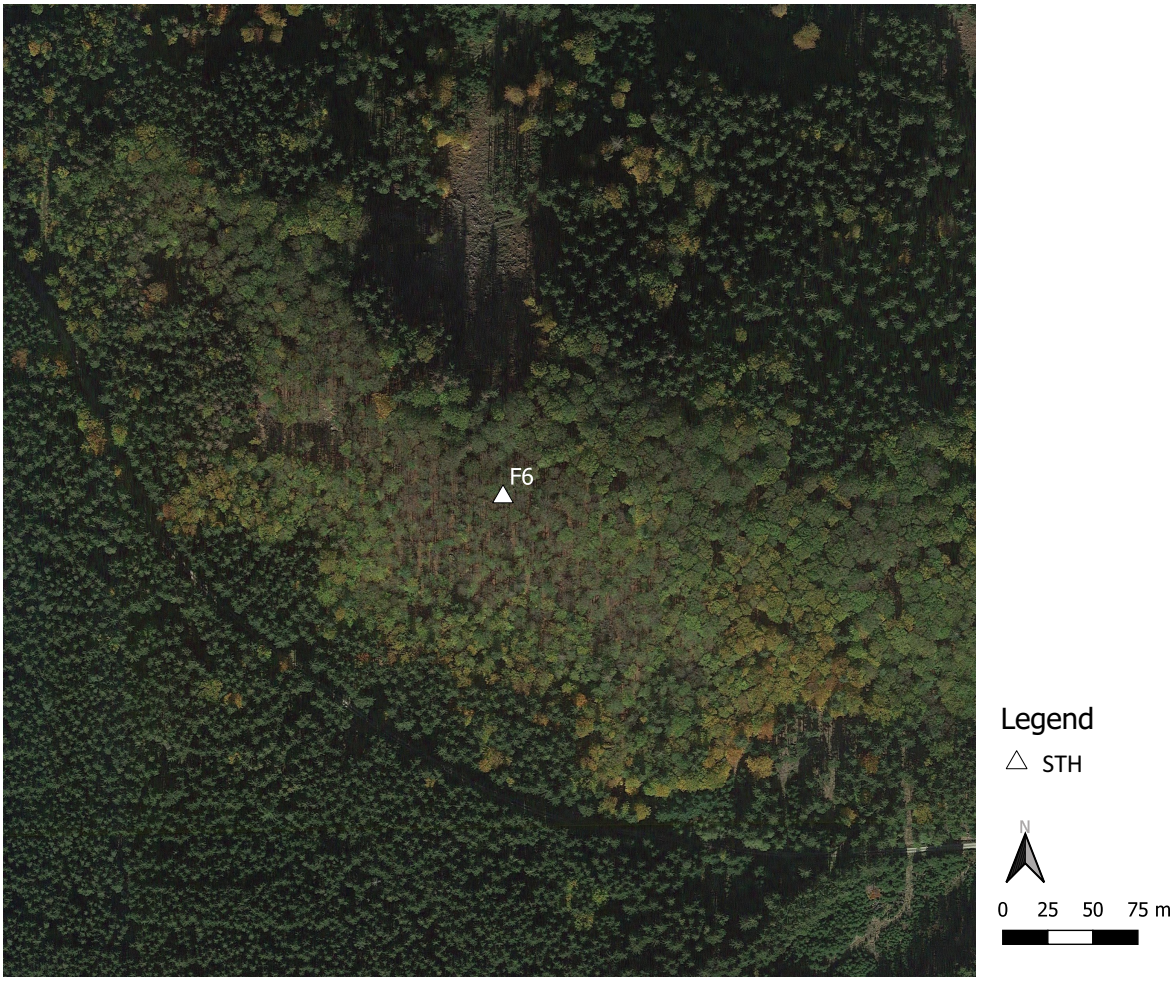

Figure 2.5.: Map of Buchberg measuring site with location of installed stationary thermohygrometer (STH). (Base map: © 2021 Google, © 2021 GeoBasis-DE/BKG)

Photographs of all measuring sites are shown in Appendix A.

2.2. Observational techniques

2.2.1. Instrumentation

Temporally continuous measurements of T_{air} at a temporal resolution of 10 min were conducted using stationary thermohygrometers (STHs; model funky_Clima, Esys GmbH, Berlin, Germany) with a thermal resolution of 0.1 K. The time constant, defined as the time needed for the measuring device to detect 63 % of a signal change, was determined experimentally as 738 s = 12.3 min using data from the cross-calibration experiment (see chapter 2.3.1) and calculating the mean time constant of five signal changes: room to fridge, fridge to freezer, freezer to room, room to stove, stove to room.
The STHs were installed in the field on 18.04.2019 (at locations F2 to F5) and 30.04.2019 (at locations F1, F6 to F8) respectively (Tab. 2.1). They were positioned inside a naturally ventilated double-walled radiation shield 25–30 cm above the ground (Fig. 2.6).

Table 2.1.: Locations of the installed stationary thermohygrometers (STHs).

STH location	site	location description	north coordinates	east coordinates	elevation (m)
F1	Schneeberg	grassland on the summit, next to one of the block heaps	50.052 03°	11.854 39°	1046.0
F2	Schneeberg	next to a beech tree above the block field	50.051 36°	11.855 10°	1038.0
F3	Schneeberg	small clearing near two beech trees above the block field	50.051 33°	11.855 48°	1034.5
F4	Schneeberg	directly below the block field	50.050 61°	11.855 56°	1020.5
F5	Schneeberg	beech plantation near the northern access road	50.062 66°	11.844 66°	870.5
F6	Buchberg	near the summit	50.114 84°	11.936 50°	673.5
F7	Rauher Kulm	west side above block field	49.828 58°	11.849 14°	665.0
F8	Rauher Kulm	west side below block field	49.828 46°	11.848 00°	619.0

Figure 2.6.: Stationary thermohygrometer at F7 above the block field at Rauher Kulm.

Additionally, hand-held measurements of T_{air} were conducted at Schneeberg site with a mobile thermohygrometer (MTH) with data recording unit (model testo 480, Testo SE & Co. KGaA, Lenzkirch, Germany). The Pt100 T_{air} sensor had a thermal resolution of 0.01 K. To minimize potential short- and longwave radiation errors, the T_{air} sensor of the MTH was kept inside a customized actively ventilated, partially double-walled radiation shield during the measurements (Fig. 2.7). This shield consisted of white-painted polyvinyl chloride tubes and a 12 V battery-powered fan (model AD0812HS-A70GL, ADDA Corp. Ltd., Taiwan). The fan was attached in such a way that it drew the air into the shield instead of blowing it, because the latter might cause additional measurement errors if the fan heated up during operation. The suction of the fan induced wind speeds of $>3\,\mathrm{m\,s^{-1}}$ inside the tubes. The design of the radiation shield was similar to a custom-aspirated radiation shield tested by Thomas and Smoot (2013), which reduced radiation errors as effectively as a commercially available triple-walled shield. Spies (2019) determined the time constant of this Pt100 T_{air} sensor to be 55 s inside a ventilated radiation shield.

Figure 2.7.: Actively ventilated radiation shield for the mobile thermohygrometer air temperature sensor.

These hand-held measurements allowed for a smaller time constant resulting in an improved spatial resolution of the roving system of the small-scale air temperature differences ΔT_{air}. Measurements were taken at fixed, predetermined locations at Schneeberg summit during the diurnal minimum T_{air} in the early morning hours (04:00 to 07:30) of four days with a late frost event: 05.05., 07.05., 14.05. and 15.05.2019. Ten of the MTH measuring points (T01-T10) were located along a 230 m long transect from the forest across the block field up onto the grassland on the summit of Schneeberg (Fig. 2.2). The lowest measuring point (T01) was chosen to be in the forest at 50 m distance from the edge of the block field, because previous studies on edge effects showed open areas to influence understory T_{air} up to 30–40 m into the forest (Davies-Colley et al., 2000; Portillo-Quintero et al., 2013). The transect measuring points were supplemented by three more measuring points below the block field (T11-T13), two above the

block field (T14-T15), four at the four beech trees that could be found above the block field (T16-T19) and one on the roof of the military building next to the weather station (T20) to allow for measurement comparisons. The measurements at T20 proved that the MTH had a high accuracy, measuring the same T_{air} values as the weather station. At each of the points T01 to T19, 10 measurements were taken at 20 cm as well as 2 m above the ground with a 1 Hz frequency.

Furthermore, images with a mobile high-resolution thermal infrared (IR) camera (model optris PI 640, Optris GmbH, Berlin, Germany) were taken in order to characterize the longwave radiation regime of the areas surrounding the MTH and STH measurement locations by measuring the surface brightness temperature $T_{surface}$. Therefore, the first camera position (C1) was located in the center of the block field, from where one image in direction of the forest below and one in direction of the forest above the block field was taken. Four of the camera positions (C2–C5) were situated near the four beech trees, while the last position (C6) was on the summit near STH location F1 (Fig. 2.2). The IR images of the beeches were used to analyze whether their $T_{surface}$ differed from T_{air}.

The IR camera measures the radiant emittance S of a surface and converts it into temperature values using the Stefan-Boltzmann law (Eq. 2.1). In this thesis, for the trees as well as the block field an emissivity ϵ of 0.92 was initially assumed.

$$S = \epsilon \cdot \sigma_{SB} \cdot T_{surface}^4 \tag{2.1}$$

$$with\ \epsilon = 0.92,\ \sigma_{SB} = 5.67 \times 10^{-8}\,\mathrm{W\,m^{-2}\,K^{-4}}\ and\ T_{surface}\ in\ \mathrm{K}$$

The positions of the measuring locations in the field were determined using a Global Positioning System (GPS) device (type GPS 72H, Garmin Ltd., Southampton, UK).

The weather observations collected by the automated weather station at the Schneeberg summit provided additional information about windiness (Fig. B.1 a) and daytime cloudiness (Fig. B.2) during the measuring period.

Wind data for Rauher Kulm was not available. As an approximate value for the windiness at this measuring site, the wind data collected by the weather station in Fichtelberg/Ofr.-Hüttstadl (49.98° N, 11.84° E) was used (Fig. B.1 b).

In order to assess whether wind speed and direction measurements recorded by the meteorological weather station on the roof of the former military building on Schneeberg summit are similar to the wind regime on the nearby block field, wind measurements were taken with a portable micro sonic anemometer (MSA; TriSonica Mini, Anemoment LLC, Longmont, CO, USA). During the night from 06.07.–07.07.2019, the MSA was positioned directly next to the weather station, before being placed in the center of the block field (Fig. 2.2) during the night from 16.07.–17.07.2019.

A comparison of the wind measurements of the portable MSA and the weather station at Schneeberg showed that both measured similar patterns in wind velocity and direction when being mounted directly next to each other (Fig. 2.8), though the squared Pearson correlation coefficient R^2 was only 0.19 for wind speed (Fig. 2.9). R^2 was determined using a linear model for the wind speed comparison and using the *circ.cor()* function of R package *CircStats* (Lund

and Agostinelli, 2018) for the wind direction, which computes a circular version of the Pearson correlation coefficient.
On average, wind velocities on the block field were lower than those on the roof of the former military building and showed disconnected patterns. Wind direction was similar on both sites during the night; however, in the early morning hours, southerly, uphill winds dominated on the block field, while on the roof, northerly winds were predominant (Fig. 2.8).
For the nighttime conditions, the data fits well to the findings of Popescu et al. (2017), who found that katabatic winds are prevalent during nighttime on a slope with rocky deposits, especially during spring and summer. After sunrise, when the surface begins to heat up, air flow will change direction and become anabatic (Foken, 2017, chap. 7.3.2). This expected flow direction change fits well with the wind direction data recorded on the block field (Fig. 2.8). Alternatively, the upwards air motion starting around 06:30 might also be caused by a turbulent wake with a cavity of reverse flow downwind of the mountain top and coincide with sunrise due to the reduced static stability at this time of day (Stull, 2017, chap. 17.7.3). The data available does not allow a definite statement which of the two mechanisms was responsible for the observed air flow.
In general, the data implies that wind speed and direction measurements taken on the roof of the military building cannot be directly transferred to the wind situation on the block field itself. Therefore, the wind data recorded by the weather station during the measurement period cannot be used to explain any observed patterns in T_{air} distribution near the block field apart from giving general information about windiness in the area.

2.2.2. Phenological observations

In order to compare tree phenology between sites and individual trees, five terminal branch buds of the uppermost three beeches at Schneeberg summit and five terminal branch buds of three trees of the beech plantation near the northern access road were selected. Since the beeches at the plantation already have a height of 5–10 m, the selected buds had to be on water sprouts in the lowest 2 m above ground. On the measuring days, the phenological stage according to the codes of the Biologische Bundesanstalt, Bundessortenamt und Chemische Indsturie (BBCH) scale (Hack et al., 1992) was determined for each bud (Tab. 2.2). Additionally, the length of all of the buds in BBCH categories 00–03 and 07 was measured.

Table 2.2.: Biologische Bundesanstalt, Bundessortenamt und Chemische Indsturie (BBCH) codes and their meaning.

BBCH code	description
00–03	winter dormancy, beginning of bud swelling, end of bud swelling
07	beginning of bud breaking
09	buds show green tips
10	first leaves spread apart
11	first leaves unfolded

Since the late frost on 05.05.2019, some of the beech trees that had already sprouted leaves had partly brownish leaf tissue. Thus, for these trees the damaged, brown area per leaf for the previously selected branch tips was estimated visually.

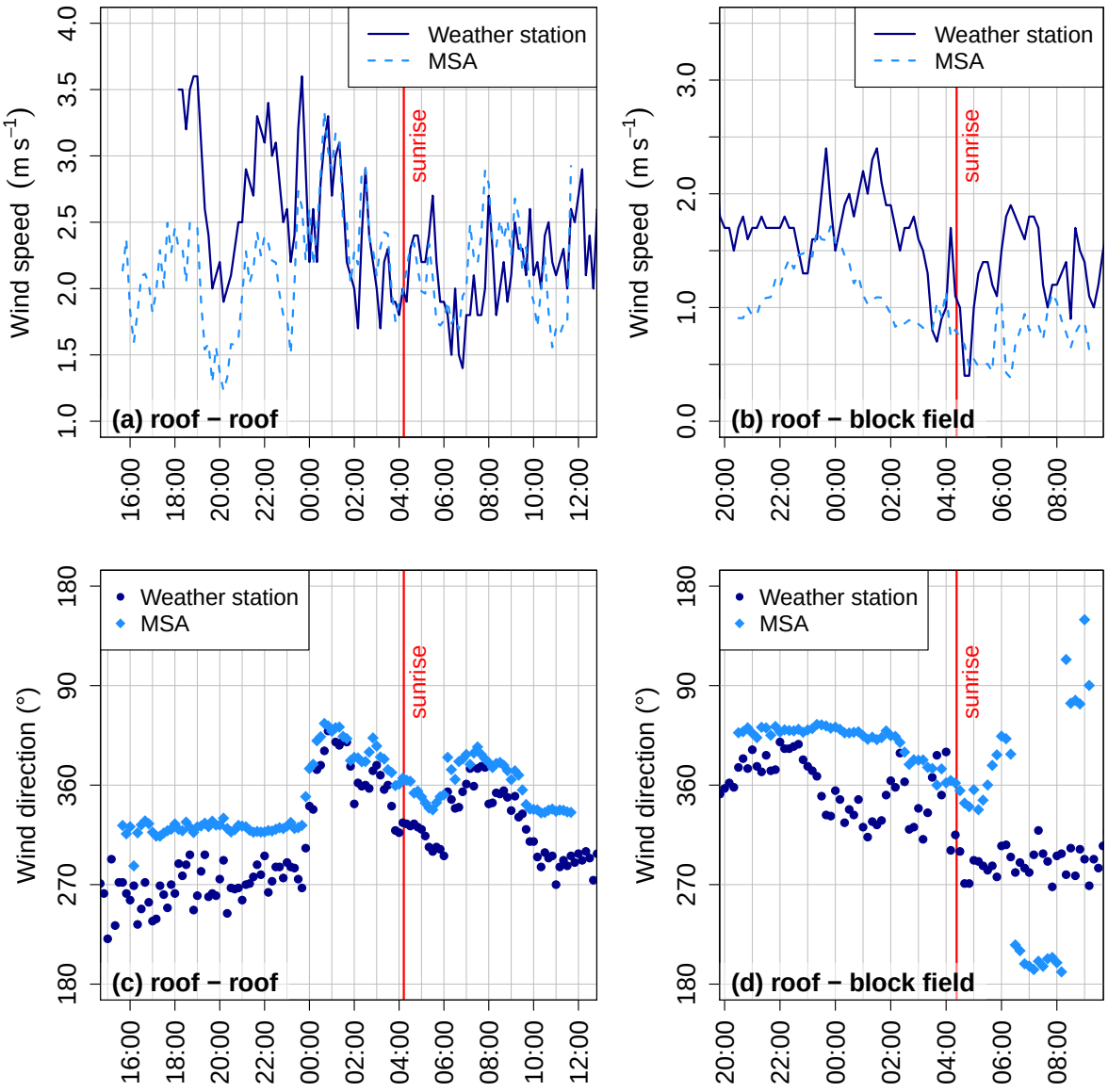

Figure 2.8.: Time series of (a) wind speed and (c) wind direction measurement comparison between the micrometeorological weather station at Schneeberg and mobile wind measurements with a micro sonic anemometer (MSA) next to the weather station (06.-07.07.2019) and time series of (b) wind speed and (d) wind direction measurement comparison with the MSA stationed in the center of the block field (16.-17.07.2019) at Schneeberg. The red line marks the time of sunrise.

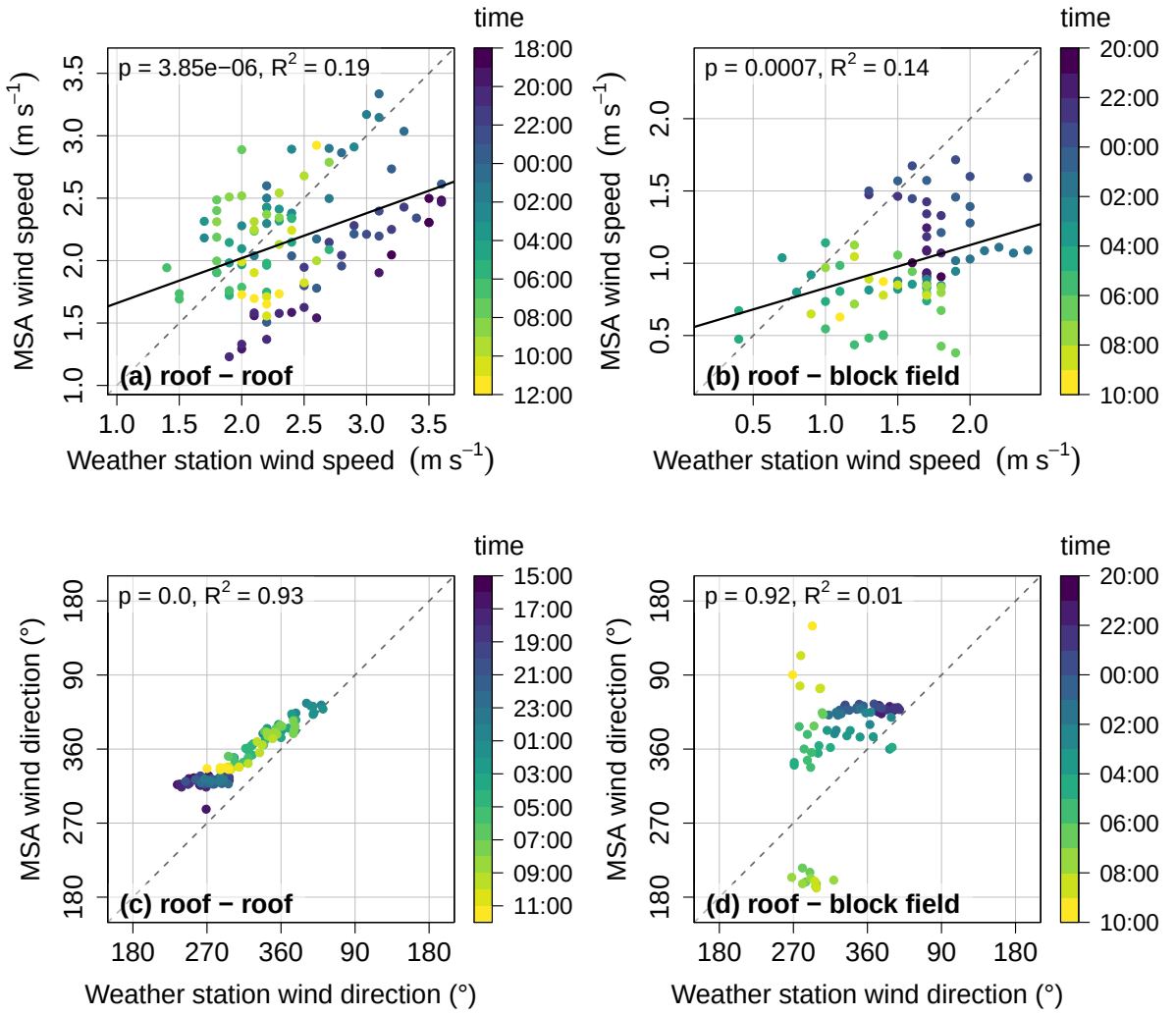

Figure 2.9.: Scatterplots and linear models of (a) wind speed and (b) wind direction measurement comparison between the micrometeorological weather station at Schneeberg and mobile wind measurements with a micro sonic anemometer (MSA) next to the weather station (06.-07.07.2019) and scatterplots of (b) wind speed and (d) wind direction measurement comparison with the MSA stationed in the center of the block field (16.-17.07.2019) at Schneeberg. The color bar represents the time of day of each measurement. R^2 denotes the square of the Pearson correlation coefficient, p is the p-value of the linear model.

2.2.3. Singular flow visualizations using artificial fog

In the evening hours of 30.10.2019 a visual air-flow analysis was performed on the block field at Rauher Kulm. For this analysis, fog generated by a fog machine (type Z-1000II, Antari Lightning & Effects Ltd., Taoyuan City, Taiwan) was illuminated by a vertical laser-plane (laser type DJ-Lase 400-B Blue, Stairville, Thomann GmbH, Burgebrach, Germany). The experiment was conducted on the west side of Rauher Kulm, the same side where the STHs had been located (Fig. 2.10). Two MTHs were used to determine T_{air} above and below the block field, recording data at a temporal resolution of 5 s. They were cross-compared in situ by being run next to each other for 1 min, then the values measured by the MTH above the block field were adjusted to the MTH below the block field.

Figure 2.10.: Block field at Rauher Kulm with setup for the flow visualization experiment: Power generator, fog machine, tube for fog locating, camera for documentation (from right to left). The laser was located to the lower left outside of the image.

2.2.4. Observational schedule for mobile thermohygrometer and infrared camera measurements

Handheld measurements took place in the early morning hours of four days: 05.05., 07.05., 14.05. and 15.05.2019. On each of those days, mobile T_{air} measurements were taken at each of the MTH measuring locations and IR camera images were taken at each camera location. The order of the measurements was the following: T01 to T13, C1, T14 to T16, C2, T17, C3, T18, C4, T19, C5 to C6. Afterwards, the BBCH category and frost damage of the beech buds and leaves were determined. On the first measuring day, the order of the measurements was

slightly different: T01 to T10, T19, T11 to T13, C1, T14 to T16, C2, T17, C3, T18, C4, C6. On average, one measuring series from T01 to C6 took 2 h 45 min. Measurements at T20 took place after bud categorizing.

2.3. Data processing

All data processing was done using RStudio Version 3.6.0.

2.3.1. Data correction

First, the STHs were cross-calibrated experimentally by being run directly next to each other. In order to cover the complete outdoor T_{air} range, they were placed inside a fridge, inside a freezer, inside an oven (once each) as well as at normal room T_{air} (four times), recording T_{air} with a resolution of 5 s. At each location, one 10-min interval was selected, except for normal room T_{air}, where four 10-min intervals were selected. Then, each STH's deviation from the mean of all STHs was calculated. Subsequently, a regression was fitted to the four deviation values of each STH and used as a correction value for the field STH data (Fig. 2.11).
However, when applied to the field data, the correction proved to worsen the STHs' accuracy. Comparing the T_{air} values measured by neighboring STHs (F1 to F4, F7 and F8, respectively) during three of the windiest nights (Fig. B.1) with mean wind speeds ranging from 3.8 to 4.8 $\mathrm{m\,s^{-1}}$ and maximum wind speeds between 5.1 and 8.7 $\mathrm{m\,s^{-1}}$ showed that the differences between measured values increased when applying the experimental cross-calibration correction (Fig. 2.12), as the longwave radiation under field conditions differs largely from experimental conditions.
An analysis of the standard deviation σ_T of a 30-min moving window of neighboring STHs during a selection of the 25 % windiest nighttime intervals (wind speed threshold: $\geq$4.0 $\mathrm{m\,s^{-1}}$ for Schneeberg and $\geq$2.4 $\mathrm{m\,s^{-1}}$ for Hüttstadl near Rauher Kulm) supported the visual analysis, revealing an increase in σ_T with the experimental cross-calibration correction from 0.29 to 0.37 K for Schneeberg and from 0.16 to 0.28 K for Rauher Kulm.
Instead, an in-situ offset correction based upon nighttime periods with wind speeds $\geq$5.1 $\mathrm{m\,s^{-1}}$ at Schneeberg and $\geq$4.5 $\mathrm{m\,s^{-1}}$ at Hüttstadl, respectively, was applied. These values correspond to the 5 % of windiest nighttime intervals (Fig. B.3 and B.1). For these intervals, the mechanically induced turbulence is expected to eliminate near-surface air temperature differences, so that neighboring STHs (F1 to F4 and F7 and F8, respectively) should measure the same potential temperature Θ values. The mean of each STH as well as the mean of all STHs of one location were calculated for these periods. Then, the difference in the mean of the individual STHs to the mean per location was used as a cross-calibration value for an offset correction. As a result, F5 and F6 could not be calibrated since no other STHs were located nearby.
All STHs measured T_{air} once every 10 min, but not at the same time, because they had an arbitrary start time. Therefore, the data was interpolated to allow for T_{air} values at given time steps (XX:00, XX:10, XX:20, XX:30, XX:40 and XX:50).
In order to compare the T_{air} measurements at the different measuring sites, Θ was used to take different elevations a.s.l. into account (Eq. 2.2).

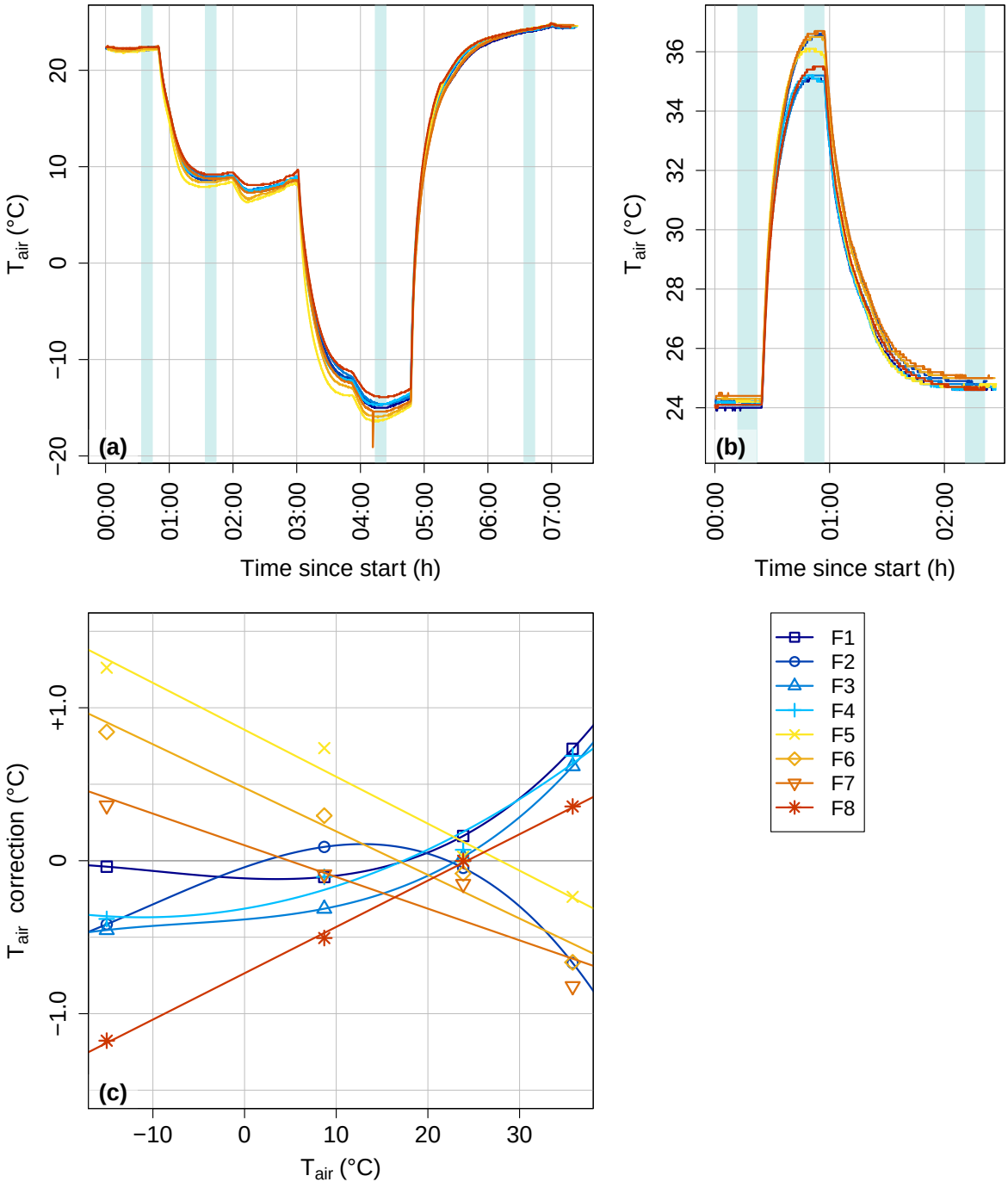

Figure 2.11.: Air temperature T_{air} measured by stationary thermohygrometers (STHs) during cross-calibration experiment in (a) fridge and freezer and (b) stove, with (c) derived correction values per T_{air}. Blue bars indicate the 10-min time intervals used for calibration.

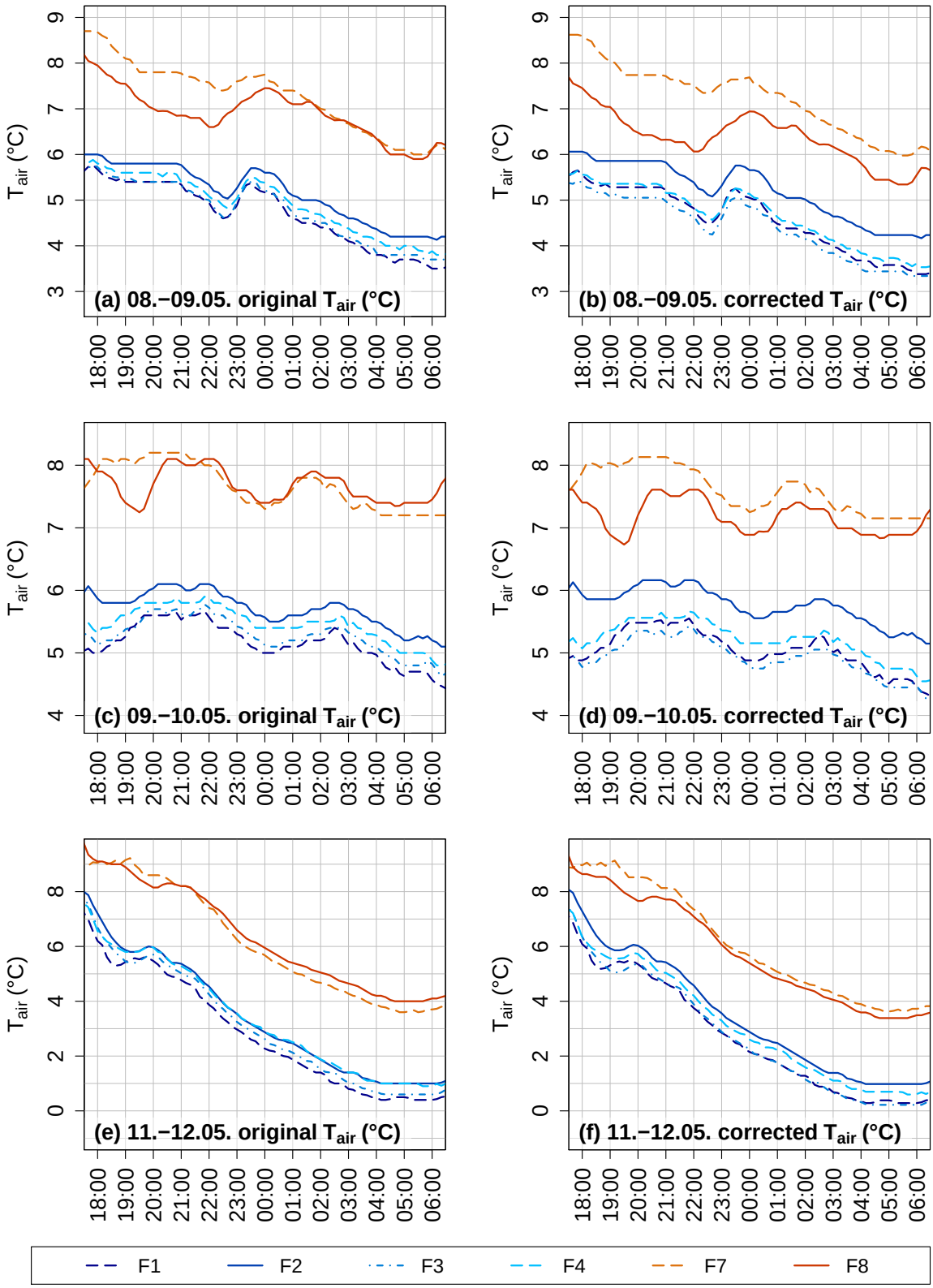

Figure 2.12.: Air temperature T_{air} values measured by neighboring stationary thermohygrometers (STHs) (F1 to F4, F7 and F8, respectively), (a), (c), (e) original versus (b), (d), (f) corrected with experimental cross-calibration values during three of the most windy nights.

$$\Theta = T_{air} \left(\frac{p_0}{p} \right)^{\kappa_L} \tag{2.2}$$

$$with\ p_0 = 1000\,\mathrm{hPa}\ and\ \kappa_L = \tfrac{2}{7}$$

However, since no pressure measurements were available, a simplified equation assuming a constant T_{air} gradient had to be used (Eq. 2.3). Therefore, an analysis of all available STH data as well as weather station data from Schneeberg and Bayreuth was performed (Fig. 2.13). From the data, a mean T_{air} gradient γ of $-6.3\,\mathrm{K\,km^{-1}}$ was chosen. All Θ values refer to a reference elevation z_0 of 871 m a.s.l., the mean elevation of all STHs, which is also the elevation of the beech plantation at Schneeberg.

$$\Theta = T_{air} + (z_0 - z) \cdot \gamma \tag{2.3}$$

$$with\ z_0 = 871\,\mathrm{m}\ and\ \gamma = -0.0063\,\mathrm{K\,m^{-1}}$$

For the analyses, the MTH data was divided into a spatial or temporal mean and deviations from the mean (Eq. 2.4).

$$\begin{aligned} & value & = & \ mean & + & \ perturbation \\ temporal\ scale: \quad & X & = & \ \overline{X} & + & \ X' \\ spatial\ scale: \quad & X & = & \ \langle X \rangle & + & \ \widehat{X} \end{aligned} \tag{2.4}$$

On average, the MTH measurements took 2 h 45 min to complete, which aggravates direct intercomparison because of the inherent T_{air} instationarity during the morning transition period (defined as 03:20–05:50, see chapter 2.3.2). Any ΔT_{air} between the MTH measuring points might therefore be due to the temporal rather than the spatial offset. To account for this, the MTH data was normalized onto a single point in time. For each of the four nights when MTH measurements were conducted, the time of lowest T_{air} was determined using the STH data mean T_{air} value recorded by F1 to F4 (Fig. 2.14). Then, the difference between the mean of the values recorded by F1 to F4 at the time of lowest T_{air} and every MTH measurement was calculated and subtracted from the MTH data (Eq. 2.5).

$$T_{MTH\_corrected} = T_{MTH} - (\langle T_{F1,F2,F3,F4} \rangle - \langle T_{F1,F2,F3,F4} \rangle_{min}) \tag{2.5}$$

$$with\ \langle T_{F1,F2,F3,F4} \rangle = spatial\ mean\ of\ T_{air}\ measured\ by\ STHs\ at\ F1,\ F2,\ F3\ and\ F4$$
$$and\ \langle T_{F1,F2,F3,F4} \rangle_{min} = minimum\ value\ of\ \langle T_{F1,F2,F3,F4} \rangle\ per\ night$$

In addition to its internal black field calibration option, the optris camera was calibrated with a ∼2 cm thick aluminum plate that was coated with thermographic black paint (LabIR, Plzeň, Czechia) with an ϵ of 0.95 in the IR spectrum. This calibration was performed at each measuring location on each measuring day. Images of the aluminum plate were taken at a distance of 20–30 cm from the IR camera. Since the camera was set to use an ϵ of 0.92, the $T_{surface}$ values of the aluminum plate were subsequently re-calculated using the Stefan-Boltzmann equation (Eq. 2.1) and an ϵ of 0.95. A measurement with the MTH Thermocouple type K temperature

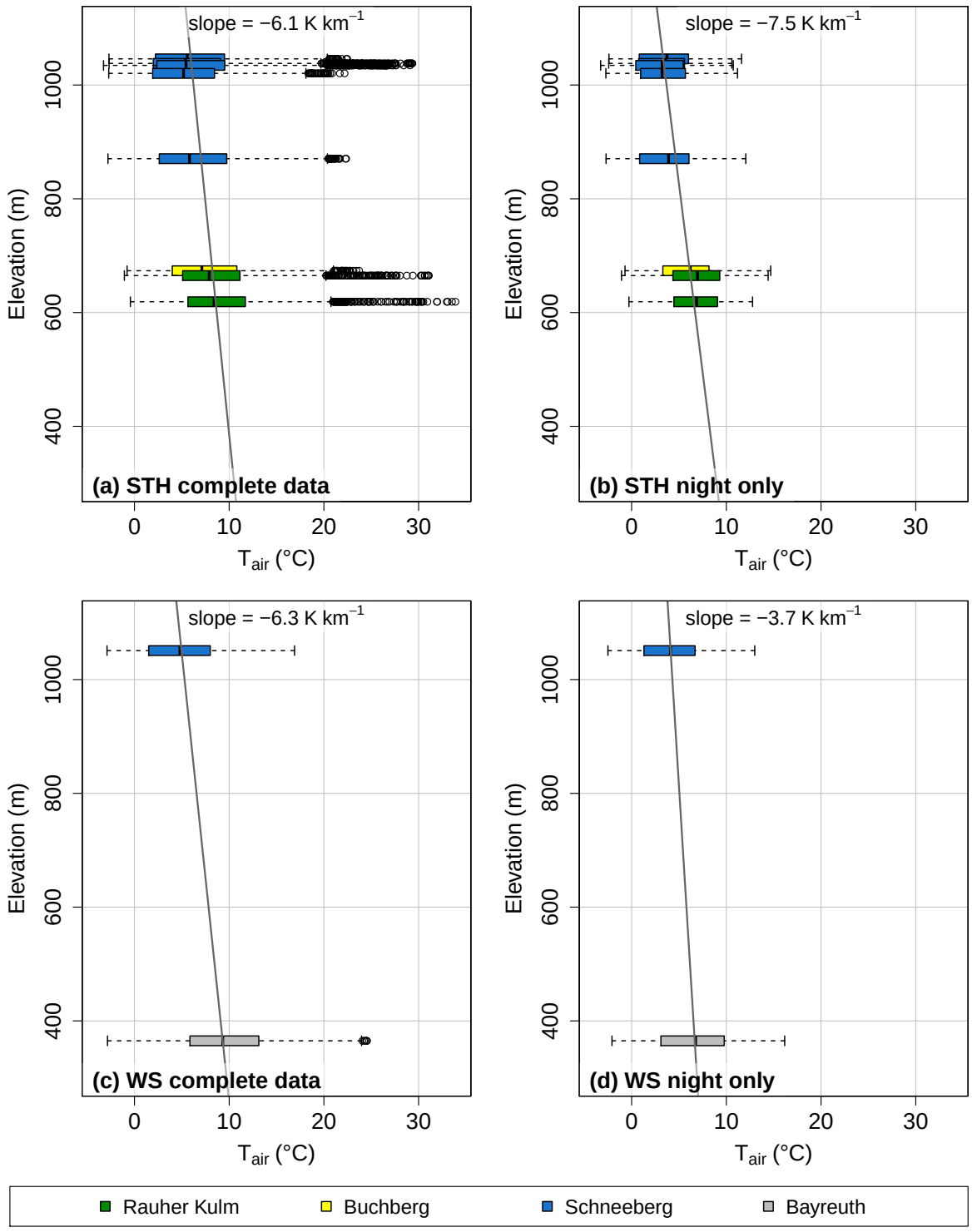

Figure 2.13.: Air temperature T_{air} in relation to measurement elevation above sea level, measured by (a) stationary thermohygrometers (STHs) over the study period, (b) STHs at nighttime during the study period, (c) weather stations (WS) over the study period and (d) weather stations at nighttime during the study period.

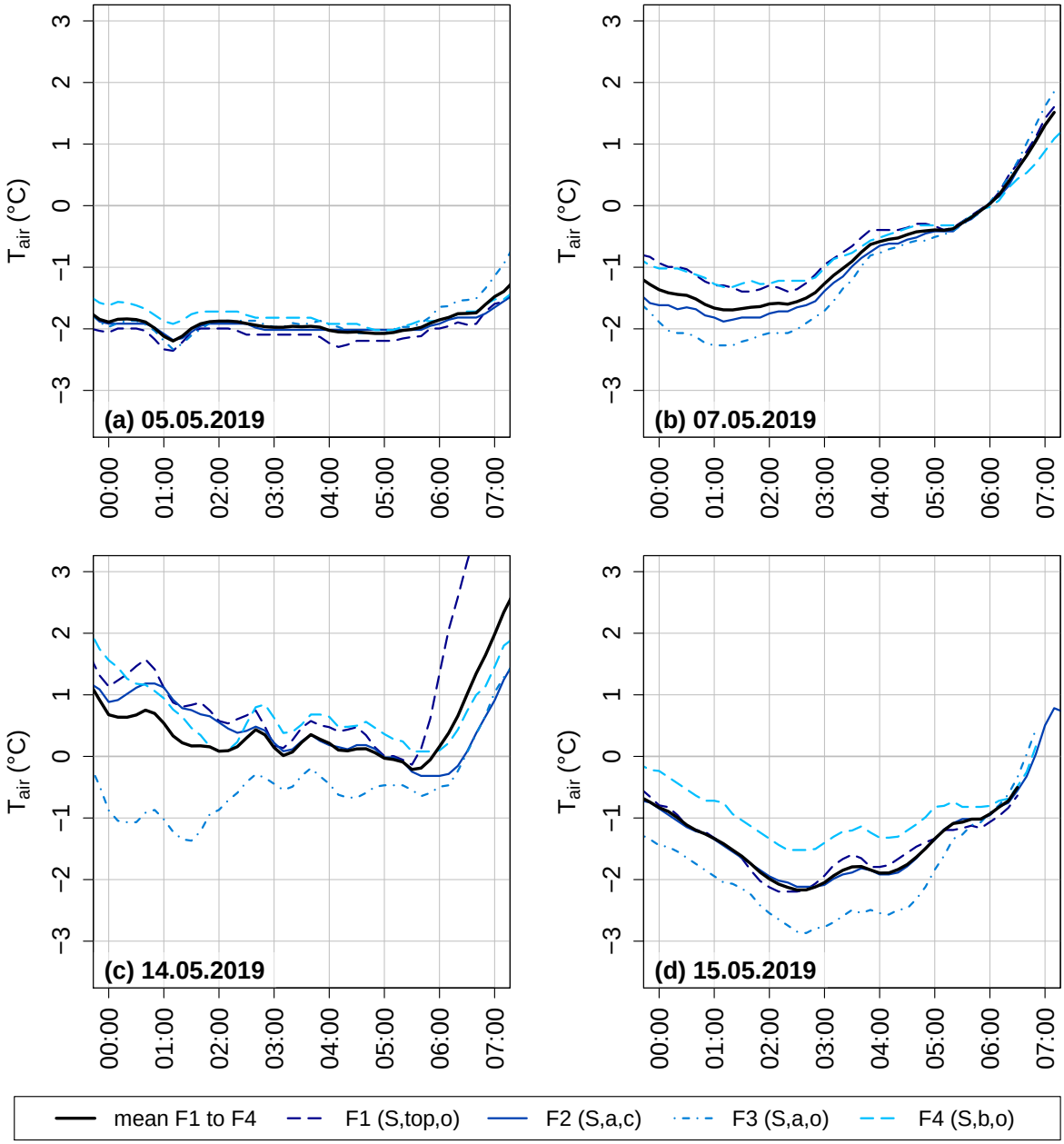

Figure 2.14.: Air temperature T_{air} measured by stationary thermohygrometers (STHs) at F1 to F4 and mean of measurements at F1 to F4 during the four nights during which hand-held measurements took place: early morning hours of (a) 05.05.2019, (b) 07.05.2019, (c) 14.05.2019 and (d) 15.05.2019. Parentheses in plot legend describe the location of each STH: S = Schneeberg, top = summit, a = above block field, b = below block field, o = open to the sky, c = under canopy.

sensor inserted into the plate simultaneously to an image of the plate with the IR camera enabled a direct comparison of the measurement techniques.

The IR images consist of 640×480 pixels each. Of each IR image of the aluminum plate, the mean $T_{surface}$ of the center 100×100 pixels was calculated (Eq. 2.6). From this value, the temperature measured with the Thermocouple sensor inside the plate was subtracted. The resulting ΔT value was used to calibrate the subsequent IR images of the trees and the block field. Overall, the Thermocouple sensor measured higher temperatures than the IR camera (Fig. 2.15).

$$T_{surface\_center} = \frac{1}{100 \cdot 100} \sum_{x=271}^{370} \sum_{y=191}^{290} T_{pixel_{x,y}} \tag{2.6}$$

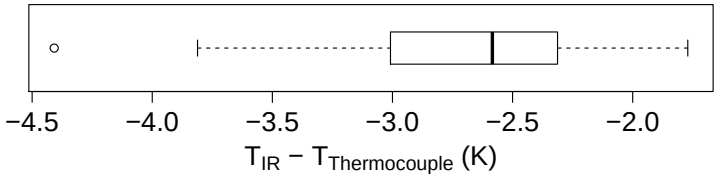

Figure 2.15.: Temperature difference ΔT between infrared (IR) camera and mobile thermohygrometer Thermocouple sensor measurements of aluminum plate. The bold line marks the median, the box encompasses the 25^{th} to 75^{th} percentile, whiskers encompass the range of all data except for outliers, dots are outliers.

In most of the images of the four beech trees at the summit of Schneeberg that were taken with the IR camera, the trees are barely visible (Fig. B.4–B.7), which means they had the same $T_{surface}$ as their surroundings. This finding applies especially for B1 and B2 (Fig. 2.16 a–b). Since these two trees were very small, having not yet reached 2 m of height, their stems were only marginally thicker than the branches and leaves of the surrounding blueberry bushes covering the ground. Thus, they had similar cooling rates and reached similar $T_{surface}$ during the night. The stem and branches of B3 and B4, on the other hand, were sometimes marginally warmer or colder than the surrounding surfaces (Fig. 2.16 c–d), however without any clear pattern. In general, it can therefore be assumed that the beeches' stem and branch $T_{surface}$ is equal to the mean image $T_{surface}$ after omitting image pixels containing sky temperatures, as those contained much lower temperature values.

A comparison of $T_{surface}$, calculated as the mean per IR image, and T_{air} at 2 m height above ground near each of the beech trees showed that $T_{surface}$ was always higher than T_{air} (Fig. 2.17). Musselman and Pomeroy (2017) state tree trunk $T_{surface}$ to be equal to T_{air} after sunset, and especially since the beeches investigated in this thesis all have relatively thin trunks, it can be assumed that $T_{surface}$ of the beeches and T_{air} coincided. The difference between $T_{surface}$ and T_{air} was probably caused by a misestimation of ϵ, as the $T_{surface}$ calculation depends strongly on the assumed ϵ (Eq. 2.1). For $T_{surface}$ and T_{air} to have no offset, ϵ would have to be 0.95. Therefore, all $T_{surface}$ values recorded by the IR camera of the block field and the canopy under assuming an ϵ of 0.92 were re-calculated with an ϵ of 0.95 for further analyses.

Additionally to an analysis of block field $T_{surface}$ (Appendix C), a rectangular subset of at

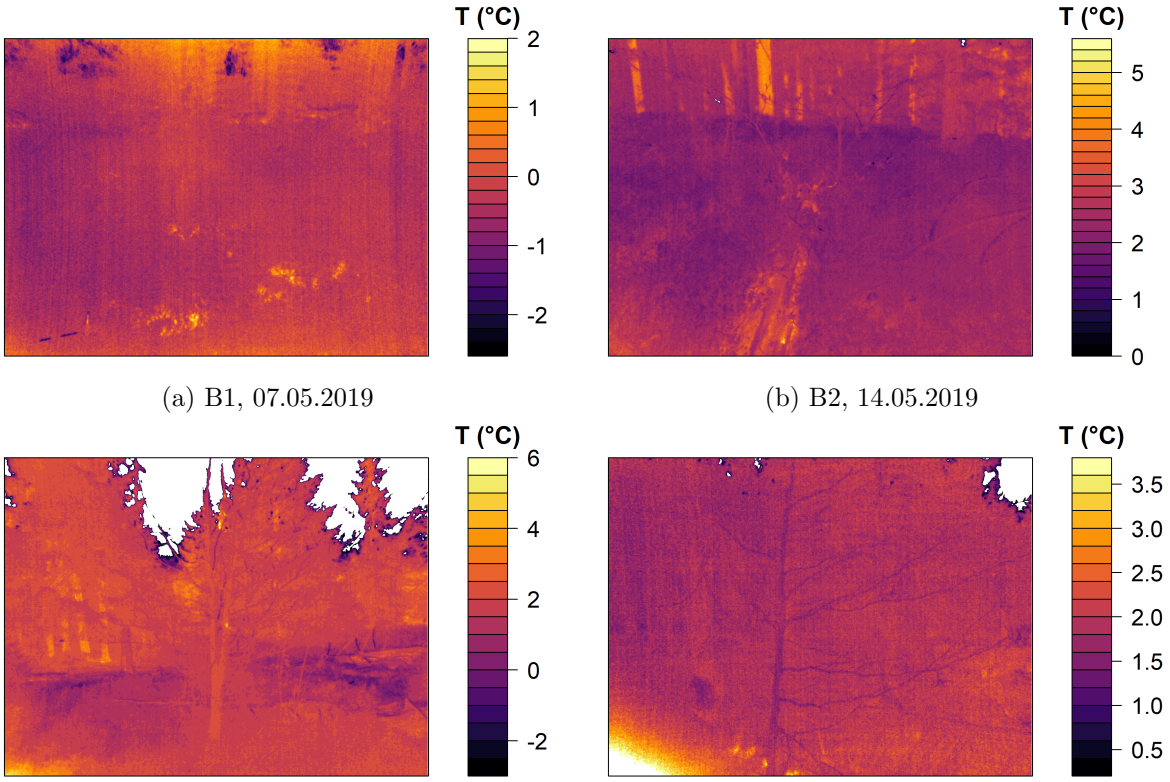

(a) B1, 07.05.2019

(b) B2, 14.05.2019

(c) B3, 14.05.2019

(d) B4, 07.05.2019

Figure 2.16.: Surface brightness temperature $T_{surface}$ of beech trees at Schneeberg summit and their surroundings on selected days, assuming an emissivity of 0.92. White areas indicate temperatures outside of the range of the color bar.

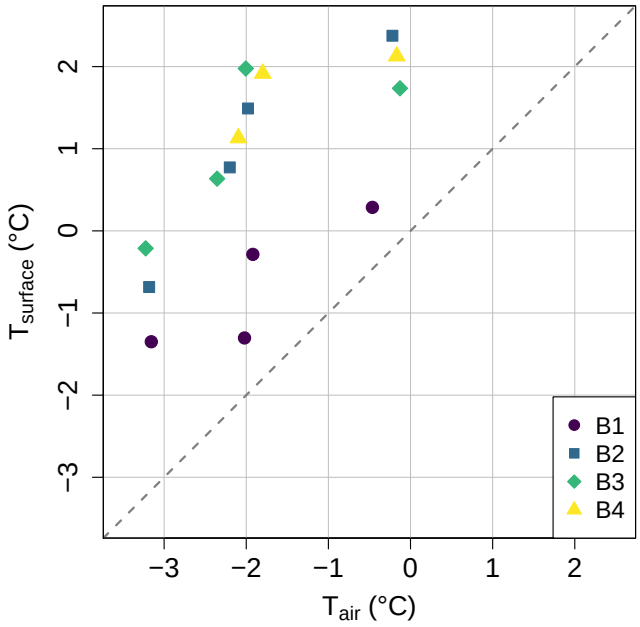

Figure 2.17.: Surface brightness temperature $T_{surface}$ measured by infrared camera in comparison to air temperature T_{air} at 2 m height above ground measured by the mobile thermohygrometer near each of the beeches. Symbols refer to different beech trees with one comparison value per measuring day. For B4, there are only three comparison values since no infrared image was taken on the first measuring day.

least 331 × 71 and up to 361 × 101 pixels containing canopy $T_{surface}$ was selected visually in the images taken at camera location C1 for each day to compare above and below block field canopy $T_{surface}$ (Fig. 2.18).

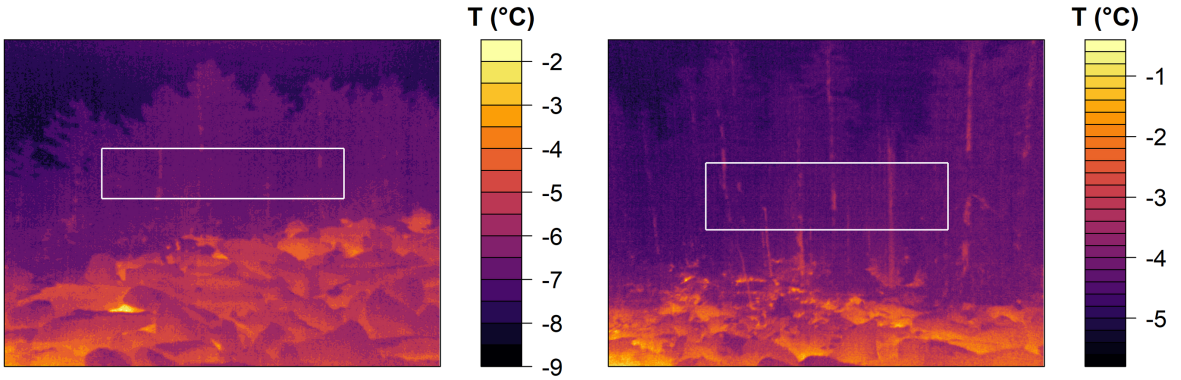

(a) C1 uphill (b) C1 downhill

Figure 2.18.: Infrared image taken at location C1 in (a) uphill and (b) downhill direction on 05.05.2019, using an emissivity of 0.95. Color scale represents surface brightness temperature $T_{surface}$ in °C, white rectangle marks the pixels used for calculating canopy $T_{surface}$.

2.3.2. Data selection

The STHs were deployed in the field from April to July 2019. However, due to battery shortages and defective contacts, several of them stopped taking measurements much earlier. For comparability reasons, the STH data used in this thesis only consists of the time period when all eight STHs worked: from 30.04.2019 to 23.05.2019. This interval is also the time period during which late frosts occurred (Fig. 2.19).
Six nights were selected as frost nights. Frost nights were defined as the nights for which at least four out of the five STHs at Schneeberg recorded at least one 10-min T_{air} value below 0 °C after the temperature correction was applied. These were also the coldest nights at Buchberg and Rauher Kulm. The respective nights and the minimum T_{air} measured by each STH are shown in Tab. 2.3.

Table 2.3.: Minimum air temperature measured by the stationary thermohygrometers at Schneeberg during frost nights in degree Celsius.

night	F1	F2	F3	F4	F5
04.-05.05.2019	-2.7	-2.7	-2.7	-2.3	-2.7
05.-06.05.2019	-2.6	-2.4	-3.3	-2.7	-2.8
06.-07.05.2019	-1.4	-1.9	-2.3	-1.3	-1.9
12.-13.05.2019	-1.1	-0.9	-1.3	-0.6	-0.4
13.-14.05.2019	-0.1	-0.3	-1.4	0.1	-0.7
14.-15.05.2019	-2.2	-2.1	-2.9	-1.5	-1.9

The time of sunrise and sunset was determined for F1 with the R function *getSunlightTimes()* of R package *suncalc* (Thieurmel and Elmarhraoui, 2019). Sunrise was between 04:53 on 30.04. and 04:18 on 23.05., while sunset was between 19:30 and 20:03, though location-specific times of sunrise and sunset are expected to differ slightly due to topography. A transition period

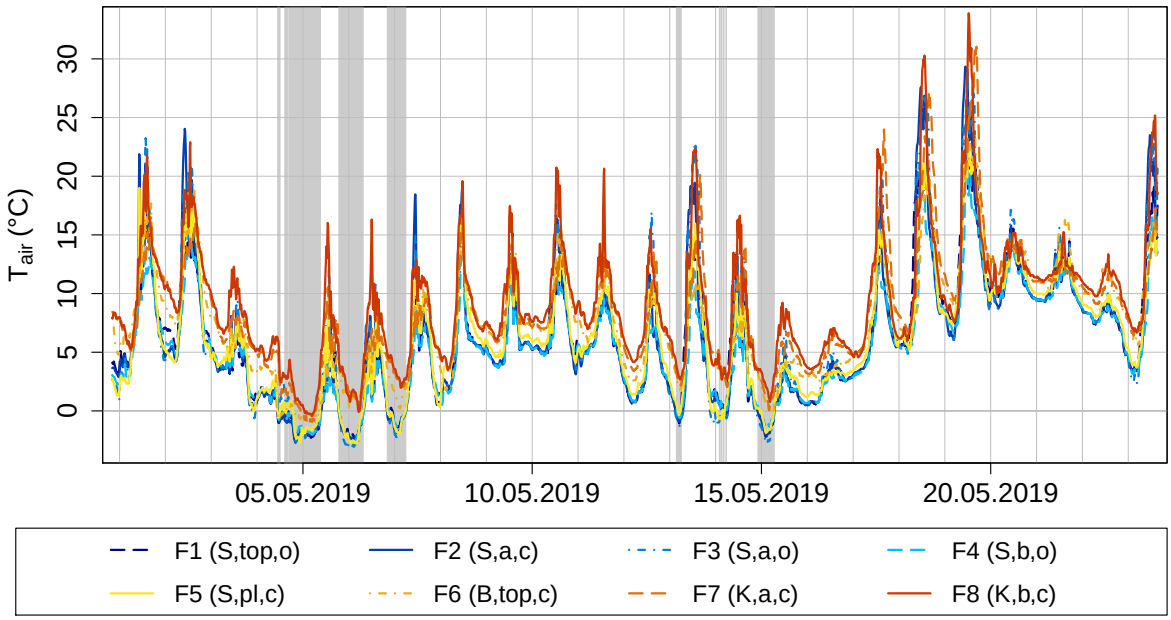

Figure 2.19.: Air temperature T_{air} measured by stationary thermohygrometers (STHs) during the experiment. Grey bars indicate the times with T_{air} at Schneeberg (spatial mean of F1 to F5) below 0 °C. Parentheses in plot legend describe the location of each STH: S = Schneeberg, B = Buchberg, K = Rauher Kulm, top = summit, a = above block field, b = below block field, pl = plantation, o = open to the sky, c = under canopy.

was defined as the sunrise and sunset period ±1 h, therefore the morning transition was from 03:20–05:50 and evening transition from 18:30–21:00. All time designations refer to Central European Time without daylight saving time.

2.3.3. Multiresolution decomposition

In order to analyze correlations between measuring locations and the amount of energy contained at different time scales, a multiresolution decomposition (MRD) (Howell and Mahrt, 1997) was conducted on the STH and the weather station data using Matlab Version R2019b and a software code written by Thomas (2011). The software decomposed the data orthogonally into subrecords of dyadic width (2^n). The original 10-min data set contained 144 data points per 24 h, which was supposed to be the longest averaging interval. However, 144 cannot be expressed as 2^n with n being an integer, therefore the data set had to be resampled to a temporal resolution of 11.25 min so that the 24 h interval contained $2^7 = 128$ data points.
The MRD was performed for different subsets of the complete STH data set: all data, only daytime, only nighttime, only morning transition, only evening transition and only frost nights. Since the subsets consisted of a varying amount of data points, different amounts of averaging windows were used (Tab. 2.4). Unlike for the other analyses, morning and evening transition were defined as sunrise/sunset −1 h and +1.5 h, adding an extra half hour to the transition period to reduce daytime to an exact 12 h interval, since this fitted the averaging windows. For the complete data set, the beginning of a day was selected as the beginning of daytime (06:22) to not cut the night in half.
The MRD computed unweighted averages for each of the subrecords with 2^{M-m} different

averaging windows of 2^m data points each, with $m = 0, ..., M$. Here, $m = 0$ corresponds to the original record resolution and $m = M$ to the record mean. M is the highest MRD mode, with $M + 1$ being the number of MRD modes.
With these results, spatial two-point correlation coefficients R_T between any two stations i and j (out of the weather station at Schneeberg and all the STHs) were computed for each of the time scales (Eq. 2.7).

$$R_{T,ij} = \frac{\overline{T_i' T_j'}}{\sigma_{T_i} \sigma_{T_j}} \tag{2.7}$$

Furthermore, the mean spectrum density D_T was calculated for each of the stations and each of the time scales to determine the amount of energy contained at each scale (Eq. 2.8).

$$D_T = \frac{1}{2^{M-m}} \sum_{1}^{2^{M-m}} T_m^2 \tag{2.8}$$

The raw power spectra were then normalized by dividing by the variance σ_T^2 and multiplying by the frequency f.

Table 2.4.: Multiresolution decomposition settings used per subset for calculating spatial two-point correlation coefficients and power spectra.

subset	no. of days	time of day	length of subset	no. of modes	averaging windows
all data	22	06:22:00–06:10:45	23 h 48 min 45 s	8	11.25 min, 22.5 min, 45 min, 1.5 h, 3 h, 6 h, 12 h, 1 d
daytime	22	06:22:00–18:22:00	12 h	7	11.25 min, 22.5 min, 45 min, 1.5 h, 3 h, 6 h, 12 h
nighttime	22	21:33:15–03:10:45	5 h 37 min 30 s	6	11.25 min, 22.5 min, 45 min, 1.5 h, 3 h, 6 h
morning transition	22	03:22:00–06:10:45	2 h 48 min 45 s	5	11.25 min, 22.5 min, 45 min, 1.5 h, 3 h
evening transition	22	18:33:15–21:22:00	2 h 48 min 45 s	5	11.25 min, 22.5 min, 45 min, 1.5 h, 3 h
frost nights	6	21:33:15–03:10:45	5 h 37 min 30 s	6	11.25 min, 22.5 min, 45 min, 1.5 h, 3 h, 6 h

3. Results and discussion

3.1. Flow visualization experiment using artificial fog

Wind speeds during the flow visualization experiment using artificial fog were generally low. In the beginning of the evening until 17:30, velocities were still relatively high with a maximum of $1.4\,\mathrm{m\,s^{-1}}$, whereas during the later phase of the evening after 17:30, wind speeds ranged mostly from $0.1\,\mathrm{m\,s^{-1}}$ to $0.4\,\mathrm{m\,s^{-1}}$ (Fig. 3.1).

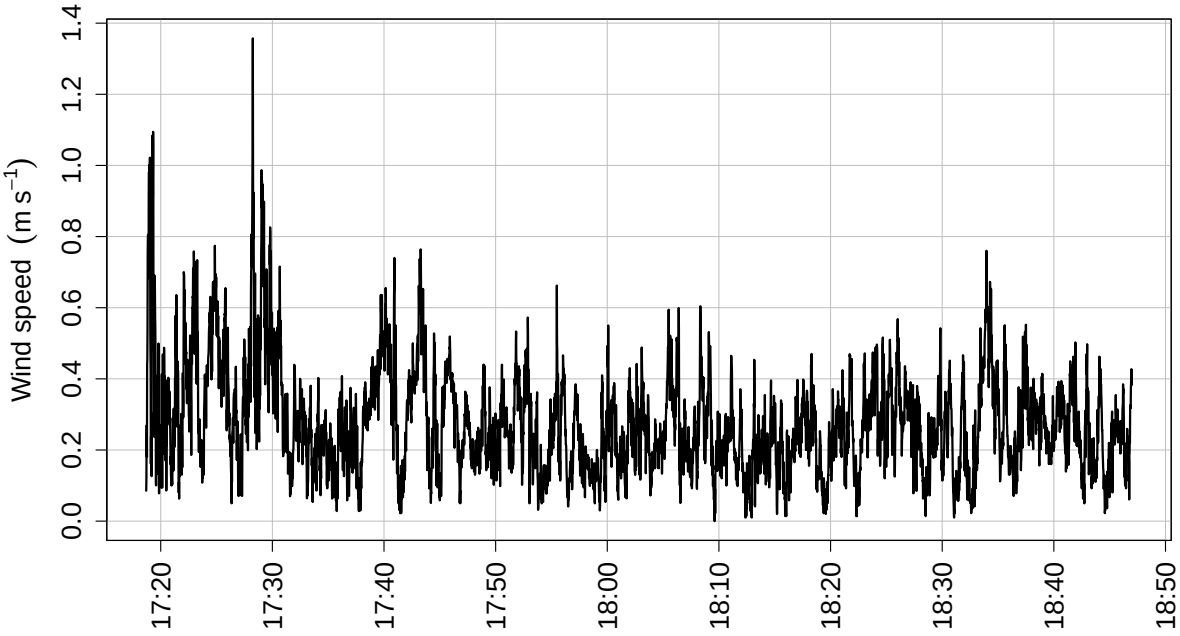

Figure 3.1.: Horizontal wind speed at the center of the block field at Rauher Kulm on 30.10.2019.

Two MTHs placed at the block field, one at the top, the other at the bottom, showed that T_{air} was consistently higher at the upper part of the block field than the lower part (Fig. 3.2 a), with a ΔT_{air} of 0.5–2.5 K early in the evening until approximately 17:50, then increasing to a difference of 1.0–3.0 K. A linear model quantified this ΔT_{air} increase to be $0.5\,\mathrm{K\,h^{-1}}$ during the time of the experiment (Fig. 3.2 b).

The visual flow analysis of the released fog revealed a continuous uphill air draft around the time of sunset, which took place at 16:55. The first downhill air flow appeared at 17:38, 43 min after sunset. However, no continuous downhill flow developed thereafter; instead, the mostly uphill flow only ever changed direction to a downward movement for short periods of time of around 1 min duration (Fig. 3.3).

An inversion between the bottom and the top of the block field is to be expected as a result of cold-air drainage across the block field (Popescu et al., 2017; Růžička et al., 2012). However,

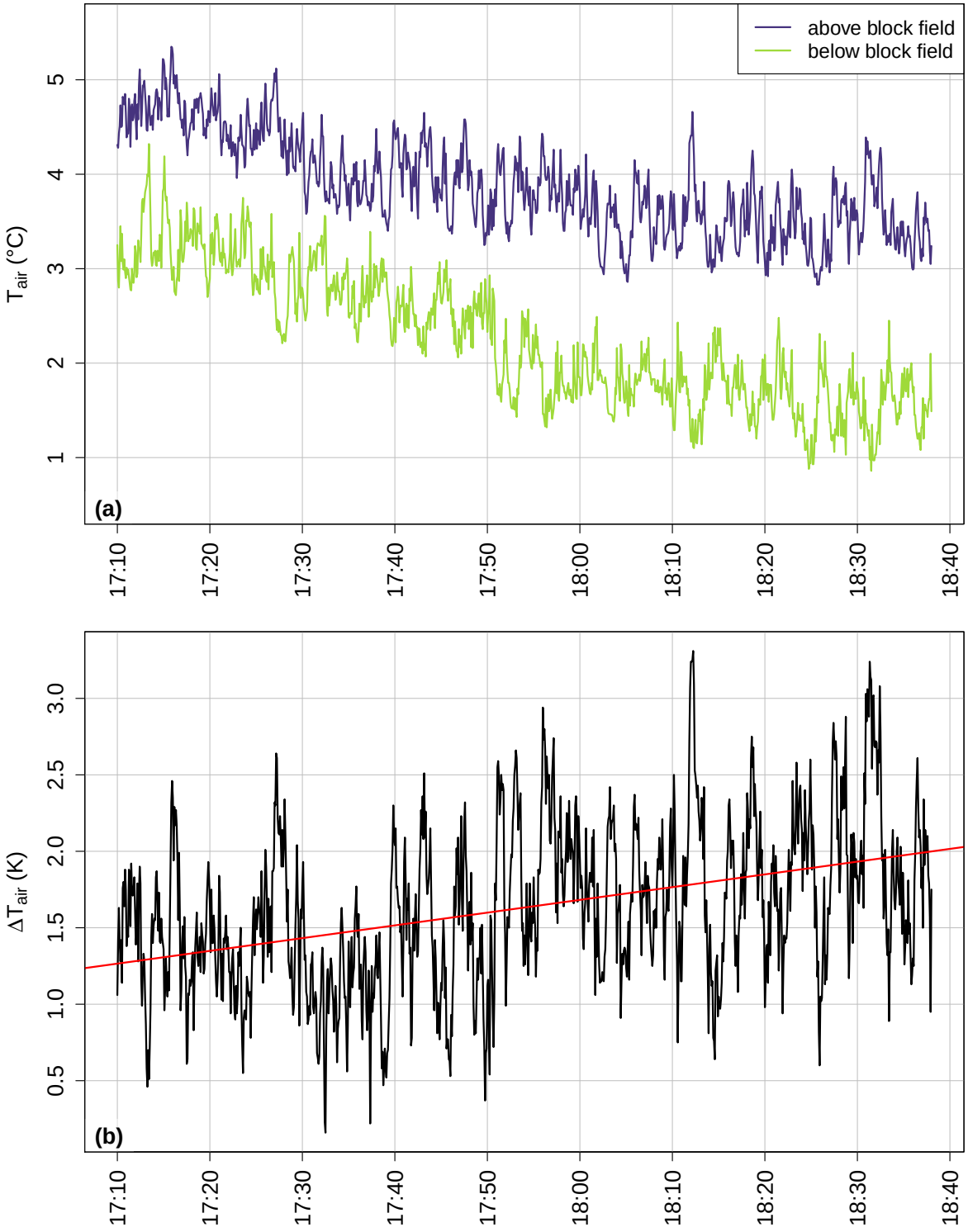

Figure 3.2.: (a) Air temperature T_{air} above and below the block field at Rauher Kulm on 30.10.2019 and (b) air temperature difference ΔT_{air} between upper and lower part of the block field. The slope of the linear model (red line) is $0.5\,\mathrm{K\,h^{-1}}$, the p-value $<2.2 \times 10^{-16}$.

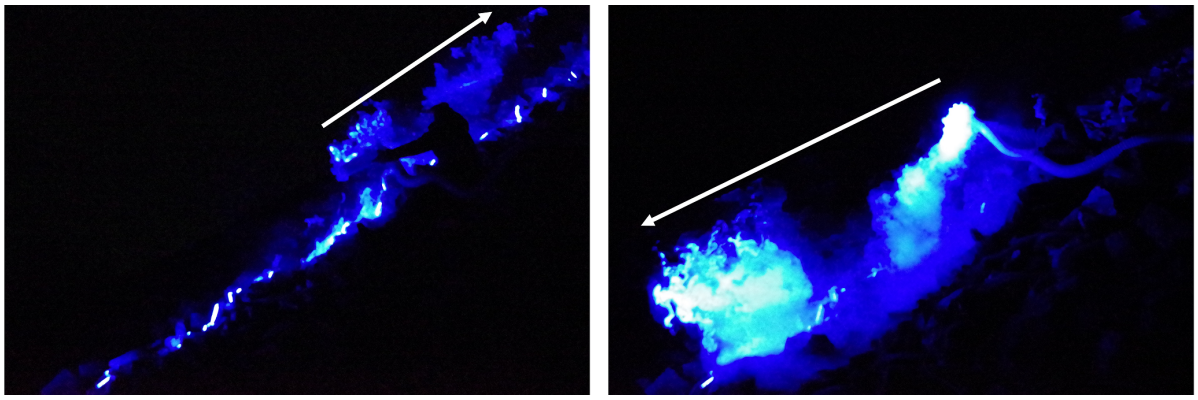

(a) Uphill flow, 19:06:52 h (Photo: C. Thomas) (b) Downhill flow, 19:07:24 h (Photo: C. Thomas)

Figure 3.3.: Laser-illuminated fog visualizing the air flow across the slope at Rauher Kulm on 30.10.2019. Pictures (a) and (b) were taken within half a minute of each other. White arrows indicate the direction of fog flow.

despite an inversion being present at Rauher Kulm site, the observed scarcity of downhill air flows suggests that other factors generated the inversion. As the experiment was performed on the west side of Rauher Kulm, the upper part of the block field received sunlight directly until sunset, whereas the lower part had been shaded by trees. This difference in direct-beam exposition might have caused a much higher energy absorption in the upper blocks, leading to higher T_{air}. On the day of the experiment, the large-scale synoptical situation was dominated by westerly winds. Despite the low mean wind speeds of 1.0–1.9 $\mathrm{m\,s^{-1}}$ according to the nearest weather station in Hüttstadl and only 0.3 $\mathrm{m\,s^{-1}}$ on average according to the MSA on the block field, this was probably sufficient to push the air uphill, leading to only short cold-air drainage periods when the westerly winds abated.

3.2. Continuous air temperature measurements

3.2.1. Ensemble average nighttime temperatures

Nighttime temperatures from STHs were similar for locations F1 to F5 at the Schneeberg summit (Fig. 3.4). The mean nighttime T_{air} at Schneeberg during the measuring period was 3.6 °C. In comparison, at Buchberg, the nighttime T_{air} was on average 5.9 °C and at Rauher Kulm 6.7 °C (Fig. B.8).

The time of lowest T_{air} also differed between sites: While at Schneeberg, on average the air was coldest at 04:38, at Rauher Kulm the time of lowest T_{air} was at 04:55 and at Buchberg at 05:30, though the range of time intervals with lowest T_{air} was large. Schneeberg has the highest elevation and therefore the earliest sunrise as well as the highest wind speeds (Fig. B.1). Sunrise enhances positive, upward buoyancy and high wind speeds increase shear forces, which both reduce dynamic stability. It is therefore likely that the nocturnal stable boundary layer with low T_{air} close to the ground started to dissolve at Schneeberg first.

Θ at a reference elevation of 871 m, the mean elevation of all STHs, was lowest for F5 (Fig. B.9). At the beginning of the night, Θ at Buchberg and Rauher Kulm was higher than Θ at Schneeberg, but decreased faster, reaching similar values toward the end of the night around 04:00–

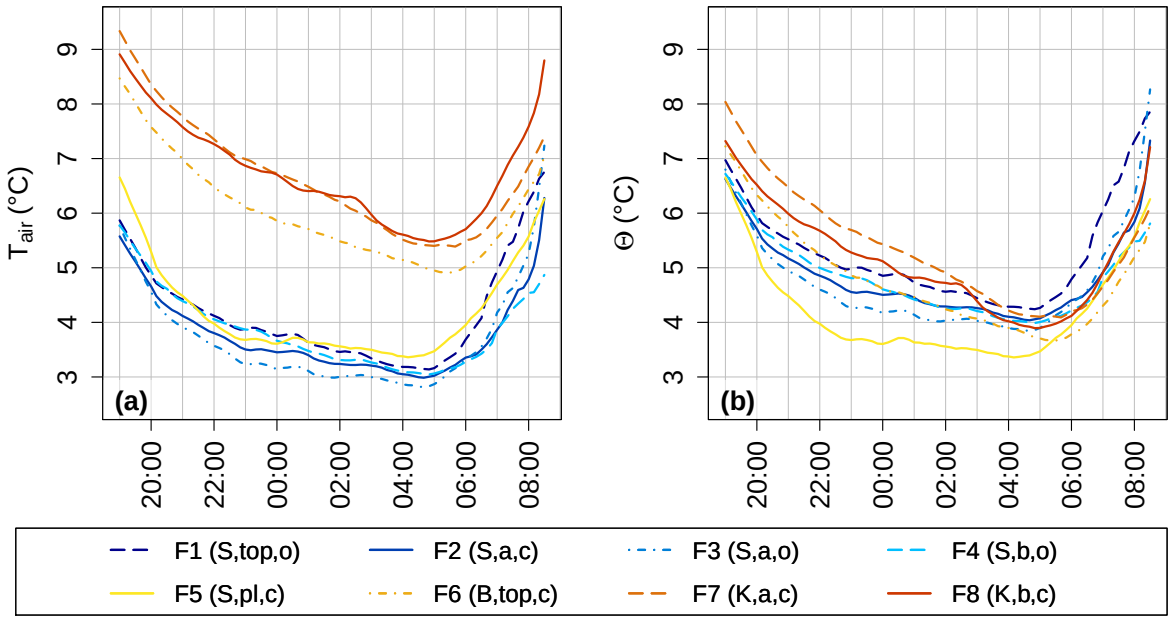

Figure 3.4.: Ensemble averages of (a) air temperature T_{air} and (b) potential temperature Θ per time of day, measured by stationary thermohygrometers (STHs) from 30.04.2019–23.05.2019, with Θ referring to a reference elevation of 871 m above sea level. Parentheses in plot legend describe the location of each STH: S = Schneeberg, B = Buchberg, K = Rauher Kulm, top = summit, a = above block field, b = below block field, pl = plantation, o = open to the sky, c = under canopy.

05:00. At Rauher Kulm, this pattern might be caused by the dark basaltic rock which influences the local energy balance, absorbing the majority of $K\downarrow$ due to its low albedo and converting it into sensible heat. Both McGreevy (1985) and Irmak et al. (2017) found basalt to reach 1.8 K higher $T_{surface}$ and physiologically equivalent temperature, respectively, than the more light-colored granite. These findings fit well with the basaltic rock at Rauher Kulm leading to higher Θ than the granitic rock at Schneeberg during daytime. Additionally, the exposition of the STHs differed between Rauher Kulm and Schneeberg: On Rauher Kulm, the measurements were located on the west side of the mountain, leading to relatively high Θ until sunset, whereas the STHs at Schneeberg were located on a southerly slope which was less sun-exposed in the evening hours. The STH at Buchberg was situated under a thick beech canopy leading to larger $I\downarrow$, keeping the understory from cooling down fast directly after sunset and leading to a higher Θ at Buchberg than at Schneeberg at the beginning of the night until 22:00. Jordan and Smith (1995) also state the presence of a thick canopy cover to impede freezing temperatures from developing in the understory, because the canopy minimizes net radiation losses. However, Θ was lower at Buchberg than at Schneeberg summit from 04:00 to 08:30, indicating the buildup of a large-scale stable stratification throughout the night as expected according to Stull (2017, chap. 18.3). While F5 at the plantation at Schneeberg was situated under beech canopy cover similar to the STH location at Buchberg, the forest structure in the plantation was different from the old-growth forest at Buchberg, with much younger and smaller trees.

In the early morning hours from 04:00 to 08:00, F1 showed the highest Θ of all STH locations, probably due to its elevation and exposed position, where ground was warmed by sunlight

first. Since the STHs were installed only 25–30 cm above the ground, an increase in ground, grass or shrub $T_{surface}$ was recorded by the T_{air} sensors quickly. An impact of $K\downarrow$ onto the T_{air} sensors has to be taken into account, enhancing the outlined effect. However, it can be considered small due to the naturally ventilated double-walled radiation shields housing the sensors.

Theoretically, differences in T_{air} gradients between STHs might also be caused by differences in cloudiness between the three sites. Cloudiness was not recorded; instead, the T_{air} range for each day was used as a proxy, since it can be assumed that the daytime high $K\downarrow$ in combination with the nighttime large positive longwave radiation balance during days with little to no cloud cover cause a large ΔT_{air} between daytime and nighttime. Even though the T_{air} range between the STHs differed, those differences were not site-specific (Fig. 3.5), excluding cloudiness differences as the main factor driving Θ differences.

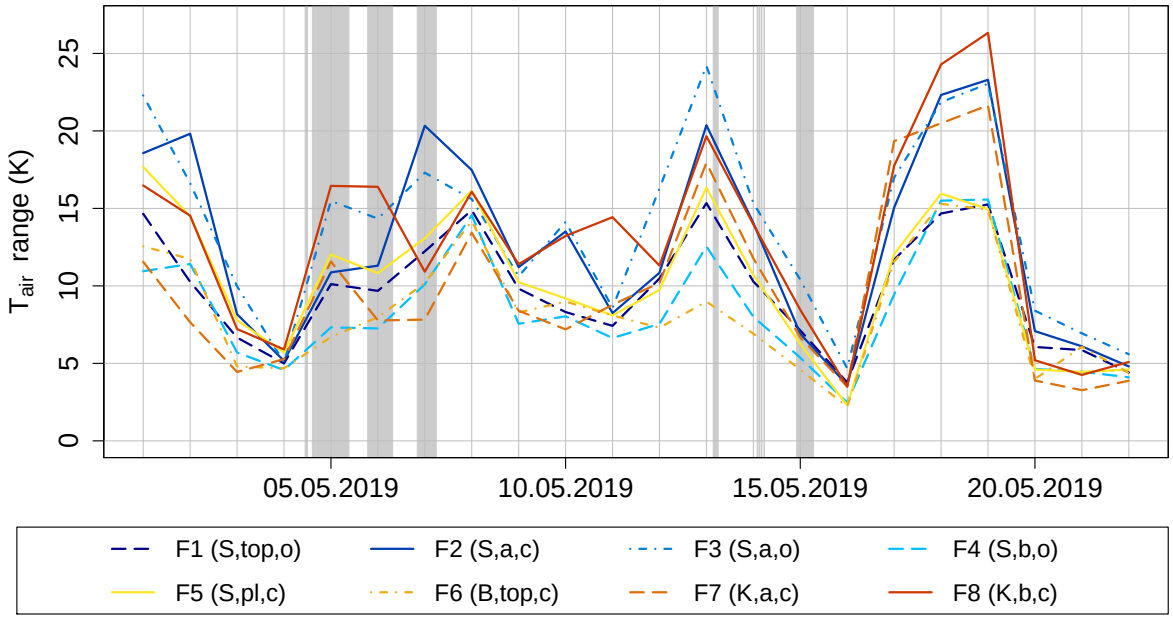

Figure 3.5.: Air temperature T_{air} range per date per stationary thermohygrometer (STH). Grey bars indicate the times with T_{air} at Schneeberg (spatial mean of F1 to F5) below 0 °C. Parentheses in plot legend describe the location of each STH: S = Schneeberg, B = Buchberg, K = Rauher Kulm, top = summit, a = above block field, b = below block field, pl = plantation, o = open to the sky, c = under canopy.

When restricting the data set to the six frost nights, ΔT_{air} between Schneeberg and the two other sites increased (Fig. 3.6 a and B.10).

T_{air} at F3, which was located above the block field in a small clearing, was consistently lower than at the other STHs' locations at Schneeberg. This pattern was also present for all nights, but ΔT_{air} was larger during the frost nights. Apparently, the radiative cooling of the ground was stronger near F3 than near F2 and F5, which were located under canopy, and stronger than near F1 and F4, which were located next to heat-emitting rocks.

The differences in Θ between the sites also increased when restricting the data set to the frost nights, except at the end of the night after 05:00 (Fig. 3.6 b).

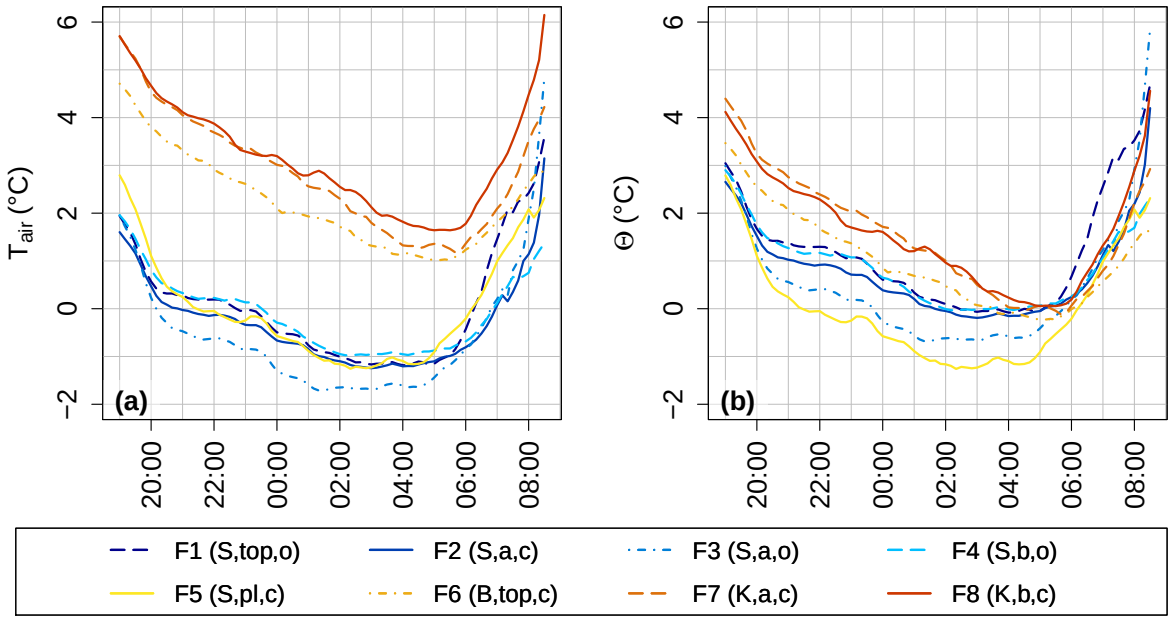

Figure 3.6.: Ensemble averages of (a) air temperature T_{air} and (b) potential temperature Θ per time of day during the frost nights, with Θ referring to a reference elevation of 871 m above sea level. Parentheses in plot legend describe the location of each stationary thermohygrometer: S = Schneeberg, B = Buchberg, K = Rauher Kulm, top = summit, a = above block field, b = below block field, pl = plantation, o = open to the sky, c = under canopy.

On 04.05.2019, a drastic T_{air} drop occurred between 09:30 and 12:00, first at Buchberg, followed by Schneeberg shortly afterwards and by Rauher Kulm one hour later (Fig. 3.7), with T_{air} dropping below 0 °C at Schneeberg. At this time of day, T_{air} should normally have increased instead of decreased according to a normal diurnal cycle. This anomaly is a strong indication for cold-air advection from north to south superimposed onto the diurnal cycle. The shortwave downwelling radiation was still increasing during this period of time according to the weather station at Schneeberg (Fig. B.2), excluding the possibility of the T_{air} drop to be only due to cloud buildup.

A second T_{air} drop then occurred around 18:30 to 20:30, the time of sunset. At Schneeberg, the time of lowest T_{air} was right after sunset at 20:00, though normally, T_{air} drops throughout the night. Possibly, warm-air advection caused the subsequent rise in T_{air}. These findings show that not only diurnal cycles of radiation and energy budgets but also large-scale advection can play a vital role in the development of late-frost conditions at the measuring sites, and in this case lead to freezing temperatures at some measuring locations at Schneeberg lasting for more than 22 h.

3.2.2. Air temperature differences above versus below block field

During nighttime and morning transition (21:10 to 05:50), ΔT_{air} between the top and the bottom of the block field varied from −3 K to +3 K (Fig. 3.8). As the data from the STH locations below the block field (F4 at Schneeberg, F8 at Rauher Kulm) were subtracted from the data from the STH locations above the block field (F2 and F3 at Schneeberg, F7 at Rauher

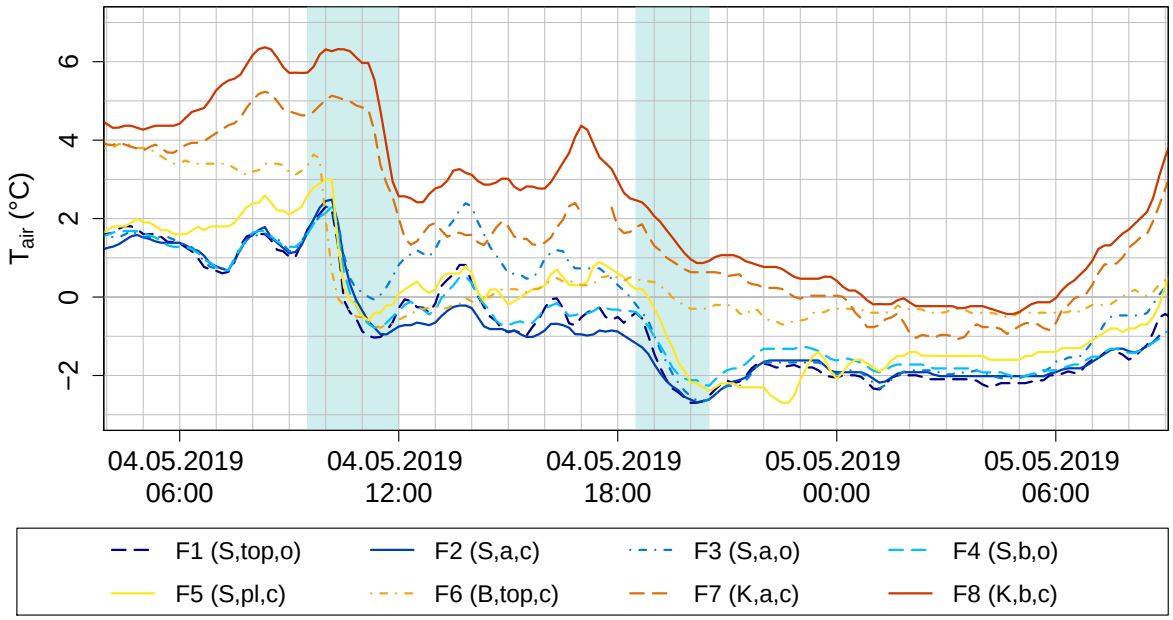

Figure 3.7.: Time series of continuous air temperature T_{air} measurements on 04.05.2019 and 05.05.2019 with periods of interest highlighted in blue. Parentheses in plot legend describe the location of each stationary thermohygrometer: S = Schneeberg, B = Buchberg, K = Rauher Kulm, top = summit, a = above block field, b = below block field, pl = plantation, o = open to the sky, c = under canopy.

Kulm), positive values indicate that it was warmer above the block field, while negative values result from warmer air below the block field. The mean ΔT_{air} for nighttime and morning transition throughout the measuring period was −0.1 K for F2–F4, −0.4 K for F3–F4 and 0.0 K for F7–F8. Therefore, in general, T_{air} was equal or higher below the block fields than above.

This finding is contrary to what was expected in hypothesis II b) as well as contrary to the findings of other studies investigating block fields (Harris and Pedersen, 1998; Popescu et al., 2017; Růžička et al., 2012, 2015; Stiegler et al., 2014; Zacharda et al., 2007). Apparently, cold-air drainage through the blocks leading to lower T_{air} below the block field was not the main nightly process at the two block fields that were investigated in this study. Possibly, the blocks store so much energy during the day that they remain a source of heat all throughout the night. At Rauher Kulm, the absence of the expected T_{air} gradient might also be due to the STHs' location on the west side of the mountain, which was exposed to the generally prevalent westerly winds, pushing the air uphill and effectively suppressing katabatic flows (see chapter 3.1). Another possible reason for the unexpected results of this thesis is that the investigated block fields are not large enough for the typical microclimate to develop, with even the center of the block fields being in the edge effect zone. The block field at Schneeberg had an area of only ∼0.5 ha. Even though the block field at Rauher Kulm, with an area of ∼3.0 ha, was larger, the slope was only 40 m in length. In comparison, the block fields studied by Popescu et al. (2017) had an area of approximately 0.7 ha and 1.5 ha according to the map in their publication, a photograph by Harris and Pedersen (1998) shows their studied block

field to span over a complete mountain slope, and the area of the block fields in the studies of Růžička et al. (2012), Růžička et al. (2015) and Zacharda et al. (2007) was determined using Google Earth as 1.6 ha and 1.9 ha. It was not possible to determine the size of the block field studied by Stiegler et al. (2014), as large parts of their study area were covered by a treeless bog.

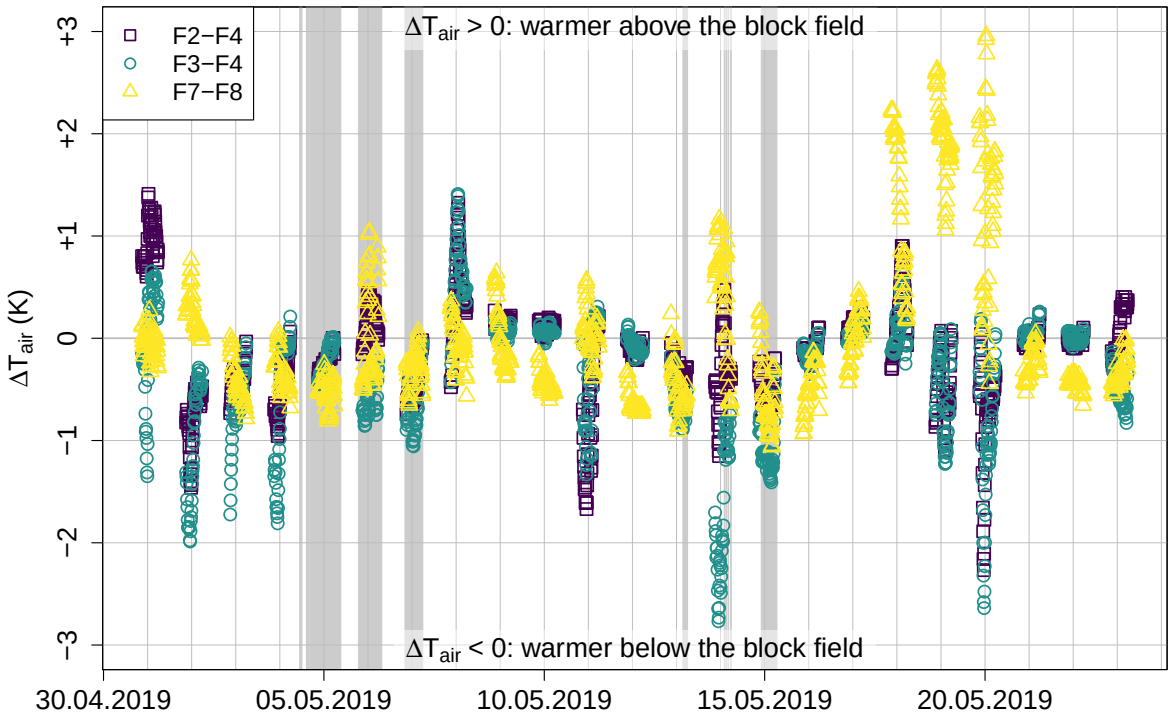

Figure 3.8.: Time series of air temperature differences ΔT_{air} between top (F2, F3, F7) and bottom (F4, F8) of block fields during night and morning transition (21:10 to 05:50). Grey bars indicate the times with T_{air} at Schneeberg (spatial mean of F1 to F5) below 0 °C.

Nighttime and morning transition ΔT_{air} between top and bottom of the block fields also depended on the wind speed at the site (Fig. 3.9). For Schneeberg, wind speed measurements from the weather station on the roof of the former military building were used for the analysis, while for Rauher Kulm, the wind data recorded by the nearest weather station in Hüttstadl was used. The STH difference at Rauher Kulm shows a medium strong trend, whereas the differences at Schneeberg only show weak trends, even though all trends are significant to the 0.001 level of the p-value. ΔT_{air} at Schneeberg was mostly negative for wind speeds $<2.5\,\mathrm{m\,s^{-1}}$, meaning that it was warmer below the block field, whereas for wind speeds between 2.5 and $4.5\,\mathrm{m\,s^{-1}}$, ΔT_{air} exhibited similar positive and negative values in range and abundance. At wind speeds $>6.0\,\mathrm{m\,s^{-1}}$, ΔT_{air} was close to 0 K. Apparently, low wind speeds favored statically unstable atmospheric conditions at this site. The effects of wind speed on block field T_{air} gradients is as yet poorly researched, since studies that take wind speed into account at all focus on its effects on the snow cover (Davesne et al., 2017) or on air movements through snow funnels (Popescu et al., 2017). Only Harris and Pedersen (1998) mention the importance of wind speed for air exchange in-between the blocks, but did not include any wind measurements into their

study themselves. Under weak-wind conditions, sensible heat is not as efficiently transported away from the surface due to a lack of turbulent mixing (Noilhan and Mahfouf, 1996), which might lead to the air near F4 heating up more strongly than near F2 and F3, because location F4 was directly between the blocks at the foot of the block field and the blocks stayed warmer than the surrounding forest throughout the night (see chapter 3.4).

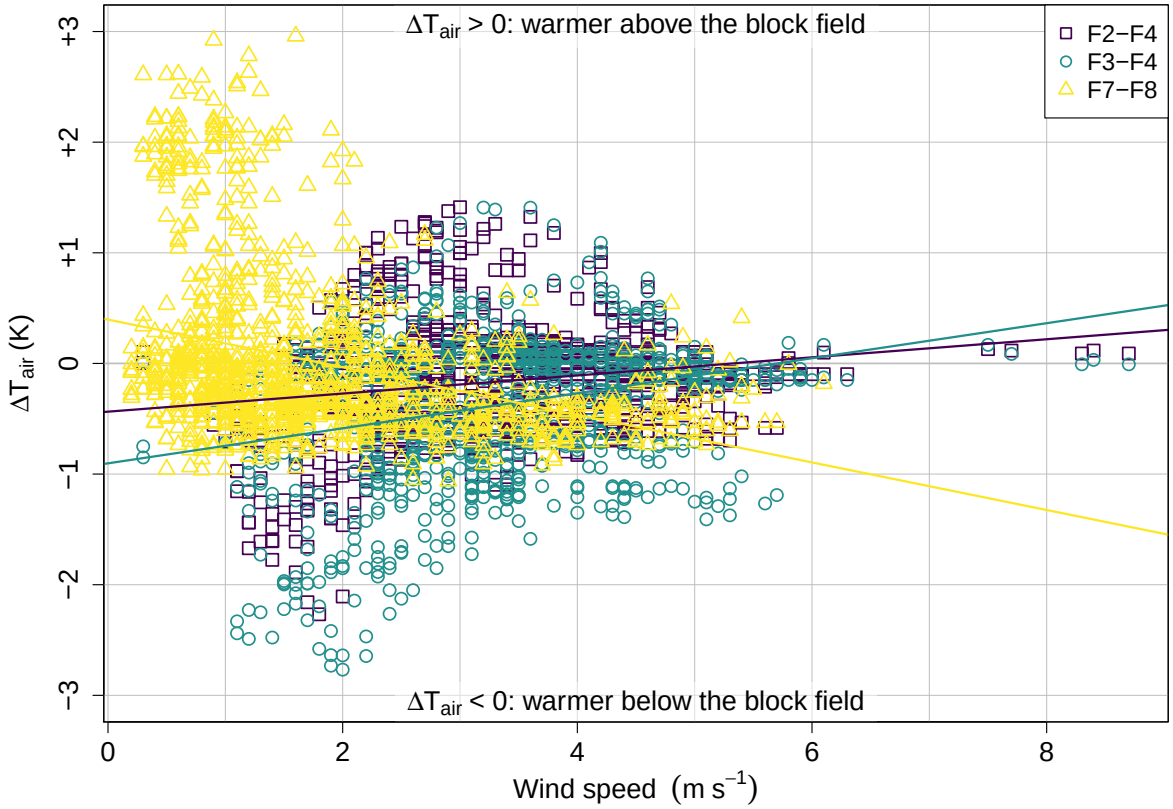

Figure 3.9.: Air temperature differences ΔT_{air} between top (F2, F3, F7) and bottom (F4, F8) of block fields in relation to wind speed at Schneeberg weather station (F2–F4, F3–F4) and at Hüttstadl weather station (F7–F8) during night and morning transition (21:10 to 05:50).

At Rauher Kulm, on the other hand, T_{air} above the block field was up to 3.0 K higher than below during conditions with wind speeds $<2.0\,\mathrm{m\,s^{-1}}$ and on average higher below the block field at times with wind speeds $>2.0\,\mathrm{m\,s^{-1}}$. The expected inversion across the block field thus mostly happened at very low wind speeds, which are probably necessary for local cold-air katabatic flows to develop. However, the flow visualization experiment using artificial fog (see chapter 3.1) showed that an inversion can also be present even though the majority of air flows is in uphill direction due to synoptic advection. Additionally, F7 above the block field at Rauher Kulm was situated under a forest canopy, whereas F8 below the block field was located directly at the border between forest and block field. Thus, differences in wind exposure as well as surface radiation budgets might have caused the measured inversion without actual cold-air drainage happening across the block field. An influence of $K\downarrow$ onto the sensors is unlikely to have caused measurement errors in this case, as only nighttime and morning transition data was used for this analysis and both STHs at Rauher Kulm were stationed on its western slope.

3.3. Multiresolution decomposition

3.3.1. Spatial two-point correlation coefficients

Spatial two-point correlation coefficients R_T, computed for different subsets of the data set (Tab. 2.4), highlight similarities and differences between the stations' T_{air} measurements on different time scales and increase consistently with increasing averaging period: For the 11.25 min scale and the complete data set, the mean R_T of all stations with all other stations was 0.50, whereas for the 24 h scale, the mean R_T was 0.99.

When restricting the results to R_T of the weather station at Schneeberg in comparison to all the STHs, it is shown that across all data subsets, the weather station correlated the most with F1, which was also located nearest to the weather station concerning both spatial distance and elevation (Fig. 3.10). However, R_T did not decrease continuously with decreasing elevation. For both daytime and nighttime data, the weather station correlated more strongly with F4 below the block field at Schneeberg than with F2 and F3 above the block field at Schneeberg, which have a smaller separation distance to the weather station (Fig. 3.10 b–c). This effect appeared across all time scales and was especially pronounced for nighttime data of all nights of the measuring period.

It is probable that this pattern results from dissimilarities in the surroundings of F2 and F3 to the weather station. F2 was located under forest canopy and surrounded by densely growing European blueberry (*Vaccinium myrtillus* L.). During daytime, the trees sometimes provided shade depending on the exact location of the trees and the sun, while the sunlight, when it did reach the blueberry cover, lead to intense heating of the air in the height above ground where the STH was located. During nighttime, when weak-wind conditions prevail, the canopy cover decoupled the air in the understory from the atmosphere above the canopy (Freundorfer et al., 2019). In combination with the canopy's influence on the longwave radiation budget (Jordan and Smith, 1995), T_{air} influencing processes near F2 vary greatly from those at the weather station. F3 was also surrounded by trees, but located in a small clearing. While the reduced canopy cover would suggest a greater R_T with the weather station, which was completely vegetation-free, the R_T with F3 was even smaller than with F2 during nighttime. This small R_T is probably due to the shape of the clearing, which consisted of a small depression in the ground. Especially during cold conditions and in absence of ground-warming sunlight, microtopographic heterogeneities like depressions can lead to cold-air pooling close to the ground. This cold-air pooling causes small-scale stable atmospheric conditions which are decoupled from larger-scale atmospheric processes (Ashcroft and Gollan, 2013). The results fit well with those of Thomas (2011), who also found a strong influence of understory density and local terrain on the observed temporal and spatial variability of T_{air} and wind.

During frost nights, the weather station T_{air} measurements correlated the least with F3 and with F6 at Buchberg (Fig. 3.10 f), underlining the effect of cold-air pooling near F3 and the effect of a dense canopy cover above F6.

The transition periods showed the most contrasting behavior: While R_T was highest during the evening transition, it was lowest during the morning transition (Fig. 3.10 d–e). On the 1.5 h scale, R_T between the weather station and F5 even reached negative values, meaning

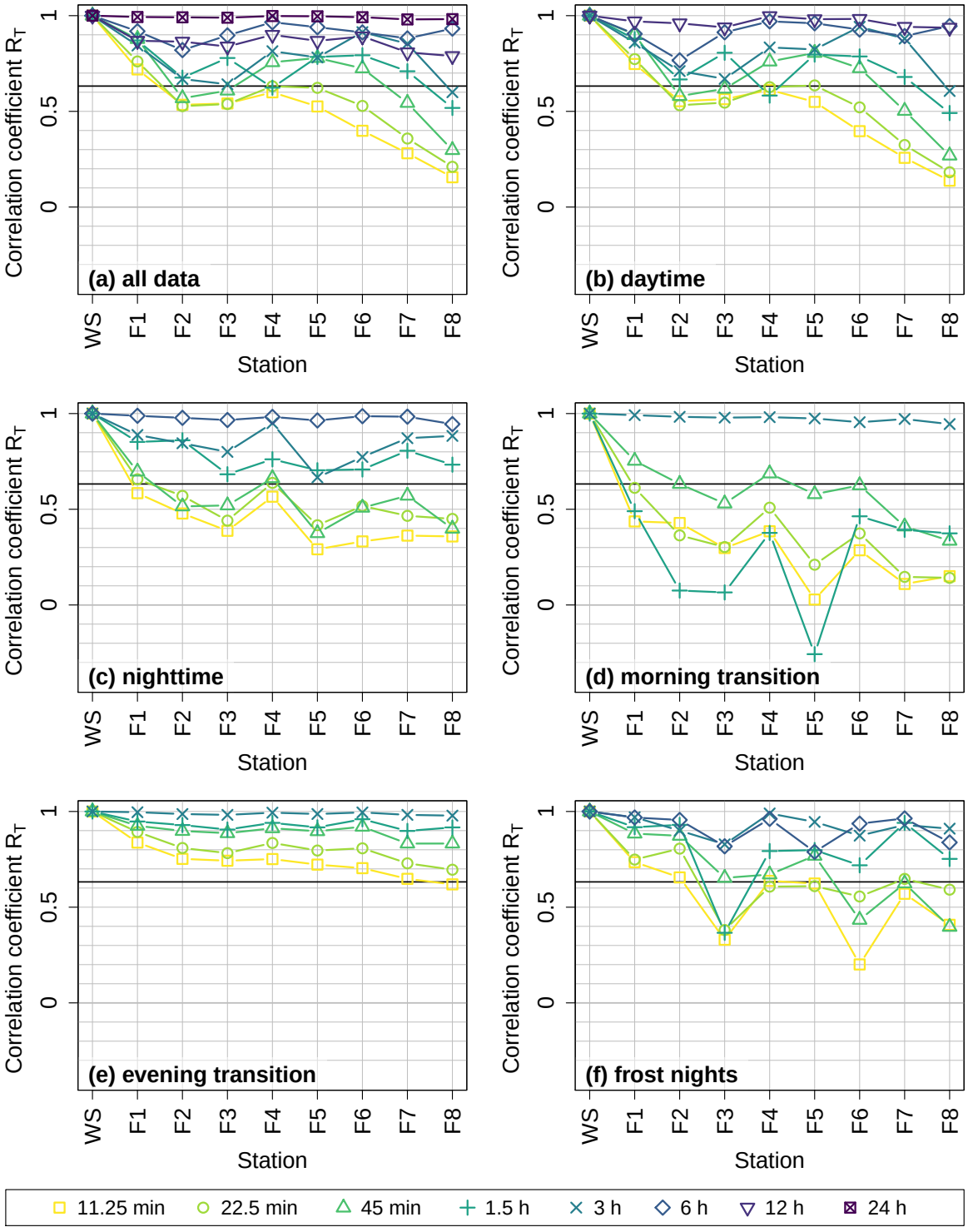

Figure 3.10.: Spatial two-point correlation coefficients R_T obtained by multiresolution decomposition of Schneeberg weather station's air temperature measurements with each of the stationary thermohygrometers. Different temporal scales are presented in different colors. R_T below the black line situated at $1 - \frac{1}{e}$ indicates significant decorrelation. Six different subsets were analyzed: (a) all data (22 d, 06:22:00 to 06:10:45), (b) only daytime (22 d, 06:22:00 to 18:22:00), (c) only nighttime (22 d, 21:33:15 to 03:10:45), (d) only morning transitions (22 d, 03:22:00 to 06:10:45), (e) only evening transitions (22 d, 18:33:15 to 21:22:00), (f) only frost nights (6 d, 21:33:15 to 03:10:45). WS refers to Schneeberg weather station.

they anti-correlated. Probably, the microtopographic differences between the locations lead to location-specific temperature dynamics, decorrelating the signals. Additionally, the sunlight exposition might have played a role. As F5 was located on the northern slope of Schneeberg, it was probably still cooling down while the sunlight already reached the weather station, warming up the air at the summit.

A direct comparison of above and below block field STH measurements with R_T computed for F2, F3, F4, F7 and F8 in comparison to every other station's location instead of only in comparison to the weather station at a 6 h time scale showed that differences in R_T were larger for daytime data than for the complete data set, nighttime data and frost night data (Fig. 3.11). Morning and evening transition were not analyzed because they only encompassed 3 h each. The 6 h scale was chosen to minimize effects of the spatial distance between sites.

F4 and F8, the STH locations below the block fields, had very similar R_T with each of the other stations during the day. At nighttime, the STHs located at the same site had similar R_T to each of the other stations (Fig. 3.11 c). The subset of the frost nights showed unexpected behavior: F3 above the block field at Schneeberg and F8 below the block field at Rauher Kulm had similar R_T with every other station, while F2, F4 and F7 exhibited a pattern similar to each other (Fig. 3.11 d). Since all of the nighttime R_T values were close to 1, the analysis of the complete data set was almost equal to the analysis of the daytime subset (Fig. 3.11 a–b). Apparently, the effect of the block field or other topographic elements on T_{air} development was larger during the day, while at night, the distance in space and/or elevation was the more important factor. This finding is contrary to the expected process of cold-air drainage and the buildup of an inversion across the block field. Cold-air drainage would lead to similar nighttime behavior of STHs in similar positions relative to the block field. However, the nighttime R_T values fit the observed T_{air} gradients across the block fields, which indicate a lack of inversion occurrences especially at Schneeberg (see chapter 3.2.2). The high similarity of R_T of F4 and F8 in comparison to every other station during daytime can be explained with both of these STH locations being situated in direct vicinity of the blocks, which should lead to them rapidly recording the effect of sunlight on the $T_{surface}$ of the rocks, heating up the air nearby under conditions with high $K\downarrow$ (Fig. B.2), whereas the other STH locations were situated several meters away from the block field edge and covered by forest canopy to varying degrees. The unexpected patterns in the frost night subset might well be an artifact of the small data set.

3.3.2. Power spectra

Power spectra, which were computed to analyze the amount of energy contained in each time scale (Fig. 3.12), being equivalent to the amount of temporal variability of T_{air}, showed that the mean spectrum density D_T decreased with increasing frequency f with a slope of approximately $-5/3$. A $-5/3$ slope is expected for the micro-turbulence in the inertial subrange according to the $-5/3$ decay law (Kolmogorov, 1941a,b, Foken, 2017, chap. 1.4.3). However, the period lengths analyzed mostly lie within the mesoscale influenced by the diurnal cycle. Here, a spectral peak is expected for period lengths of ∼6 h (Roedel and Wagner, 2017, chap. 6.3.3). This peak was detected for daytime data gathered by the STHs (Fig. 3.12 b). Furthermore, for daytime, evening transition and the complete data set, the weather station at Schneeberg

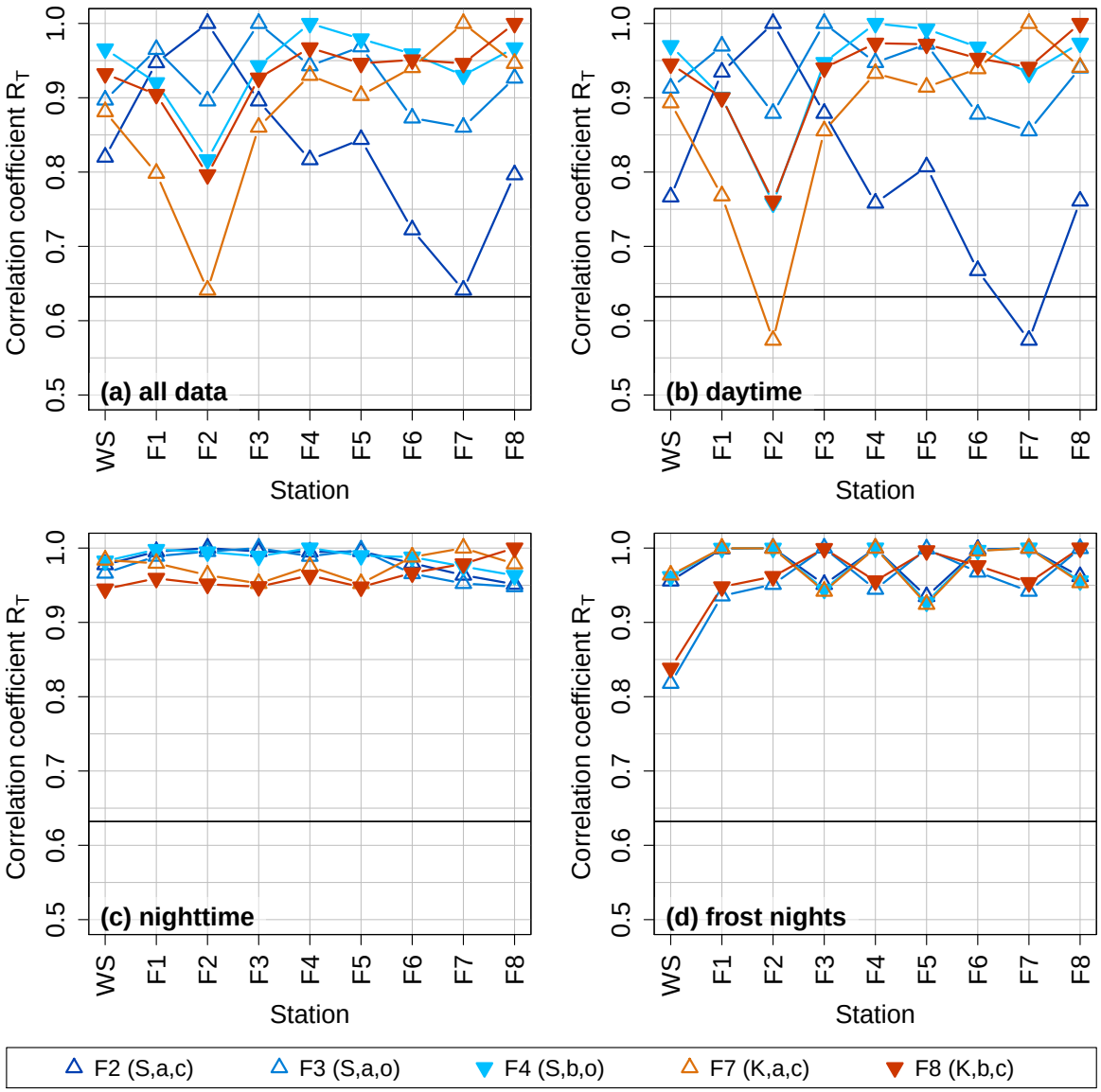

Figure 3.11.: Spatial two-point correlation coefficients R_T obtained by multiresolution decomposition of five stationary thermohygrometers (STHs)' air temperature measurements in comparison to every other station at the 6 h time scale. Blue lines represent STHs at Schneeberg, orange lines represent STHs at Rauher Kulm. Empty, upwards pointing triangles indicate STHs located above the block field, filled, downwards pointing triangles indicate STHs located below the block field. R_T below the black line situated at $1 - \frac{1}{e}$ indicates significant decorrelation. Four different subsets were analyzed: (a) all data (22 d, 06:22:00 to 06:10:45), (b) only daytime (22 d, 06:22:00 to 18:22:00), (c) only nighttime (22 d, 21:33:15 to 03:10:45), (d) only frost nights (6 d, 21:33:15 to 03:10:45). Parentheses in plot legend describe the location of each STH: S = Schneeberg, K = Rauher Kulm, a = above block field, b = below block field, o = open to the sky, c = under canopy. WS refers to Schneeberg weather station.

exhibited a distinctly lower D_T across all frequencies (Fig. 3.12 a, b, e). This lack in T_{air} variance might have several reasons: For one, the weather station's measurement technology is less prone to longwave radiation errors than the STHs. For another, the building on whose roof the weather station was located has a large heat storage capacity, weakening the temporal T_{air} variability. Lastly, the weather station was located in a very exposed position with high wind speeds leading to strong turbulent mixing, which also reduced the temporal variability of T_{air} at the investigated time scales. In general, D_T was largest during the day, where the differences between the stations also were largest (Fig. 3.12 b). During nighttime, D_T was lower and almost the same for all stations (Fig. 3.12 c). The generally lower D_T at night implies stronger atmospheric mixing during the day than at night, which fits the common process of a stable nocturnal boundary layer with minimum turbulence. As D_T for all stations was similar at night, the nocturnal processes of stabilization of stratification and cessation of wind-inducing air density differences affected all stations equally, irrelevant of site, vegetation cover and position in relation to the block field. It was unclear whether the summit of Schneeberg would be affected by a low-level jet during the night, with high wind speeds above the friction-reducing stable surface layer. Serafimovich et al. (2017) detected occasional low-level jets at the nearby Waldstein research site in the Fichtelgebirge mountains and Loos (2016) found low-level jets to develop above the valley north of Schneeberg. Holden (2016) found no significant changes in wind direction and speed within the lowest 200 m above the Schneeberg summit, which indicates the absence of low-level jets above Schneeberg. This finding fits the results of the power spectrum analysis showing that the weather station at Schneeberg summit had a very similar variance to the other stations, meaning that it was probably not influenced by a low-level jet.

After normalizing the spectra by dividing by the variance σ_T^2 and multiplying by the frequency f, all subsets except for the evening transition exhibited a spectral peak, situated at 1.5 h (nighttime, morning transition) and 6 h (daytime), respectively (Fig. 3.13). Only for higher frequencies, which means shorter period lengths, than 1.5 h, the spectra showed a decay of approximately $-2/3$ with increasing frequency as expected for normalized spectra for the inertial subrange (Kolmogorov, 1941a,b, Foken, 2017, chap. 2.5). Since sub-canopy turbulence depends on shear generation of above-canopy turbulence which is transported downwards (Vickers and Thomas, 2013), the different energy decay during the evening transition might be due to the mechanically induced turbulence by shear forces which prevail during this time of day with highly variable and fast-changing wind directions and speeds in different heights, which matches findings by Fernando et al. (2013) and Chen et al. (2017). The high variability during the frost nights indicates microclimatic deviations between STHs.

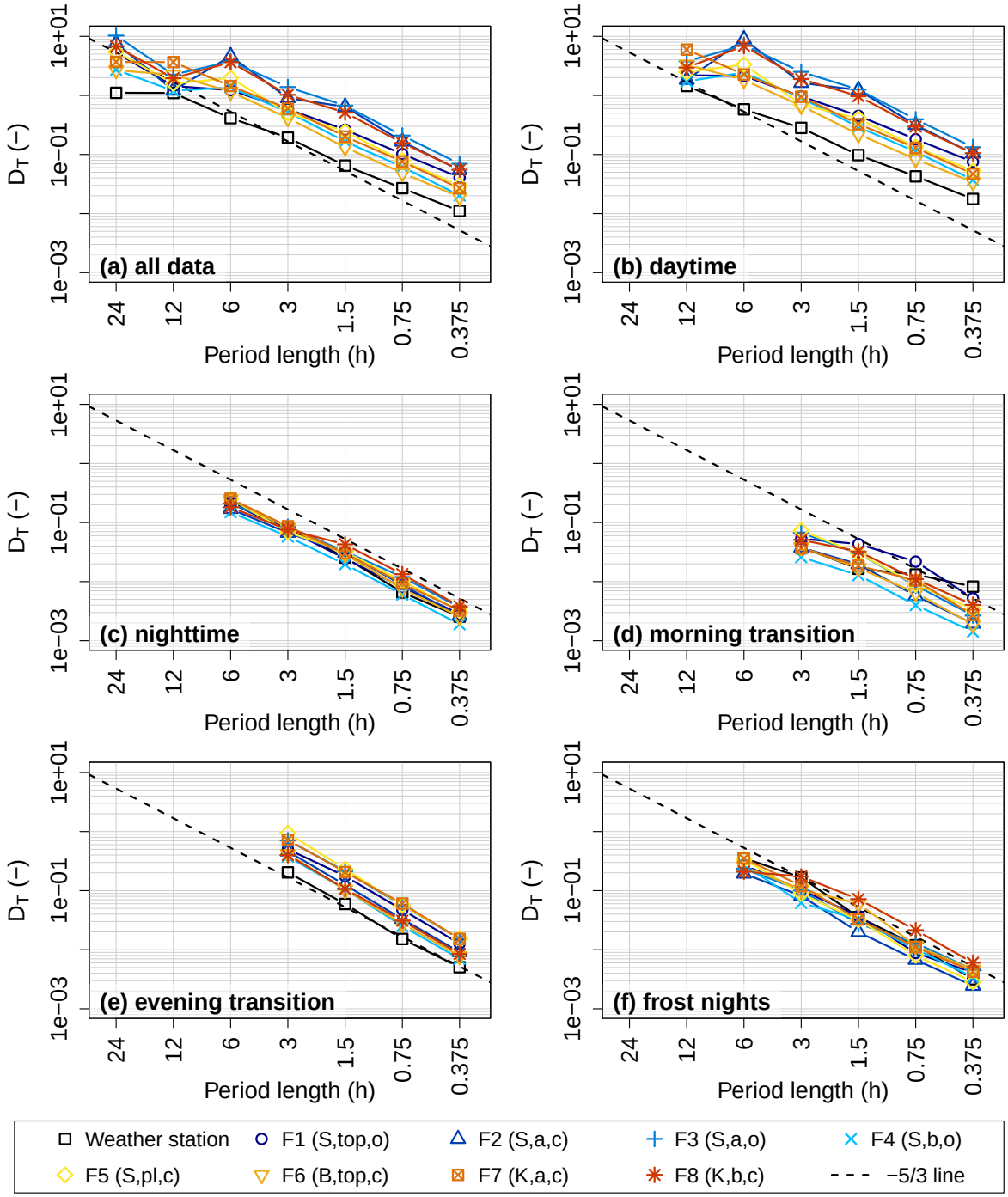

Figure 3.12.: Power spectra of air temperature obtained by multiresolution decomposition showing the mean spectrum density D_T per period length. Different temporal stations are presented in different colors. Six different subsets were analyzed: (a) all data (22 d, 06:22:00 to 06:10:45), (b) only daytime (22 d, 06:22:00 to 18:22:00), (c) only nighttime (22 d, 21:33:15 to 03:10:45), (d) only morning transitions (22 d, 03:22:00 to 06:10:45), (e) only evening transitions (22 d, 18:33:15 to 21:22:00), (f) only frost nights (6 d, 21:33:15 to 03:10:45). Parentheses in plot legend describe the location of each STH: S = Schneeberg, B = Buchberg, K = Rauher Kulm, top = summit, a = above block field, b = below block field, pl = plantation, o = open to the sky, c = under canopy. WS refers to Schneeberg weather station.

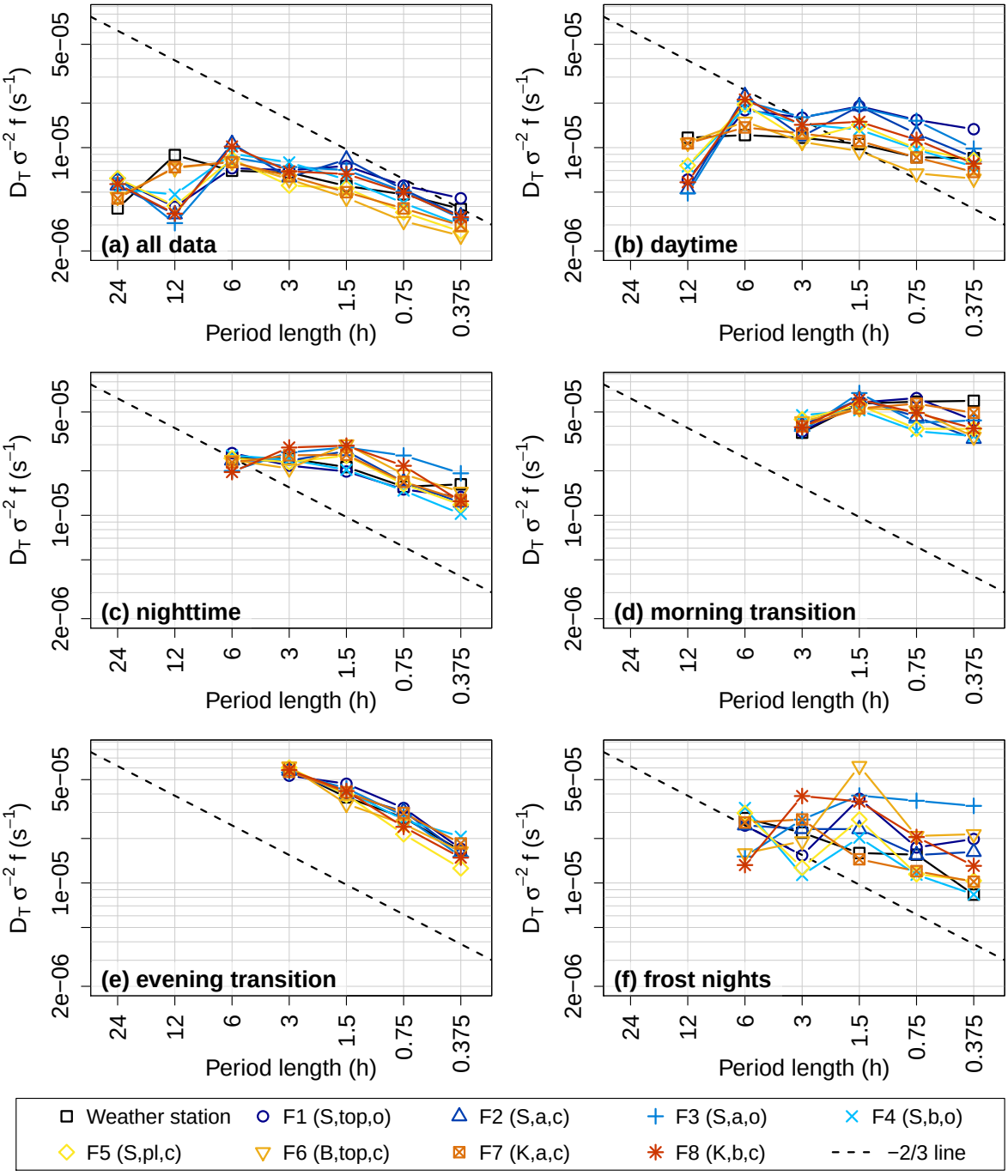

Figure 3.13.: Power spectra of air temperature obtained by multiresolution decomposition showing the mean spectrum density D_T per period length, normalized by dividing by the variance σ_T^2 and multiplying by the frequency f. Different temporal stations are presented in different colors. Six different subsets were analyzed: (a) all data (22 d, 06:22:00 to 06:10:45), (b) only daytime (22 d, 06:22:00 to 18:22:00), (c) only nighttime (22 d, 21:33:15 to 03:10:45), (d) only morning transitions (22 d, 03:22:00 to 06:10:45), (e) only evening transitions (22 d, 18:33:15 to 21:22:00), (f) only frost nights (6 d, 21:33:15 to 03:10:45). Parentheses in plot legend describe the location of each STH: S = Schneeberg, B = Buchberg, K = Rauher Kulm, top = summit, a = above block field, b = below block field, pl = plantation, o = open to the sky, c = under canopy. WS refers to Schneeberg weather station.

3.4. Hand-held air temperature measurements

On each of the four days where hand-held T_{air} measurements were conducted, the mean T_{air} recorded by the MTH at 20 cm was higher than or equal to T_{air} at 2 m height, indicating there was no nighttime surface-based inversion (Tab. 3.1). The mean ΔT_{air} between the 20 cm and the 2 m height measurements ranged from 0.0 K on 14.05.2019 to 0.3 K on 05.05.2019. After calculating the mean of the 10 measurements per height above ground, day and location, a Shapiro-Wilk normality test showed that the data subsets of each day and measuring height were normally distributed. Therefore, a paired, two-sided t-test was performed on the data of the two measuring heights. It revealed that for three of the four nights, the differences between the measuring heights were significant to the 0.05 level of the p-value, while on 14.05.2019, there was no significant difference.

Table 3.1.: Mean air temperature T_{air} per day and measuring height recorded by the mobile thermo-hygrometer, p-value of Shapiro-Wilk normality test and p-value of paired, two-sided t-test.

night	mean T_{air} (°C) at 20 cm	mean T_{air} (°C) at 200 cm	p-value Shapiro-Wilk (20 cm)	p-value Shapiro-Wilk (200 cm)	p-value t-test
05.05.2019	−1.8	−2.1	0.70	0.66	4.22×10^{-6}
07.05.2019	−0.2	−0.3	0.27	0.63	0.02
14.05.2019	0.6	0.6	0.15	0.13	0.92
15.05.2019	−1.1	−1.2	0.47	0.97	0.04

3.4.1. Mean of all days

The hand-held T_{air} measurements, which allowed for a higher spatial resolution than the temporally continuous measurements, showed that the warmest part of the measuring site during the frost nights was usually the block field (Fig. 3.14), contrary to hypothesis II a). This finding shows that the large heat-storage capacity of the blocks has a stronger impact on T_{air} than the absence of a canopy that would provide higher $I \downarrow$ than the bare night sky. Jordan and Smith (1995), on the other hand, state sky exposure to be the main factor influencing frost occurrence, though they did not use a block field for a comparison to a forested area.

In general, it was warmer below the block field than above, in accordance with the temporally continuous T_{air} measurements (see chapter 3.2.2) and contrary to hypothesis II b). Therefore, there was usually no inversion between above- and below-block field areas during the frost nights. Studies investigating block fields usually find colder air downslope of the block field, not above (Harris and Pedersen, 1998; Popescu et al., 2017; Růžička et al., 2012, 2015; Stiegler et al., 2014; Zacharda et al., 2007).

The lowest T_{air} occurred at the three beech trees number 1 to 3 above the block field. While at 20 cm height above ground the low T_{air} might have been due to the blueberry cover, these measuring locations were also the coldest at 2 m height. It was assumed that the few beech trees which grow at the site would be situated at the warmest parts of the site, hence the lack of beeches in the rest of the forest surrounding the block field. However, the result that T_{air} was lowest near the beeches contradicts this assumption. Thus, it is highly probable that

beeches would be able to grow everywhere in this area, which is of high importance for future forest management.

The current absence of beeches at the rest of the study site is therefore not due to unfavorable conditions; instead, a mere coincidence of a few beech-nuts reaching the forest above the block field seems to be the cause of the present distribution of beeches at the site.

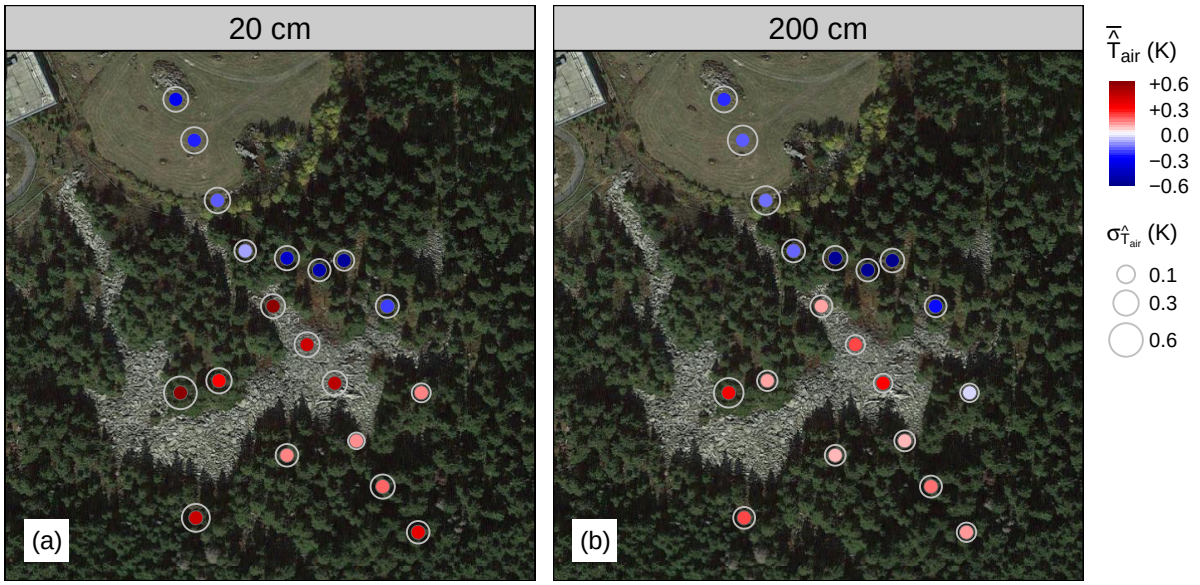

Figure 3.14.: Temporal mean of spatial perturbations and standard deviation σ of spatial perturbations of air temperature T_{air} of the four measuring days at (a) 20 cm and (b) 2 m height above ground at Schneeberg. (Base map: © 2021 Google, © 2021 GeoBasis-DE/BKG)

3.4.2. Data for each day

For a better understanding of the variation in T_{air} perturbations from day to day, the perturbations were analyzed for each single measuring day (Fig. 3.15), showing that the largest perturbations occurred on 05.05.2019 with +1.4 K to −0.8 K deviation from the mean at 20 cm height above ground (Fig. 3.15 a) and +0.8 K to −0.9 K deviation at 2 m height (Fig. 3.15 b). The smallest perturbations occurred on 07.05.2019 with +0.6 K to −0.4 K deviation from the mean at 20 cm height above ground (Fig. 3.15 c) and +0.3 K to −0.4 K deviation at 2 m height (Fig. 3.15 d). The standard deviation σ_T of the 10 measurements per location was usually smallest for the uppermost measurement locations (T07 to T10, T16 to T18; Fig. 2.2) and largest for the westernmost locations (T13 to T15) and the locations on the block field (T03 to T06).

An inversion only occurred on 14.05.2019, when the air at the measuring locations above the block field (T07 to T10) was slightly warmer than at those below (T01 to T02), though the locations of the beech trees (T16 to T19) were still the coldest (Fig. 3.15 e–f). However, the block field was still the warmest part of the site on this day (T03 to T06). On 07.05.2019, the block field was not warmer than the surrounding area, though. This day was also the day with the least spatial ΔT_{air} between measuring locations. Interestingly, neither were wind speeds on this day particularly high (Fig. B.1), which would have induced strong turbulent mixing,

nor was the day before the measuring night particularly cloudy (Fig. B.2), which might have explained the lack of heat stored by the blocks. On the other three measuring days, the warming effect of the block field was much more pronounced for the 20 cm measurements than the 2 m measurements. The vertical T_{air} gradient at T03 to T06 suggests that the air above the block field was warmed by the heat-storing blocks.
T16 to T18, where three of the four beech trees were located, were among the coldest measuring locations every single day, indicating that the mean T_{air} value of the four measuring days being the lowest at these locations as seen in Fig. 3.14 was not due an extreme outlier.

3.4.3. Difference between the measuring heights

On 05.05.2019, ΔT_{air} between the 2 m and the 20 cm height measurements was $\leq$0.0 K for every measuring location, meaning that the stratification in the 2 m above ground was neutral to statically unstable. On all other days, there were varying numbers of measuring locations with positive ΔT_{air} (Fig. 3.16 b–d). Especially the uppermost locations (T08 to T10) exhibited a statically stable stratification on each of the measuring days except for the first. Possibly, the uninhibited surface radiative cooling of the flat, grassy surface near Schneeberg summit created a small-scale inversion, whereas the rest of the measuring locations either had reduced radiative net losses due to longwave radiation coming in from the canopy or air heated by the warm blocks.
The largest amount of measuring locations with a statically stable stratification in the 2 m above ground occurred on 14.05.2019, the same day where the locations above the block field were warmer than below the block field (Fig. 3.15 e–f). According to the weather station at Schneeberg, wind speed was very low during this night, leading to a lack of turbulent mixing and providing perfect conditions for the development of an inversion layer close to the ground. Of the four measuring locations on the block field, the uppermost one (T06) stood out as having the strongest negative ΔT_{air} between the two measuring heights, especially on 14.05.2019 and 15.05.2019 (Fig. 3.16 c–d). T06 was the most sheltered measuring location on the block field, with large blocks surrounding it on all sides and apparently heating the air inside the small hollow they created. Thus, there was a larger difference to the air at 2 m height than at locations T03 to T05, which were more exposed.

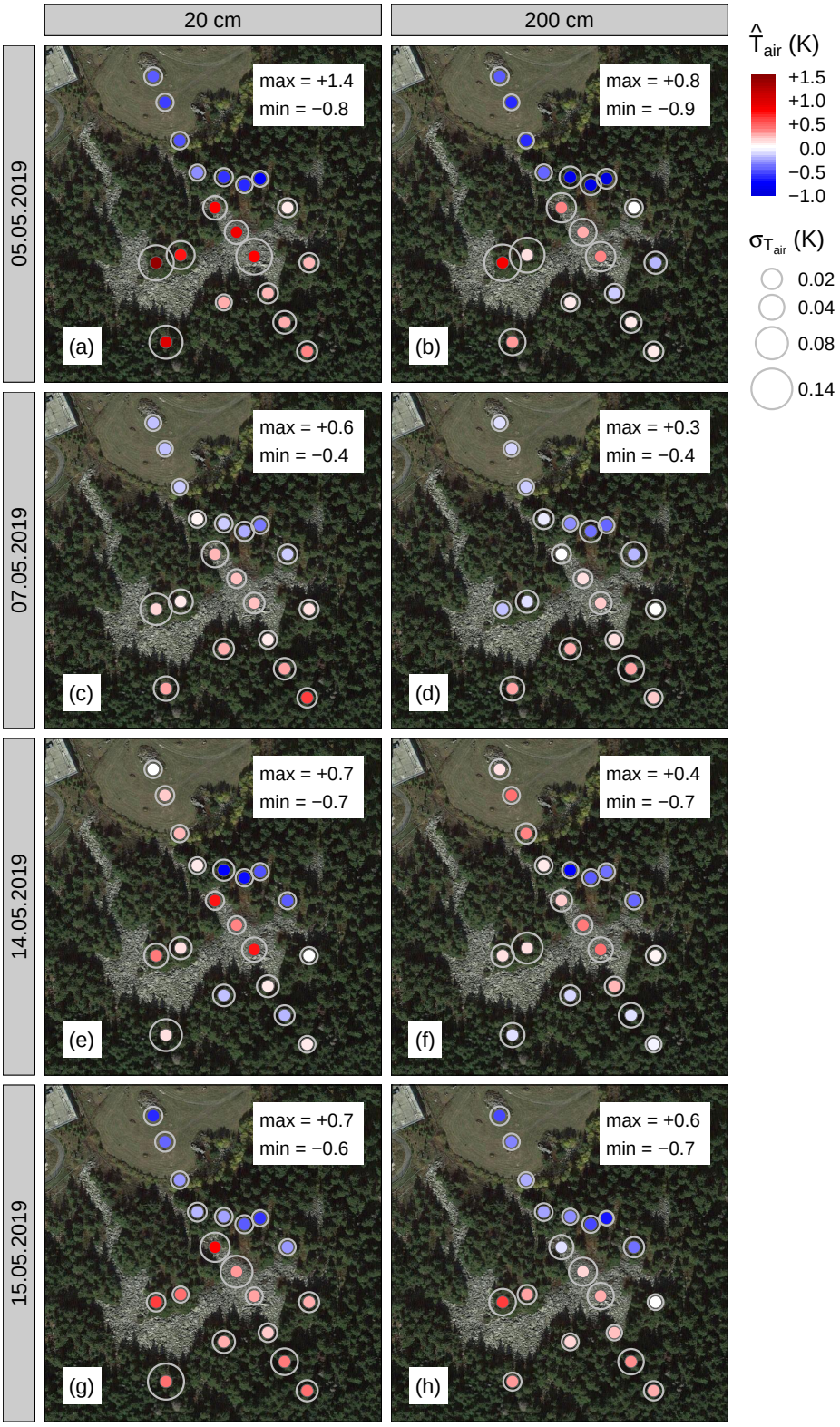

Figure 3.15.: Spatial air temperature T_{air} perturbations per day and measuring height, gained by subtracting the mean T_{air} of both heights per day (05.05.2019: −2.3 °C, 07.05.2019: −1.6 °C, 14.05.2019: 0.3 °C, 15.05.2019: −1.7 °C) from the mean of the 10 measurements per location to allow for comparison of the two heights. The standard deviation σ_T was also calculated using the 10 measurements per location. Max and min refer to the maximum and minimum perturbation from the mean per day and measuring height. (Base map: © 2021 Google, © 2021 GeoBasis-DE/BKG)

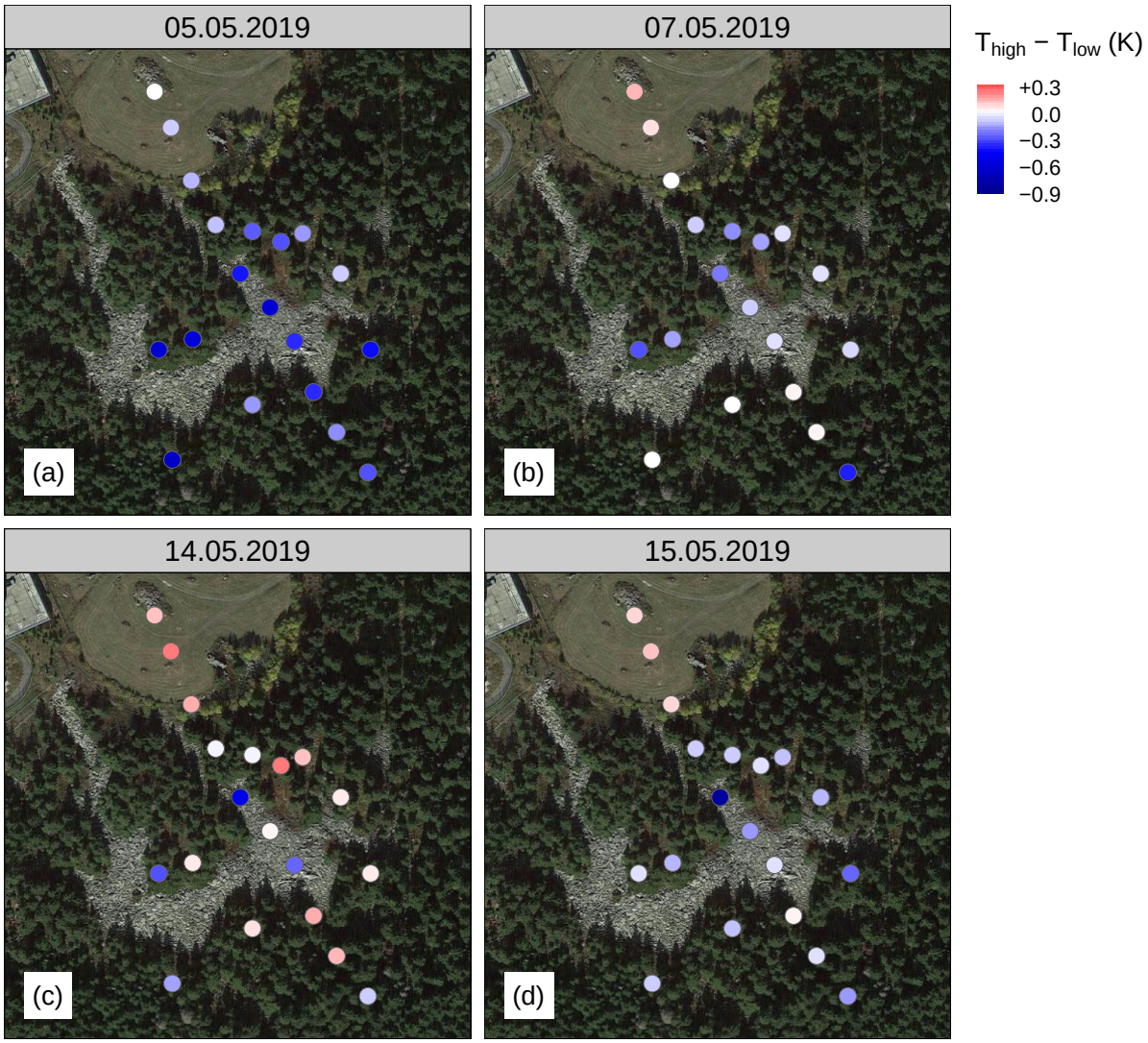

Figure 3.16.: Difference between air temperature at 2 m height (T_{high}) and 20 cm height (T_{low}) above ground for each measuring day. Red indicates that it was warmer at 2 m height, blue means that it was warmer at 20 cm height. (Base map: © 2021 Google, © 2021 GeoBasis-DE/BKG)

3.5. Canopy surface temperature

Longwave radiation is of high importance to plant tissue (Jones and Rotenberg, 2001). Therefore, the T_{air} measurements were accompanied by $T_{surface}$ measurements taken with an IR camera.

On average, the forest canopy $T_{surface}$ was higher below the block field than above (Fig. 3.17), as was T_{air} (see chapter 3.4). A possible explanation is that since the rocks are generally warmer than the forest (see chapter 3.4), they emit more longwave radiation which heats up the forest edge. The angle between the block field slope and the forest edge below is <90°, whereas the angle with the uphill forest edge is >90°. Therefore, the lower forest edge receives more of the $I\uparrow$. Only on 07.05.2019, $T_{surface}$ of the canopy above the block field was higher, whereas T_{air} was higher above the block field only on 14.05.2019 (Fig. 3.15). Therefore, the heating effect of the block field cannot explain all the differences in forest T_{air}. Instead, a complex interplay between $I\uparrow$ and various other factors influence the local stratification of the atmosphere: Clouds increase $I\downarrow$, reducing the positive nighttime longwave radiation balance; high wind speed or direction differences between layers generate shear and enhance turbulent mixing, increasing the sensible heat flux; and the large-scale synoptical situation drives air flow across the block field (see chapter 3.1).

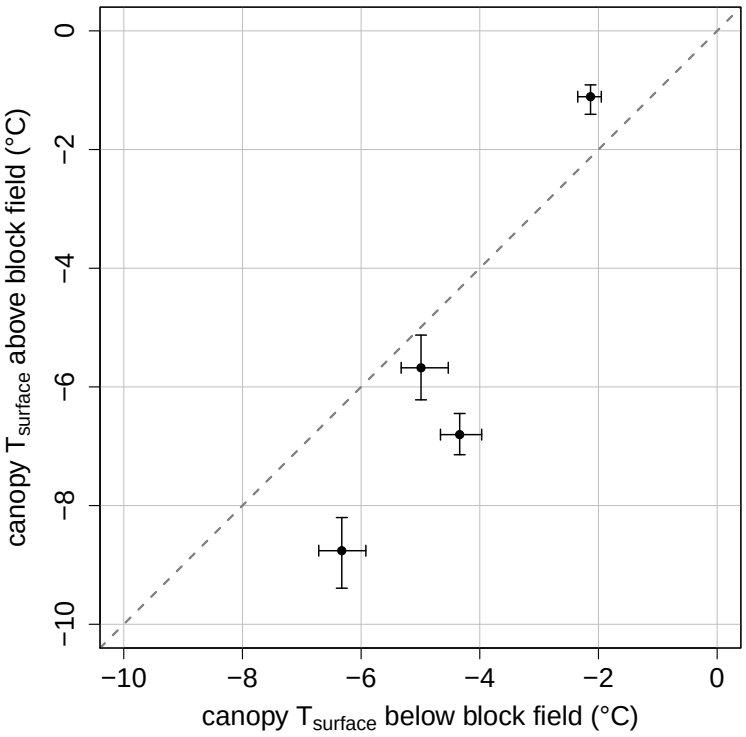

Figure 3.17.: Relation between above block field and below block field canopy surface brightness temperature $T_{surface}$. Each point represents one day. The error bars contain the 0.05 and 0.95 quantiles of pixel values.

3.6. Beech development

3.6.1. Bud growth

Three of the beech trees had buds that had not yet started bursting at the beginning of May 2019. A linear model of the length measurements of these buds between 30.04.2019 and 15.05.2019 revealed that the buds grew on average $0.57\,\mathrm{mm\,d^{-1}}$. The measurements showed bud length to stay the same or even decrease shortly after frost events (Fig. 3.18). Since bud length decreasing is unlikely, this finding is most probably due to measurement errors. Bud length of beech number 7 increased with a similar rate to beeches number 2 and 3 despite being located in the plantation rather than at the summit. The similar growth rate suggests that the beeches from the two measuring locations can be treated as a single sample.

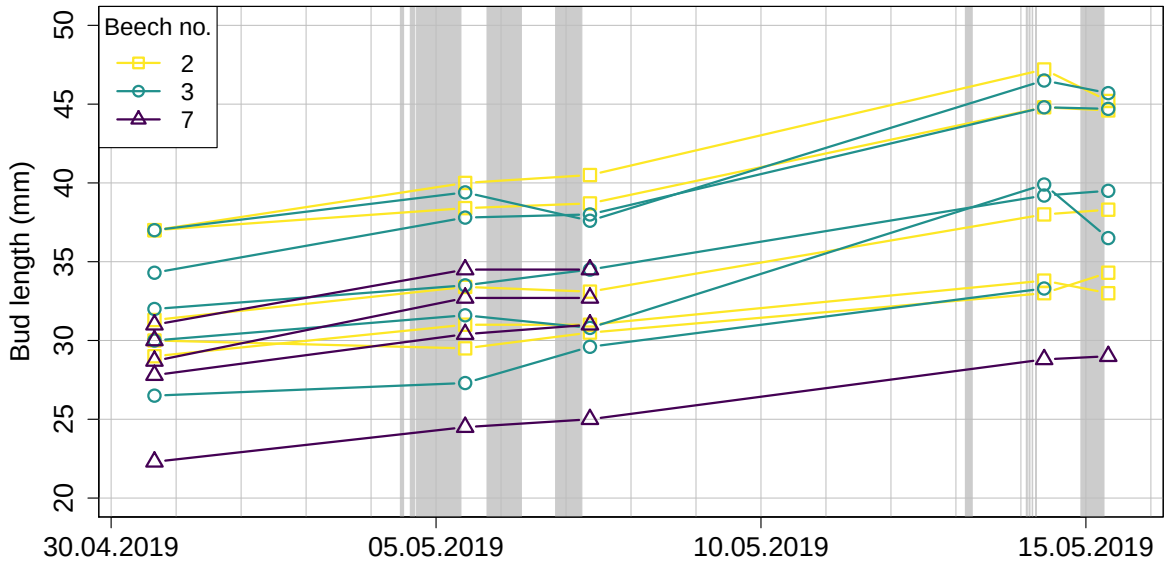

Figure 3.18.: Bud length development during the first half of May 2019. Even though five branch tips per tree were selected, represented here are only the buds in the phenological stages of the Biologische Bundesanstalt, Bundessortenamt und Chemische Indsturie in categories 00–03 and 07 (before buds showed green tips or leaves unfolded). Beeches number 1, 5 and 6 did not have any buds in these phenological stages at the time of measurement. Grey bars indicate the times with air temperature at Schneeberg (spatial mean of F1 to F5) below 0 °C.

3.6.2. Phenology

On 05.05.2019, the first day of late frost, the leaves of trees number 1 at Schneeberg summit and number 5 and 6 in the plantation had at least partly unfolded their leaves (Fig. 3.19). On the last day of late frost, 15.05.2019, additionally tree number 7 at the plantation had started spreading its leaves. Trees number 2 and 3 near the block field were still just beginning to break their buds. Urban et al. (2015) recorded a 21-year average of 8 d between the first leaves in a stand being partially unfolded and all leaves in the stand being partially unfolded; furthermore, they state the interval between 0 % and 100 % of leaf area in the stand to be 28 d. Their measurements took place in a 45-year-old European beech forest in the Czech Republic.

Marchand et al. (2020) state the inter-individual variability of beech bud burst to be 13 d at two sites in Belgium and the variability to correlate most strongly with the timing of cessation of wood formation in the previous autumn. Similarly, Menzel et al. (2015) give a range of 12 d for the timing of leaf unfolding among beech trees in the Bavarian Forest national park, Germany. The beeches investigated in this thesis varied more in their timing of leaf-out, at least where leaf unfolding is concerned (the variability in the timing of bud burst could not be analyzed because observations only started when four of the six beeches had already started bud burst). While on 30.04.2019, only beech number 5 had partly spread apart its leaves (BBCH category 10), two weeks later only beeches number 1 and 6 as well as one of the five investigated branches of beech number 7 had reached the same or more advanced phenological stages. Since the beeches at both the summit and at the plantation exhibited similar variability in leaf-out, the differences in tree phenology do not stem from the summit versus plantation location but are the normal variance within a single sample. This finding is also in accordance with Heide (1993), who found four different ecotypes from provenances between 47° N and 59° N in latitude and 10–600 m a.s.l. in altitude to respond very similarly to day length for the timing of bud burst.

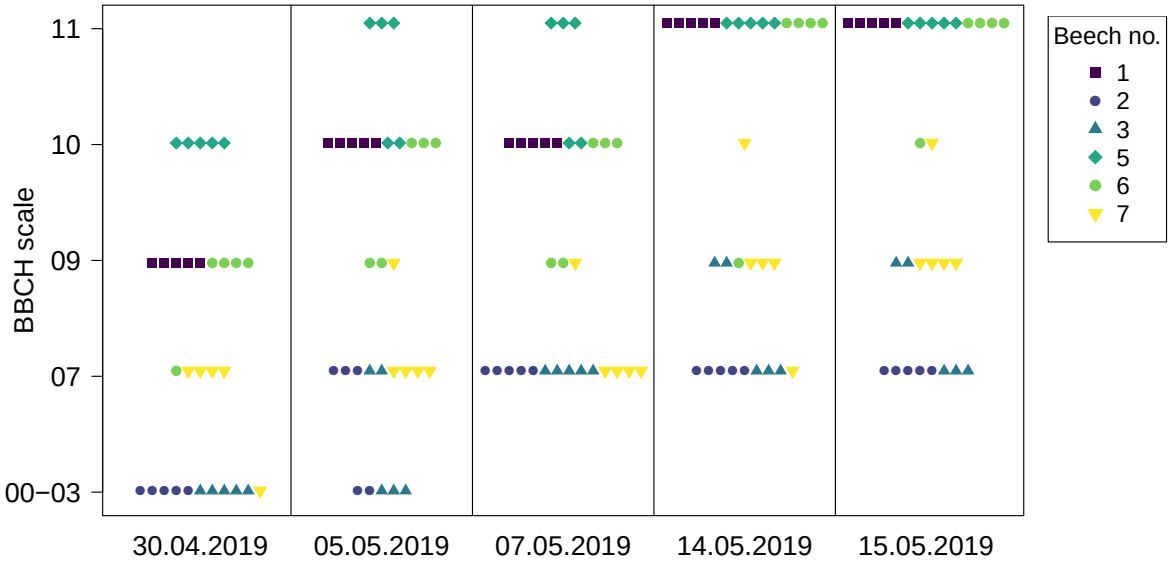

Figure 3.19.: Phenological stage of beech buds at each of the measuring days. The Biologische Bundesanstalt, Bundessortenamt und Chemische Indsturie (BBCH) scales represent the following phenological stages: BBCH code 00–03: winter dormancy, beginning of bud swelling, end of bud swelling, BBCH code 07: beginning of bud breaking, BBCH code 09: buds show green tips, BBCH code 10: first leaves spread apart, BBCH code 11: first leaves unfolded. Beeches number 1 to 3 were located at the summit of Schneeberg near the block field, trees number 5 to 7 were located on the northern slope of Schneeberg in a beech plantation.

3.6.3. Frost damage

When comparing the frost damage each beech suffered to the phenological stage the trees were in at the last day of frost, it is apparent that only the leaves which had already completely

unfolded (BBCH category 11) received substantial damage (Fig. 3.20). The terminal buds which were in BBCH categories 7–10 had a maximum of 5 % damaged leaf tissue. Beech number 1, which was located at the summit of Schneeberg, received much more frost damage than beeches number 5 and 6 at the plantation, even though T_{air} at the plantation was similar to the summit (see chapter 3.2.1). The minimum T_{air} at the summit was −2.7 °C, with T_{air} < − 2.0 °C lasting for 5.5 h; whereas the minimum T_{air} at the plantation was −2.8 °C, with T_{air} < − 2.0 °C for the same time period.

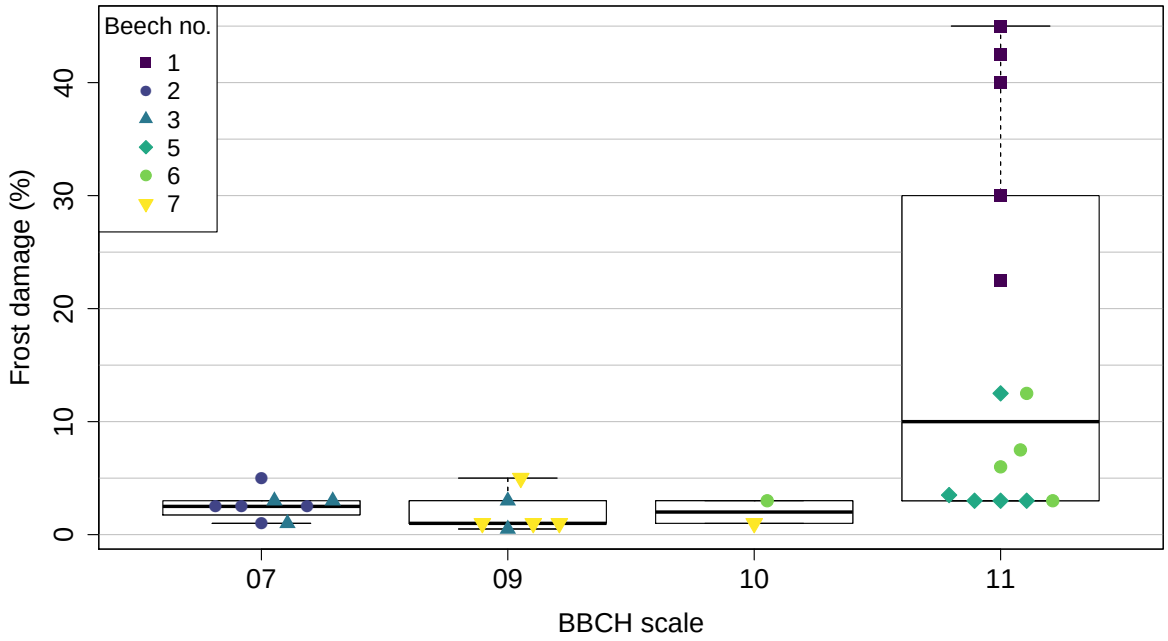

Figure 3.20.: Frost damage of beech leaves in July in relation to bud phenology on 15.05.2019, the last day of frost. The Biologische Bundesanstalt, Bundessortenamt und Chemische Indsturie (BBCH) scales represent the following phenological stages: BBCH code 00–03: winter dormancy, beginning of bud swelling, end of bud swelling, BBCH code 07: beginning of bud breaking, BBCH code 09: buds show green tips, BBCH code 10: first leaves spread apart, BBCH code 11: first leaves unfolded. Beeches number 1 to 3 were located at the summit of Schneeberg near the block field, trees number 5 to 7 were located on the northern slope of Schneeberg in a beech plantation.

Hofmann and Bruelheide (2015) found the T_{air} at which 50 % of the maximum frost damage was reached to be −10.2 °C for freshly opened beech buds, while Vitasse et al. (2014) state the same effect to be reached at −6.8 °C. The difference might be caused by Vitasse et al. (2014) studying buds in BBCH category 10–11, whereas Hofmann and Bruelheide (2015) analyzed buds in BBCH category 9–10. This difference in critical T_{air} in combination with leaf development fits the findings of this thesis which show that the more unfolded leaves are, the more damage they sustain at the same T_{air}. However, other factors between the studies also differed: Hofmann and Bruelheide (2015) selected samples near Halle (Saale), Germany, at ∼90 m a.s.l. and applied freezing temperatures for 45 min, while Vitasse et al. (2014) sampled trees in Switzerland at 570–580 m a.s.l. and froze them for 4 h. Till (1956), on the other hand, states 50 % of the leaf tissue of beeches he sampled near Göttingen, Germany, at altitudes of 240–360 m a.s.l. to already be damaged at T_{air} of only −3.0 °C for a time period of 2 h. The amount of damage

sustained by the leaf tissue thus depends not only on the minimum T_{air} the tissue is exposed to, but is also affected by other factors such as duration of the frost event and seed origin, as individuals from different provenances might have adapted to their climate of origin (Kramer, 1994). While the beech trees in the plantation at Schneeberg were planted, the beeches at the summit most likely germinated in place and their seed origin is unknown. Furthermore, microclimatic factors like air moisture, wind exposure, $I \downarrow$ and canopy cover have not been taken into consideration in the laboratory experiments of Hofmann and Bruelheide (2015), Till (1956) and Vitasse et al. (2014). The complex interplay of all of these variables impedes a definite answer as to why the beeches studies in this thesis showed varying amounts of frost damage.
Additionally to the frost damage, the beeches at the plantation were infested with woolly beech aphids (*Phyllaphis fagi* L.), a common insect in beech nurseries and natural regeneration areas (Gora et al., 1994). *Ph. fagi* feeds on phloem sap, leading to leaf discoloration, desiccation and downwards curling as well as necroses and premature leaf loss (Gora et al., 1994; Iversen and Harding, 2007a,b; Kot and Kmieć, 2012). Possibly, some of the leaf damage attributed to late frost in beeches number 5 to 7 at the plantation actually stems from the aphid infection.
The beeches at Buchberg had already fully unfolded their leaves when measurements started. Despite T_{air} dropping to $-0.7\,°C$ during the night of 04.-05.05.2019, no apparent frost damage was visible at the beeches at Buchberg. Since older leaves are more frost-resistant than newly sprouted leaves (Menzel et al., 2015) and T_{air} was still well above the mildest critical frost threshold found to damage beech leaves in other studies (Till, 1956), this mild frost event probably had no impact on the leaf tissue.

3.7. Synthesis

According to hypothesis I a), the T_{air} differences between measuring locations at Schneeberg site should have been larger than the differences between sites during night, which was clearly not the case as seen in chapter 3.2.1. Only the T_{air} differences between the Schneeberg summit area and the Schneeberg beech plantation $\sim$200 m of elevation lower were within the range of T_{air} differences between measuring locations within the summit area.
Hypothesis I b) was that T_{air} at the Schneeberg summit, at least in some locations, is not lower than at the coldest locations at beech-covered reference sites. While T_{air} at Buchberg and Rauher Kulm was always higher than at the complete Schneeberg summit area during the relevant time intervals with freezing temperatures, T_{air} in the beech plantation at Schneeberg was lower than at the warmest parts of the summit area, supporting this hypothesis (see chapter 3.2.1).
Hypothesis II a) was that the block field cools down further than forested areas during the night, which was refuted by the T_{air} data (see chapter 3.4). Apparently, the amount of energy stored by the blocks during the day, especially due to the size of the blocks and the position on the southern slope, lead to high nighttime T_{air} despite the net longwave radiation loss due to the missing canopy cover.
Hypothesis II b) was the establishment of an inverse T_{air} gradient across the block field at night, which was disproven both for Schneeberg and during time intervals with wind speeds

$>2.0\,\mathrm{m\,s^{-1}}$ also for Rauher Kulm (see chapter 3.2.2 and 3.4). The atmospheric processes of cold-air drainage, ascending warm air, and cold-air pooling downslope typical for block fields could not be found at the two block fields investigated in this thesis. A thin snow cover was present on the first of the measuring days, but too interrupted to facilitate a chimney effect as described by Wakonigg (1996). Neither was there strong enough wind to blow the snow from the boulder surfaces and lead to a thermal bridge (Davesne et al., 2017). Since no measurements inside the voids between the blocks were taken, no definite statements about the possible development of a Balch effect (Balch, 1900, chap. II) with cold-air pooling beneath the blocks versus a rapid adjustment of the void T_{air} to T_{air} above the boulders as found by Harris and Pedersen (1998) can be made. However, the T_{air} and $T_{surface}$ data suggest that it was warmer between the blocks than in the surrounding near-surface air. These unexpected findings mismatching previous studies of block field micrometeorology might be due to the shape and the small size of the block fields investigated in this thesis. With 0.5 ha at Schneeberg and 3 ha but a slope length of only 40 m at Rauher Kulm, both block fields were likely too small for the atmospheric processes typical for block fields to develop. Additionally, the blocks at Schneeberg were much larger than the ones in the study sites of Harris and Pedersen (1998), where they had a diameter of only ∼25 cm, and of Růžička et al. (2012), Růžička et al. (2015) and Zacharda et al. (2007), which had a diameter of 40–80 cm. These smaller blocks might cool down faster than the ones at Schneeberg due to their larger surface to volume ratio, influencing the T_{air} development at the study site.

The site at Buchberg did not show any kind of interesting T_{air} regimes. It behaved similarly to Rauher Kulm, though nighttime T_{air} at Buchberg was usually 0.5 K to 1.0 K below that of Rauher Kulm despite the similar elevation. This thesis could therefore not identify any limiting factors to beech rejuvenation at Buchberg site.

4. Conclusions

The main question of this thesis was whether microtopographic special sites like block fields influence the micrometeorological conditions of their surroundings in a way that enables the growth of European beech outside of its usual physiological habitat range, which is limited by late frosts at high altitudes. If so, those beech establishments could be a first step to diversifying the tree species composition, leading to a decreased risk for forest management of calamities and wood loss.

Meteorological as well as phenological data were gathered in the Fichtelgebirge mountains in Germany, with most measurements taking place at Schneeberg, the highest elevation in the area, to address these questions.

It was found that the air temperature at the summit of Schneeberg does not differ vastly from the temperature at lower parts of the mountain which are covered in beech forest, even in nights were late frosts occurred. The block field proved to be the warmest part of the summit area, while the air under the canopy was cooler. The locations of four beech trees that had germinated in the summit area by chance were consistently the coldest parts of the site. Thus, the beech trees' presence was not due to a microclimate generated by the block field, with chimney-effect induced warm-air locations above the block field favoring beech growth. It is therefore likely that beech would be able to inhabit the complete summit area except for the block field itself and, on a larger scale, all of Fichtelgebirge mountains, except for sites where other factors than late frost are limiting. Both at the summit and in lower regions of Schneeberg mountain, some of the beech trees had started unfolding their leaves by the time of late frosts, while others had not. Of those in advanced phenological stages, the beech at the summit received more frost damage than beeches at lower elevations, but all of the saplings survived, indicating that sapling mortality due to late frost is not a limiting factor for beech establishment in this mountain range.

Considering the block field did not act as a cold-air drainage site and thus did not have the anticipated effects on the surrounding trees, it would have been interesting to have data from further into the forest to get a broader understanding of local temperature gradients irrespective of the block field. From a micrometeorological point of view, a detailed study of the block field's radiation and energy budgets would be of interest, with measurements not only taking place across the surface of the field, but also into the depths between the blocks. From an ecological point of view, arising questions are whether the beech trees that suffered from frost damage will adapt and build more robust leaves in the following years, and whether frost damage significantly decreases wood increment in these altitudes. Furthermore, the statistical validity of the findings was limited by the small sample size of beech trees, a fact that was due to only four beech individuals having sprouted in this area so far. These questions could not be investigated in this thesis, since they would have gone beyond the temporal and technical

scope, and might therefore be addressed in future studies.
The results of this thesis show that European beech is currently not late-frost limited at the summit of Schneeberg, and therefore most likely neither at other parts of Fichtelgebirge mountains. Thus, it is possible to initiate major changes in the silviculture of higher-elevation forests, increasing the percentage of European beech and decreasing the amount of Norway spruce, leading to more diverse, stress-resistant and climate-change tolerating forests. By the end of the century, our understanding of forestry in mid-range mountains might be vastly different from previous perspectives.

Acknowledgements

I would like to thank everyone who helped in the realization of this thesis:
I am especially thankful to Prof. Dr. Christoph Thomas and Prof. Dr. Anke Jentsch for their time and effort, for collaborating in finding this interesting topic, for being willing to embark on an interdisciplinary journey and for their guidance in site selection, data acquisition, evaluation and interpretation.
Thanks to the groups of Micrometeorology and Disturbance Ecology for their feedback on the data analysis.
Many thanks to Jannis Huss for accompanying the field measurements and for fruitful discussions.
I would like to thank Anna Sauer and Blanca Appelt for their help with conducting the flow visualization experiment and their continuous support.
Thanks to Isabel Spies for an introduction to the measuring equipment and her valuable support during the beginning of this thesis and to Andreas Tschuschke for collaborating on designing and building an actively ventilated radiation shield for the MTH.
Thanks to Johann Schneider and Johannes Olesch for help with preparing and setting up the equipment.
Furthermore, I would like to thank the District Government of Upper Franconia, the administrative district office Neustadt an der Waldnaab and Bayerische Staatsforsten AöR for their permission to conduct the field measurements and the flow visualization experiment in protected areas.
Special thanks to the Naturpark Fichtelgebirge e.V., who sponsored this thesis as part of their funding program for theses studying nature conservation aspects in the Fichtelgebirge mountains.

Bibliography

Ammer, C., Stimm, B., and Mosandl, R.: Ontogenetic variation in the relative influence of light and belowground resources on European beech seedling growth, Tree Physiology, 28, 721–728, 2008.

Ashcroft, M. B. and Gollan, J. R.: Moisture, thermal inertia, and the spatial distributions of near-surface soil and air temperatures: understanding factors that promote microrefugia, Agricultural and Forest Meteorology, 176, 77–89, 2013.

Augspurger, C. K.: Spring 2007 warmth and frost: phenology, damage and refoliation in a temperate deciduous forest, Functional Ecology, 23, 1031–1039, https://doi.org/10.1111/j.1365-2435.2009.01587.x, 2009.

Augspurger, C. K. and Bartlett, E. A.: Differences in leaf phenology between juvenile and adult trees in a temperate deciduous forest, Tree Physiology, 23, 517–525, 2003.

Balch, E. S.: Glacières or Freezing Caverns, Allen, Lane & Scott, Philadelphia, USA, 1900.

Bianchi, E., Bugmann, H., and Bigler, C.: Early emergence increases survival of tree seedlings in Central European temperate forests despite severe late frost, Ecology and evolution, 9, 8238–8252, https://doi.org/10.1002/ece3.5399, 2019.

Boeckli, L., Brenning, A., Gruber, S., and Noetzli, J.: Permafrost distribution in the European Alps: calculation and evaluation of an index map and summary statistics, The Cryosphere, 6, 807–820, https://doi.org/10.5194/tc-6-807-2012, 2012.

Bradshaw, R. and Holmqvist, B. H.: Danish forest development during the last 3000 years reconstructed from regional pollen data, Ecography, 22, 53–62, https://doi.org/10.1111/j.1600-0587.1999.tb00454.x, 1999.

Caffarra, A. and Donnelly, A.: The ecological significance of phenology in four different tree species: effects of light and temperature on bud burst, International journal of biometeorology, 55, 711–721, https://doi.org/10.1007/s00484-010-0386-1, 2011.

Cannell, M. G. R. and Smith, R. I.: Climatic Warming, Spring Budburst and Frost Damage on Trees, The Journal of Applied Ecology, 23, 177–191, https://doi.org/10.2307/2403090, 1986.

Čehulić, I., Sever, K., Katičić Bogdan, I., Jazbec, A., Škvorc, Ž., and Bogdan, S.: Drought Impact on Leaf Phenology and Spring Frost Susceptibility in a Quercus robur L. Provenance Trial, Forests, 10, https://doi.org/10.3390/f10010050, 2019.

Chen, Y., An, J., Wang, X., Sun, Y., Wang, Z., and Duan, J.: Observation of wind shear during evening transition and an estimation of submicron aerosol concentrations in Beijing using a Doppler wind lidar, Journal of Meteorological Research, 31, 350–362, https://doi.org/10.1007/s13351-017-6036-3, 2017.

Cole, R. J.: The Longwave Radiative Environment Around Buildings, Building and Environment, 11, 3–13, 1976.

Davesne, G., Fortier, D., Domine, F., and Gray, J. T.: Wind-driven snow conditions control the occurrence of contemporary marginal mountain permafrost in the Chic-Choc Mountains, south-eastern Canada: a case study from Mont Jacques-Cartier, The Cryosphere, 11, 1351–1370, https://doi.org/10.5194/tc-11-1351-2017, 2017.

Davies-Colley, R. J., Payne, G. W., and van Elswijk, M.: Microclimate gradients across a forest edge, New Zealand Journal of Ecology, 24, 111–121, 2000.

Dierschke, H. and Bohn, U.: Eutraphente Rotbuchenwälder in Europa, Tuexenia, 24, 19–56, 2004.

Dittmar, C., Fricke, W., and Elling, W.: Impact of late frost events on radial growth of common beech (Fagus sylvatica L.) in Southern Germany, European Journal of Forest Research, 125, 249–259, https://doi.org/10.1007/s10342-005-0098-y, 2006.

Dobrowski, S. Z.: A climatic basis for microrefugia: the influence of terrain on climate, Global Change Biology, 17, 1022–1035, https://doi.org/10.1111/j.1365-2486.2010.02263.x, 2011.

Ellenberg, H.: Vegetation Mitteleuropas mit den Alpen: In ökologischer, dynamischer und historischer Sicht, vol. 8104 of *UTB für Wissenschaft Grosse Reihe*, Ulmer, Stuttgart, 5 edn., 1996.

Farahat, E. and Linderholm, H. W.: Growth–climate relationship of European beech at its northern distribution limit, European Journal of Forest Research, 137, 619–629, https://doi.org/10.1007/s10342-018-1129-9, 2018.

Fernando, H. J. S., Verhoef, B., Di Sabatino, S., Leo, L. S., and Park, S.: The Phoenix Evening Transition Flow Experiment (TRANSFLEX), Boundary-Layer Meteorology, 147, 443–468, https://doi.org/10.1007/s10546-012-9795-5, 2013.

Fisichelli, N., Vor, T., and Ammer, C.: Broadleaf seedling responses to warmer temperatures "chilled" by late frost that favors conifers, European Journal of Forest Research, 133, 587–596, https://doi.org/10.1007/s10342-014-0786-6, 2014.

Foken, T.: Micrometeorology, Springer-Verlag GmbH, Berlin, Heidelberg, 2 edn., https://doi.org/10.1007/978-3-642-25440-6, 2017.

Freundorfer, A., Rehberg, I., Law, B. E., and Thomas, C.: Forest wind regimes and their implications on cross-canopy coupling, Agricultural and Forest Meteorology, 279, 107 696, https://doi.org/10.1016/j.agrformet.2019.107696, 2019.

Fu, Y. H., Piao, S., Zhou, X., Geng, X., Hao, F., Vitasse, Y., and Janssens, I. A.: Short photoperiod reduces the temperature sensitivity of leaf-out in saplings of Fagus sylvatica but not in horse chestnut, Global Change Biology, 25, 1696–1703, https://doi.org/10.1111/gcb.14599, 2019.

Gora, V., König, J., and Lunderstädt, J.: Physiological defence reactions of young beech trees (Fagus sylvatica) to attack by Phyllaphis fagi, Forest Ecology and Management, 70, 245–254, 1994.

Gude, M. and Barsch, D.: Assessment of geomorphic hazards in connection with permafrost occurrence in the Zugspitze area (Bavarian Alps, Germany), Geomorphology, 66, 85–93, https://doi.org/10.1016/j.geomorph.2004.03.013, 2005.

Guo, L., Wang, J., Li, M., Liu, L., Xu, J., Cheng, J., Gang, C., Yu, Q., Chen, J., Peng, C., and Luedeling, E.: Distribution margins as natural laboratories to infer species' flowering responses to climate warming and implications for frost risk, Agricultural and Forest Meteorology, 268, 299–307, https://doi.org/10.1016/j.agrformet.2019.01.038, 2019.

Hack, H., Bleiholder, H., Buhr, L., Meier, U., Schnock-Fricke, U., Weber, E., and Witzenberger, A.: Einheitliche Codierung der phänologischen Entwicklungsstadien mono- und dikotyler Pflanzen. -Erweiterte BBCH-Skala, Allgemein-, Nachrichtenbl. Deut. Pflanzenschutzd., 44, 265–270, 1992.

Hänninen, H.: Does climatic warming increase the risk of frost damage in northern trees?, Plant, Cell and Environment, 14, 449–454, https://doi.org/10.1111/j.1365-3040.1991.tb01514.x, 1991.

Harris, S. A. and Pedersen, D. E.: Thermal regimes beneath coarse blocky materials, Permafrost and Periglacial Processes, 9, 107–120, https://doi.org/10.1002/(SICI)1099-1530(199804/06)9:2{\textless}107::AID-PPP277{\textgreater}3.0.CO;2-G, 1998.

Heide, O. M.: Dormancy release in beech buds (Fagus sylvatica) requires both chilling and long days, Physiologia Plantarum, 89, 187–191, 1993.

Hertel, M.: Auerhühner Tetrao urogallus im Fichtelgebirge: Anmerkungen eines Försters, Ornithologischer Anzeiger, 48, 13–18, 2009.

Hofmann, M. and Bruelheide, H.: Frost hardiness of tree species is independent of phenology and macroclimatic niche, Journal of Biosciences, 40, 147–157, https://doi.org/10.1007/s12038-015-9505-9, 2015.

Hofmeister, H.: Lebensraum Wald: Pflanzengesellschaften und ihre Ökologie, Kessel, Remagen-Oberwinter, Germany, 4 edn., 2004.

Holden, S.: Dynamics of the wind boundary layer profile and surface parameters at the Schneeberg summit in the Fichtelgebirge Mountains, Bachelor thesis, University of Bayreuth, Bayreuth, 2016.

Howell, J. F. and Mahrt, L.: Multiresolution Flux Decomposition, Boundary-Layer Meteorology, 83, 117–137, 1997.

IPCC: Climate change 2013: The physical science basis. Working Group I contribution to the Fifth assessment report of the Intergovernmental Panel on Climate Change [Stocker, T.F; Qin, D.; Plattner, G.-K; Tignor, M.; Allen, S. K.; Boschung, J.; Nauels, A.; Xia, Y.; Bex, V.; Midgley, P. M. (eds.)], 2013.

Irmak, M. A., Yilmaz, S., and Dursun, D.: Effect of different pavements on human thermal comfort conditions, Atmósfera, 30, 355–366, https://doi.org/10.20937/ATM.2017.30.04.06, 2017.

Iversen, T. and Harding, S.: Biological and other alternative control methods against the woolly beech aphid Phyllaphis fagi L. on beech Fagus sylvatica seedlings in forest nurseries, Journal of Pest Science, 80, 159–166, https://doi.org/10.1007/s10340-007-0168-7, 2007a.

Iversen, T. and Harding, S.: Life table parameters affecting the population development of the woolly beech aphid, Phyllaphis fagi, Entomologia Experimentalis et Applicata, 123, 109–117, https://doi.org/10.1111/j.1570-7458.2007.00524.x, 2007b.

Jones, H. G. and Rotenberg, E.: Energy, Radiation and Temperature Regulation in Plants, in: Encyclopedia of Life Sciences, edited by eLS, John Wiley & Sons, Ltd., New York, https://doi.org/10.1038/npg.els.0003199, 2001.

Jordan, D. N. and Smith, W. K.: Microclimate factors influencing the frequency and duration of growth season frost for subalpine plants, Agricultural and Forest Meteorology, 77, 17–30, 1995.

Kadereit, J. W., Körner, C., Kost, B., and Sonnewald, U.: Strasburger – Lehrbuch der Pflanzenwissenschaften, Springer Spektrum, Berlin, Heidelberg, 37 edn., https://doi.org/10.1007/978-3-642-54435-4, 2014.

Kodra, E., Steinhaeuser, K., and Ganguly, A. R.: Persisting cold extremes under 21st-century warming scenarios, Geophysical Research Letters, 38, https://doi.org/10.1029/2011GL047103, 2011.

Kollas, C., Körner, C., and Randin, C. F.: Spring frost and growing season length co-control the cold range limits of broad-leaved trees, Journal of Biogeography, 41, 773–783, https://doi.org/10.1111/jbi.12238, 2014.

Kölling, C., Zimmermann, L., and Walentowski, H.: Klimawandel: Was geschieht mit Buche und Fichte? Entscheidungshilfen für den klimagerechten Waldumbau in Bayern, AFZ-DerWald, 62, 584–588, 2007.

Kolmogorov, A. N.: Lokalnaja struktura turbulentnosti v neschtschimaemoi schidkosti pri otschen bolschich tschislach Reynoldsa (The local structure of turbulence in incompressible viscous fluid for very large Reynolds numbers), Dokl AN SSSR, 30, 299–303, 1941a.

Kolmogorov, A. N.: Rassejanie energii pri lokolno-isotropoi turbulentnosti (Dissipation of energy in locally isotropic turbulence), Dokl AN SSSR, 32, 22–24, 1941b.

Kot, I. and Kmieć, K.: Study on Intensity of Infestation, Biology and Harmfulness of Wolly Beech aphid (Phyllaphis fagi L.) on Fagus sylvatica (L.), Acta Scientiarum Polonorum-Hortorum Cultus, 11, 3–11, 2012.

Kotzé, C. and Meiklejohn, I.: Temporal variability of ground thermal regimes on the northern buttress of the Vesleskarvet nunatak, western Dronning Maud Land, Antarctica, Antarctic Science, 29, 73–81, https://doi.org/10.1017/S095410201600047X, 2017.

Kramer, K.: A modelling analysis of the effects of climatic warming on the probability of spring frost damage to tree species in The Netherlands and Germany, Plant, Cell and Environment, 17, 367–377, https://doi.org/10.1111/j.1365-3040.1994.tb00305.x, 1994.

Kreyling, J., Buhk, C., Backhaus, S., Hallinger, M., Huber, G., Huber, L., Jentsch, A., Konnert, M., Thiel, D., Wilmking, M., and Beierkuhnlein, C.: Local adaptations to frost in marginal and central populations of the dominant forest tree Fagus sylvatica L. as affected by temperature and extreme drought in common garden experiments, Ecology and evolution, 4, 594–605, https://doi.org/10.1002/ece3.971, 2014.

Leinonen, I.: A Simulation Model for the Annual Frost Hardiness and Freeze Damage of Scots Pine, Annals of Botany, 78, 687–693, 1996.

Lenz, A., Hoch, G., Körner, C., and Vitasse, Y.: Convergence of leaf-out towards minimum risk of freezing damage in temperate trees, Functional Ecology, 30, 1480–1490, https://doi.org/10.1111/1365-2435.12623, 2016.

Liepe, K.: Growth-chamber trial on frost hardiness and field trial on flushing of sessile oak (Quercus petraea Liebl), Annales des sciences forestières, 50 (Suppl 1), 208s–214s, 1993.

Loos, E.: Dynamics of the temperature and wind profiles in the boundary layer of a valley in the Fichtelgebirge Mountains, Bachelor thesis, University of Bayreuth, Bayreuth, 2016.

Lund, U. and Agostinelli, C.: CircStats: Circular Statistics: R package version 0.2-6, URL `https://cran.r-project.org/web/packages/CircStats/CircStats.pdf`, 2018.

Marchand, L. J., Dox, I., Gričar, J., Prislan, P., Leys, S., van den Bulcke, J., Fonti, P., Lange, H., Matthysen, E., Peñuelas, J., Zuccarini, P., and Campioli, M.: Inter-individual variability in spring phenology of temperate deciduous trees depends on species, tree size and previous year autumn phenology, Agricultural and Forest Meteorology, 290, 108 031, https://doi.org/10.1016/j.agrformet.2020.108031, 2020.

Marini, L., Ayres, M. P., Battisti, A., and Faccoli, M.: Climate affects severity and altitudinal distribution of outbreaks in an eruptive bark beetle, Climatic Change, 115, 327–341, https://doi.org/10.1007/s10584-012-0463-z, 2012.

McGreevy, J. P.: Thermal properties as controls on rock surface temperature maxima, and possible implications for rock weathering, Earth Surface Processes and Landforms, 10, 125–136, 1985.

Menzel, A., Helm, R., and Zang, C.: Patterns of late spring frost leaf damage and recovery in a European beech (Fagus sylvatica L.) stand in south-eastern Germany based on repeated digital photographs, Frontiers in plant science, 6, https://doi.org/10.3389/fpls.2015.00110, 2015.

Mezei, P., Jakuš, R., Pennerstorfer, J., Havašová, M., Škvarenina, J., Ferenčík, J., Slivinský, J., Bičárová, S., Bilčík, D., Blaženec, M., and Netherer, S.: Storms, temperature maxima and the Eurasian spruce bark beetle Ips typographus—An infernal trio in Norway spruce forests of the Central European High Tatra Mountains, Agricultural and Forest Meteorology, 242, 85–95, https://doi.org/10.1016/j.agrformet.2017.04.004, 2017.

Moning, C. and Müller, J.: Critical forest age thresholds for the diversity of lichens, molluscs and birds in beech (Fagus sylvatica L.) dominated forests, Ecological Indicators, 9, 922–932, https://doi.org/10.1016/j.ecolind.2008.11.002, 2009.

Murray, M. B., Cannell, M. G. R., and Smith, R. I.: Date of Budburst of Fifteen Tree Species in Britain Following Climatic Warming, The Journal of Applied Ecology, 26, 693, https://doi.org/10.2307/2404093, 1989.

Musselman, K. N. and Pomeroy, J. W.: Estimation of Needleleaf Canopy and Trunk Temperatures and Longwave Contribution to Melting Snow, Journal of Hydrometeorology, 18, 555–572, https://doi.org/10.1175/JHM-D-16-0111.1, 2017.

Negi, A. S., Negi, G. C. S., and Singh, S. P.: Establishment and growth of Quercus floribunda seedlings after a mast year, Journal of Vegetation Science, 7, 559–564, 1996.

Ningre, F. and Colin, F.: Frost damage on the terminal shoot as a risk factor of fork incidence on common beech (Fagus sylvatica L.), Annals of Forest Science, 64, 79–86, https://doi.org/10.1051/forest:2006091, 2007.

Noilhan, J. and Mahfouf, J.-F.: The ISBA land surface parameterisation scheme, Global and Planetary Change, 13, 145–159, 1996.

Nolè, A., Rita, A., Ferrara, A. M. S., and Borghetti, M.: Effects of a large-scale late spring frost on a beech (Fagus sylvatica L.) dominated Mediterranean mountain forest derived from the spatio-temporal variations of NDVI, Annals of Forest Science, 75, https://doi.org/10.1007/s13595-018-0763-1, 2018.

Oesterle, N.: Untersuchungen zum Waldwachstum, Altersaufbau und Radialzuwachs im FFH – Gebiet Buchberg (Fichtelgebirge/Oberfranken), Bachelor thesis, Weihenstephan-Triesdorf University of Applied Sciences, Freising, 2015.

Petritan, A. M., von Lüpke, B., and Petritan, I. C.: Effects of shade on growth and mortality of maple (Acer pseudoplatanus), ash (Fraxinus excelsior) and beech (Fagus sylvatica) saplings, Forestry, 80, 397–412, https://doi.org/10.1093/forestry/cpm030, 2007.

Popescu, R., Vespremeanu-Stroe, A., Onaca, A., Vasile, M., Cruceru, N., and Pop, O.: Low-altitude permafrost research in an overcooled talus slope–rock glacier system in the Romanian Carpathians (Detunata Goală, Apuseni Mountains), Geomorphology, 295, 840–854, https://doi.org/10.1016/j.geomorph.2017.07.029, 2017.

Portillo-Quintero, C., Sánchez-Azofeifa, A., and Marcos do Espírito-Santo, M.: Edge Influence on Canopy Openness and Understory Microclimate in Two Neotropical Dry Forest Fragments, in: Tropical Dry Forests in the Americas, edited by Sanchez-Azofeifa, A., Powers, J. S., Fernandes, G. W., and Quesada, M., pp. 157–172, CRC Press Taylor & Francis Group, Boca Raton, https://doi.org/10.1201/b15417-11, 2013.

Príncipe, A., van der Maaten, E., van der Maaten-Theunissen, M., Struwe, T., Wilmking, M., and Kreyling, J.: Low resistance but high resilience in growth of a major deciduous forest tree (Fagus sylvatica L.) in response to late spring frost in southern Germany, Trees, 31, 743–751, https://doi.org/10.1007/s00468-016-1505-3, 2017.

Reiter, B.: Einfluss des Wildes auf die Keimlingsetablierung von Fagus sylvatica in einem FFH-Buchenwald am Buchberg, Bachelor thesis, University of Bayreuth, Bayreuth, 2012.

Roedel, W. and Wagner, T.: Physik unserer Umwelt: Die Atmosphäre, Springer Spektrum, Berlin, Heidelberg, 5 edn., https://doi.org/10.1007/978-3-662-54258-3, 2017.

Růžička, V., Zacharda, M., Němcová, L., Šmilauer, P., and Nekola, J. C.: Periglacial microclimate in low-altitude scree slopes supports relict biodiversity, Journal of Natural History, 46, 2145–2157, https://doi.org/10.1080/00222933.2012.707248, 2012.

Růžička, V., Zacharda, M., Šmilauer, P., and Kučera, T.: Can paleorefugia of cold-adapted species in talus slopes resist global warming?, Boreal Environment Research, 20, 403–412, 2015.

Schmidt, P.: Studie zur Verjüngung der Buche im FFH-Gebiet Buchberg im Fichtelgebirge – Entwicklung von Buchenkeimlingen in unterschiedlichen Bodensubstraten, Bachelor thesis, Weihenstephan-Triesdorf University of Applied Sciences, Freising, 2018.

Serafimovich, A., Hübner, J., Leclerc, M. Y., Duarte, H. F., and Foken, T.: Influence of Low-Level Jets and Gravity Waves on Turbulent Fluxes, in: Energy and matter fluxes of a spruce forest ecosystem, edited by Foken, T., Ecological studies, pp. 247–276, Springer, Cham, https://doi.org/10.1007/978-3-319-49389-3{\textunderscore}11, 2017.

Spiecker, H., Hansen, J., Klimo, E., Skovsgaard, J. P., Sterba, H., and von Teuffel, K., eds.: Norway spruce conversion - options and consequences, vol. 18 of *European Forest Institute research report*, European Forest Institute, Brill, Leiden, 2004.

Spies, I.: Urban climate – just warm streets and cool parks? Investigating the variabilities of heat at street-canyon and city-wide scale in Bayreuth, Master thesis, University of Bayreuth, Bayreuth, 2019.

Stiegler, C., Rode, M., Sass, O., and Otto, J.-C.: An Undercooled Scree Slope Detected by Geophysical Investigations in Sporadic Permafrost below 1000 M ASL, Central Austria, Permafrost and Periglacial Processes, 25, 194–207, https://doi.org/10.1002/ppp.1813, 2014.

Strunz, H.: Die Basalte der Oberpfalz und ihre Mineralien, in: Zur Mineralogie und Geologie der Oberpfalz, edited by Strunz, H., vol. Der Aufschluss, Sonderband 26 of *Der Aufschluss*, pp. 329–342, Vereinigung der Freunde der Mineralogie und Geologie e.V., Heidelberg, 1975.

Stull, R. B.: Practical meteorology: An algebra-based survey of atomspheric science, University of British Columbia, Vancouver, v1.02b edn., URL `https://www.eoas.ubc.ca/books/Practical_Meteorology`, 2017.

Thieurmel, B. and Elmarhraoui, A.: suncalc: Compute Sun Position, Sunlight Phases, Moon Position and Lunar Phase: R package version 0.5.0, URL `https://github.com/datastorm-open/suncalc`, 2019.

Thomas, C. K.: Variability of Sub-Canopy Flow, Temperature, and Horizontal Advection in Moderately Complex Terrain, Boundary-Layer Meteorology, 139, 61–81, https://doi.org/10.1007/s10546-010-9578-9, 2011.

Thomas, C. K. and Smoot, A. R.: An Effective, Economic, Aspirated Radiation Shield for Air Temperature Observations and Its Spatial Gradients, Journal of Atmospheric and Oceanic Technology, 30, 526–537, https://doi.org/10.1175/JTECH-D-12-00044.1, 2013.

Till, O.: Über die Frosthärte von Pflanzen sommergrüner Laubwälder, Flora – Allgemeine Botanische Zeitung, 143, 499–542, https://doi.org/10.1016/S0367-1615(17)33134-8, 1956.

Urban, J., Bednárová, E., Plichta, R., Gryc, V., Vavrčík, H., Hacura, J., Fajstavr, M., and Kučera, J.: Links between phenology and ecophysiology in a European beech forest, iForest - Biogeosciences and Forestry, 8, 438–447, https://doi.org/10.3832/ifor1307-007, 2015.

Vander Mijnsbrugge, K., Turcsán, A., Maes, J., Duchêne, N., Meeus, S., Steppe, K., and Steenackers, M.: Repeated Summer Drought and Re-watering during the First Growing Year of Oak (Quercus petraea) Delay Autumn Senescence and Bud Burst in the Following Spring, Frontiers in plant science, 7, https://doi.org/10.3389/fpls.2016.00419, 2016.

Vickers, D. and Thomas, C. K.: Some aspects of the turbulence kinetic energy and fluxes above and beneath a tall open pine forest canopy, Agricultural and Forest Meteorology, 181, 143–151, https://doi.org/10.1016/j.agrformet.2013.07.014, 2013.

Vickers, D. and Thomas, C. K.: Observations of the scale-dependent turbulence and evaluation of the flux–gradient relationship for sensible heat for a closed Douglas-fir canopy in very weak wind conditions, Atmospheric Chemistry and Physics, 14, 9665–9676, https://doi.org/10.5194/acp-14-9665-2014, 2014.

Vitasse, Y., Lenz, A., Hoch, G., and Körner, C.: Earlier leaf-out rather than difference in freezing resistance puts juvenile trees at greater risk of damage than adult trees, Journal of Ecology, 102, 981–988, https://doi.org/10.1111/1365-2745.12251, 2014.

Vitasse, Y., Schneider, L., Rixen, C., Christen, D., and Rebetez, M.: Increase in the risk of exposure of forest and fruit trees to spring frosts at higher elevations in Switzerland over the last four decades, Agricultural and Forest Meteorology, 248, 60–69, https://doi.org/10.1016/j.agrformet.2017.09.005, 2018.

Vollrath, H.: Die Pflanzenwelt des Fichtelgebirges und benachbarter Landschaften in geobotanischer Schau: Geobotanik des Fichtelgebirges und benachbarter Florenbezirke, vol. 9 of *Berichte der Naturwissenschaftlichen Gesellschaft Bayreuth*, Naturwissenschaftliche Gesellschaft Bayreuth, Bayreuth, 1957.

Vospernik, S. and Nothdurft, A.: Can trees at high elevations compensate for growth reductions at low elevations due to climate warming?, Canadian Journal of Forest Research, 48, 650–662, 2018.

Wakonigg, H.: Unterkühlte Schutthalden, Arbeiten aus dem Institut für Geographie der Karl-Franzens-Universität Graz, 33, 209–223, 1996.

Wurm, A.: Einfluss ökologischer Parameter auf die Keimlingsetablierung von Fagus sylvatica L. in einem autochthonen Buchenwald am Buchberg (Fichtelgebirge), Bachelor thesis, University of Bayreuth, Bayreuth, 2012.

Wüst, J.: Studie zur Verjüngung der Buche im FFH-Gebiet Buchberg im Fichtelgebirge - Saatversuche in Kleinparzellen mit Bodenbearbeitung und Kalkung, Bachelor thesis, Weihenstephan-Triesdorf University of Applied Sciences, Freising, 2018.

Zacharda, M., Gude, M., and Růžička, V.: Thermal regime of three low elevation scree slopes in central Europe, Permafrost and Periglacial Processes, 18, 301–308, https://doi.org/10.1002/ppp.598, 2007.

Zohner, C. M., Rockinger, A., and Renner, S. S.: Increased autumn productivity permits temperate trees to compensate for spring frost damage, The New phytologist, 221, 789–795, https://doi.org/10.1111/nph.15445, 2019.

A. Measuring sites

Figure A.1.: Picture of Schneeberg measuring site with micro sonic anemometer (marked by white arrow) and supporting equipment (17.07.2019).

Figure A.2.: Picture of Schneeberg beech plantation (14.05.2019).

Figure A.3.: Picture of Buchberg measuring site (30.04.2019).

Figure A.4.: Picture of Rauher Kulm measuring site (19.01.2019).

(a) F1, 30.04.2019

(b) F2, 18.04.2019 (Photo: C. Thomas)

(c) F3, 18.04.2019 (Photo: C. Thomas)

(d) F4, 18.04.2019 (Photo: C. Thomas)

(e) F5, 05.05.2019

(f) F6, 30.04.2019

(g) F7, 04.05.2019

(h) F8, 04.05.2019

Figure A.5.: Pictures of all stationary thermohygrometer measuring locations.

(a) T01, 06.07.2019

(b) T02, 06.07.2019

(c) T03, 06.07.2019

(d) T04, 06.07.2019

(e) T05, 06.07.2019

(f) T06, 06.07.2019

(g) T07, 06.07.2019

(h) T08, 06.07.2019

Figure A.6.: Pictures of mobile thermohygrometer measuring locations T01 to T08.

(a) T09, 06.07.2019

(b) T10, 06.07.2019

(c) T11, 06.07.2019

(d) T12, 06.07.2019

(e) T13, 06.07.2019

(f) T14, 06.07.2019

(g) T15, 06.07.2019

(h) T16, B1, 15.05.2019

Figure A.7.: Pictures of mobile thermohygrometer measuring locations T09 to T16 and beech B1.

(a) T17, B2, 15.05.2019

(b) T18, B3, 15.05.2019

(c) T19, B4, 15.05.2019

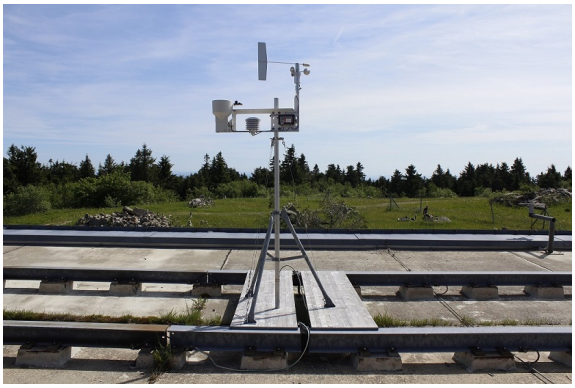

(d) T20, weather station, 09.06.2019

Figure A.8.: Pictures of mobile thermohygrometer measuring locations T17 to T20, beeches B2 to B4 and Schneeberg weather station.

B. Additional figures

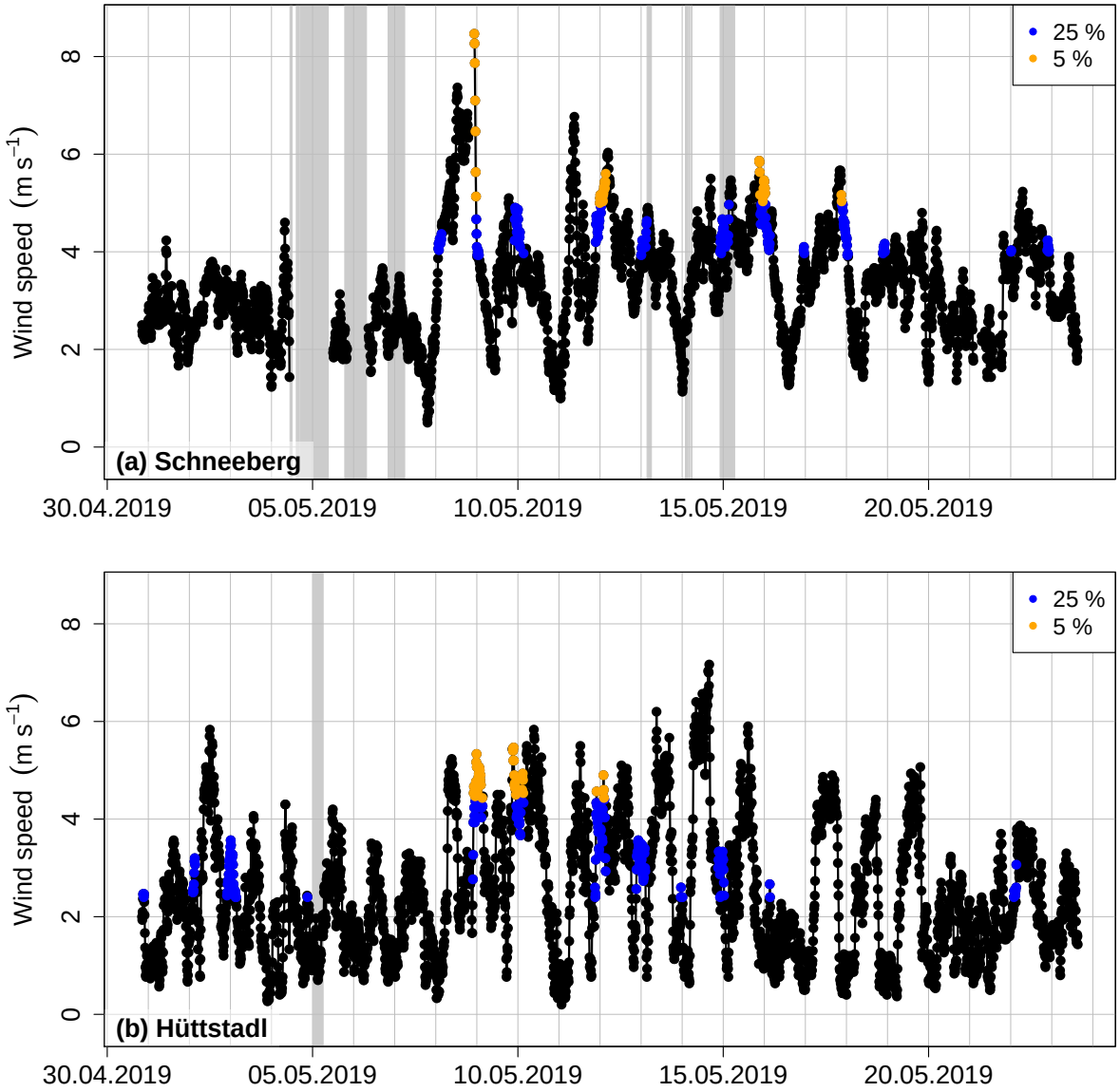

Figure B.1.: Wind speed measured by weather stations with 25 % and 5 % of windiest intervals of nighttime (21:00–03:20) data highlighted. The wind speed was recorded (a) at Schneeberg, with grey bars indicating the times with air temperature T_{air} at Schneeberg (spatial mean of F1 to F5) below 0 °C and (b) at Hüttstadl near Rauher Kulm, with grey bars indicating the times with T_{air} at Rauher Kulm (spatial mean of F7 and F8) below 0 °C.

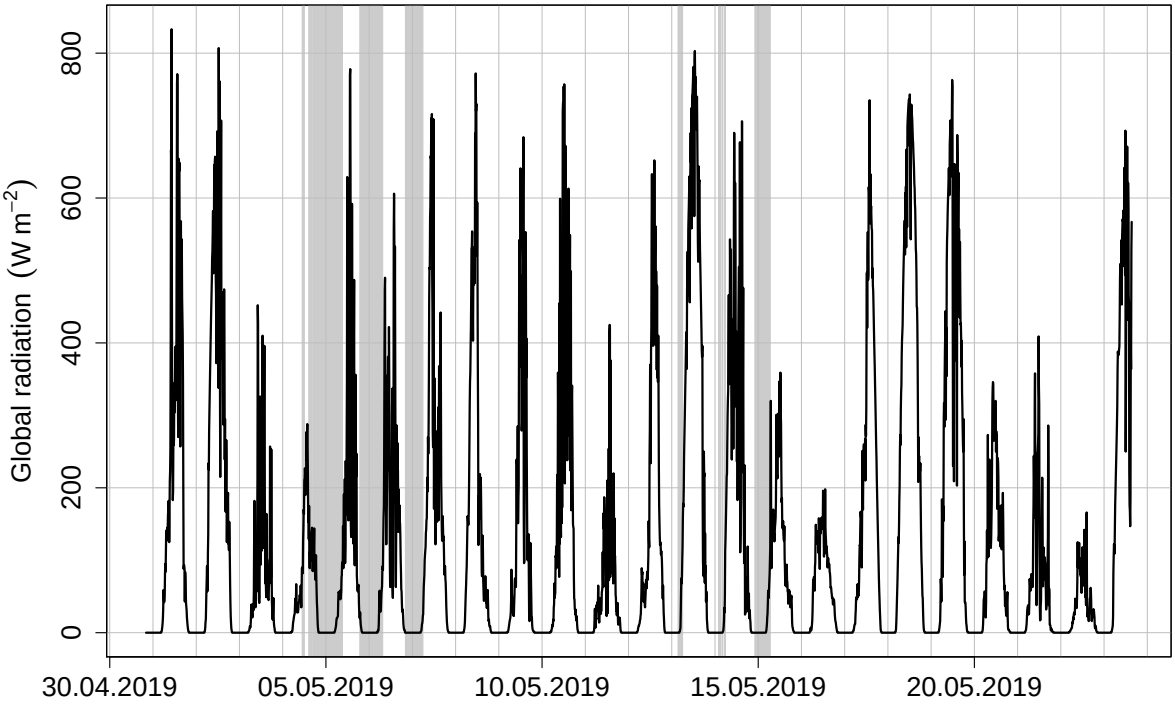

Figure B.2.: Global radiation at Schneeberg weather station during the time of the experiment. Grey bars indicate the times with air temperature at Schneeberg (spatial mean of F1 to F5) below 0 °C.

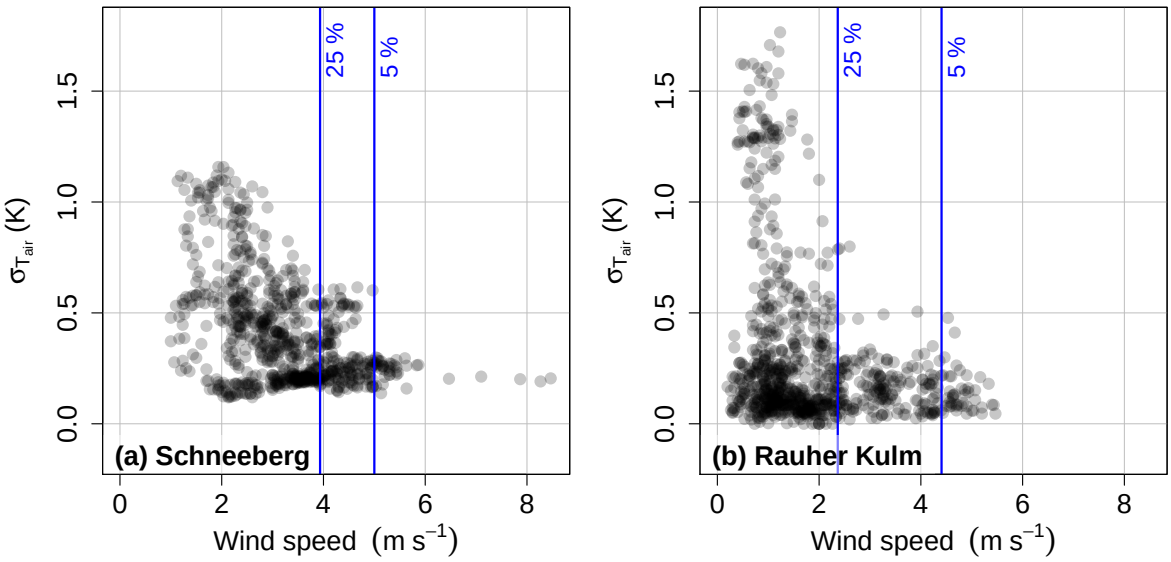

Figure B.3.: Standard deviation σ of (a) F1 to F4 and (b) F7 and F8 half-hourly stationary thermo-hygrometer air temperature T_{air} data per wind speed during nighttime with 25th and 5th percentile.

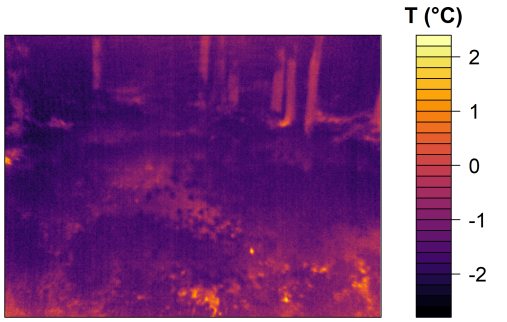

(a) B1, 05.05.2019

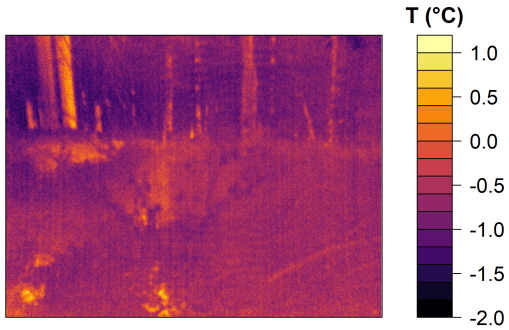

(b) B2, 05.05.2019

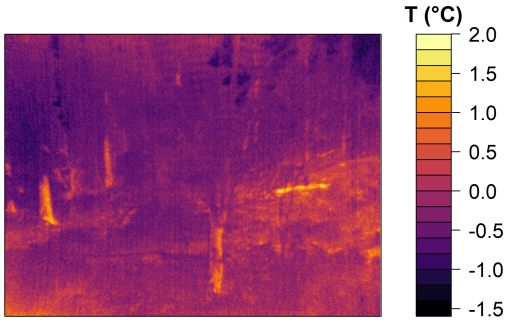

(c) B3, 05.05.2019

Figure B.4.: Surface brightness temperature $T_{surface}$ of beech trees at Schneeberg summit and their surroundings on 05.05.2019, assuming an emissivity of 0.92. White areas indicate temperatures outside of the range of the color bar.

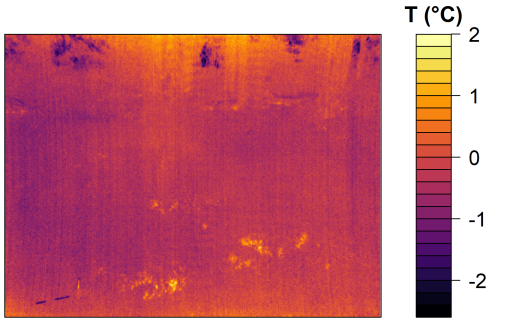

(a) B1, 07.05.2019

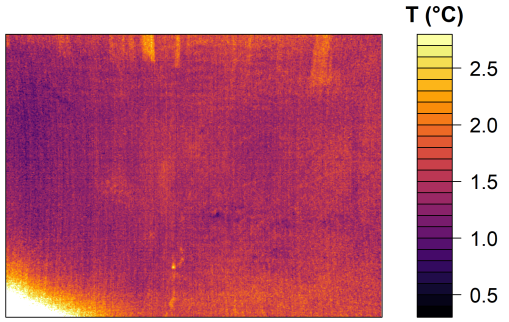

(b) B2, 07.05.2019

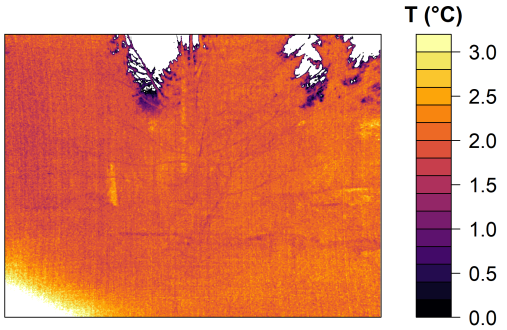

(c) B3, 07.05.2019

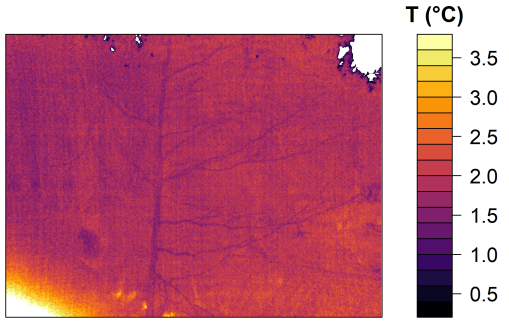

(d) B4, 07.05.2019

Figure B.5.: Surface brightness temperature $T_{surface}$ of beech trees at Schneeberg summit and their surroundings on 07.05.2019, assuming an emissivity of 0.92. White areas indicate temperatures outside of the range of the color bar.

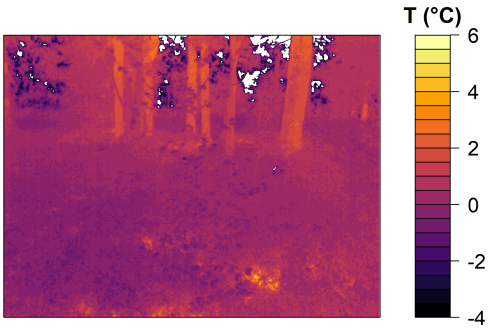

(a) B1, 14.05.2019

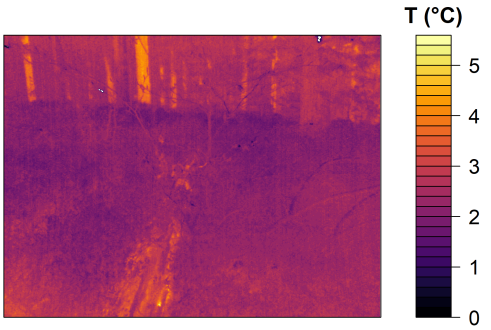

(b) B2, 14.05.2019

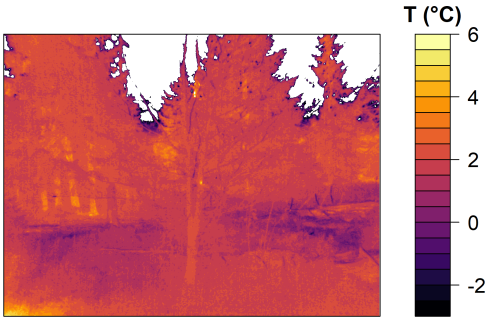

(c) B3, 14.05.2019

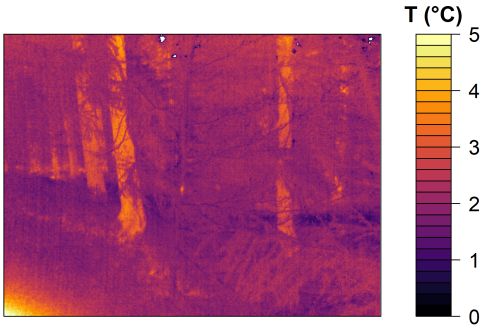

(d) B4, 14.05.2019

Figure B.6.: Surface brightness temperature $T_{surface}$ of beech trees at Schneeberg summit and their surroundings on 14.05.2019, assuming an emissivity of 0.92. White areas indicate temperatures outside of the range of the color bar.

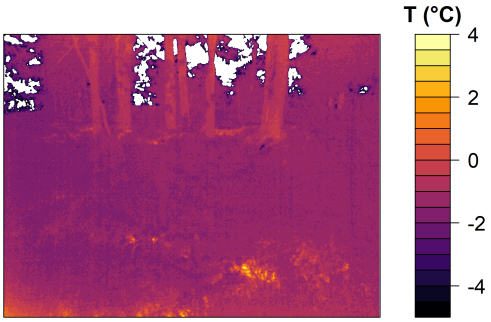

(a) B1, 15.05.2019

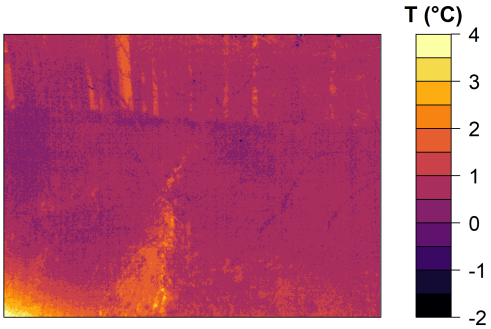

(b) B2, 15.05.2019

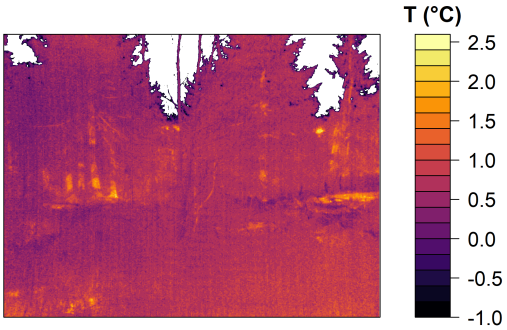

(c) B3, 15.05.2019

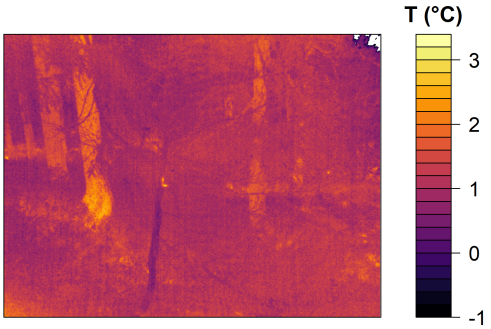

(d) B4, 15.05.2019

Figure B.7.: Surface brightness temperature $T_{surface}$ of beech trees at Schneeberg summit and their surroundings on 15.05.2019, assuming an emissivity of 0.92. White areas indicate temperatures outside of the range of the color bar.

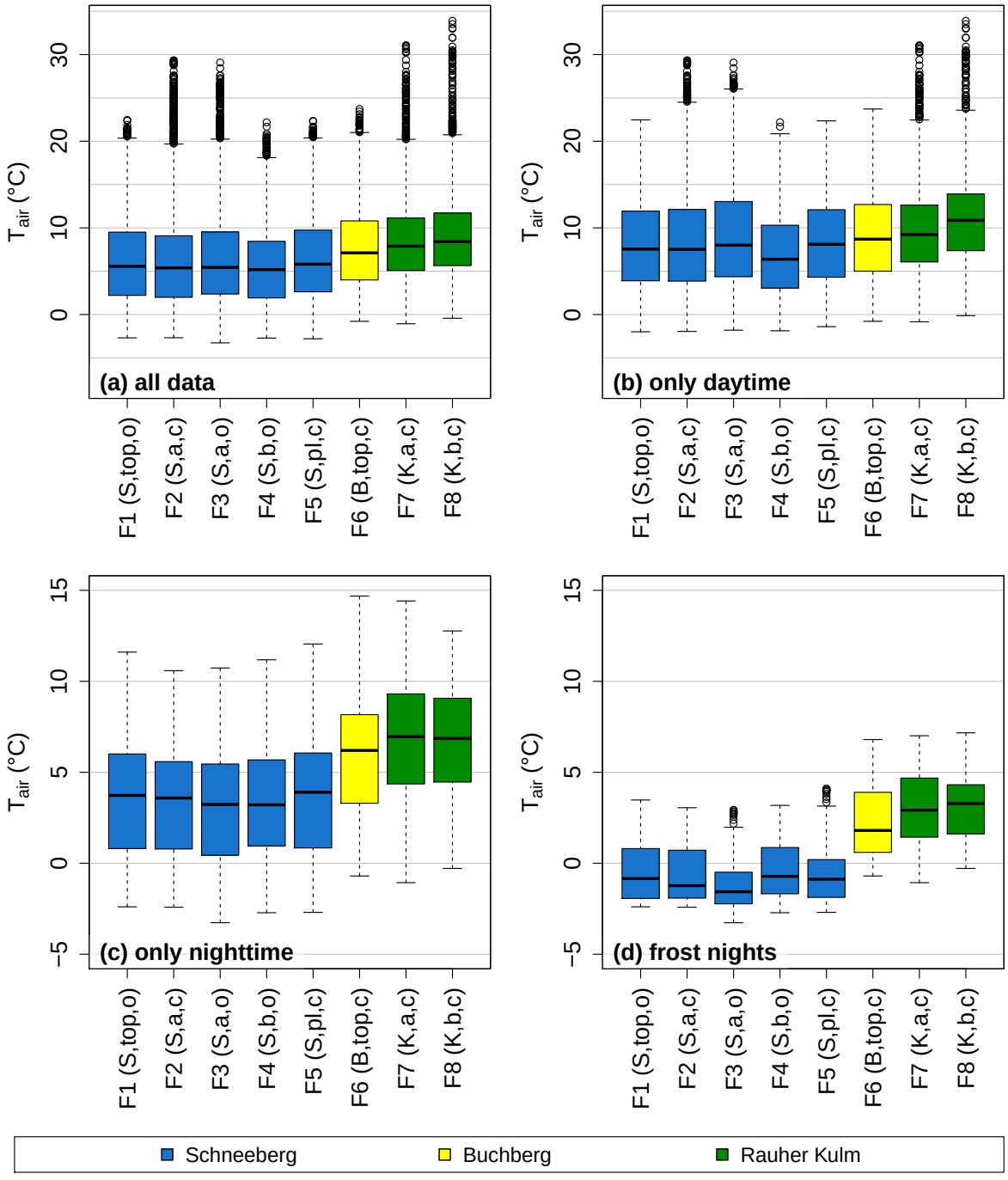

Figure B.8.: Boxplots of air temperature T_{air} per stationary thermohygrometer (STH) and subset: (a) complete data set from 30.04.2019–23.05.2019, (b) only daytime values (05:50–18:30), (c) only nighttime values (21:00–03:20), (d) only frost night values (see Tab. 2.3). Parentheses in axis labels describe the location of each STH: S = Schneeberg, B = Buchberg, K = Rauher Kulm, top = summit, a = above block field, b = below block field, pl = plantation, o = open to the sky, c = under canopy. The bold line marks the median, the box encompasses the 25^{th} to 75^{th} percentile, whiskers encompass the range of all data except for outliers, dots are outliers.

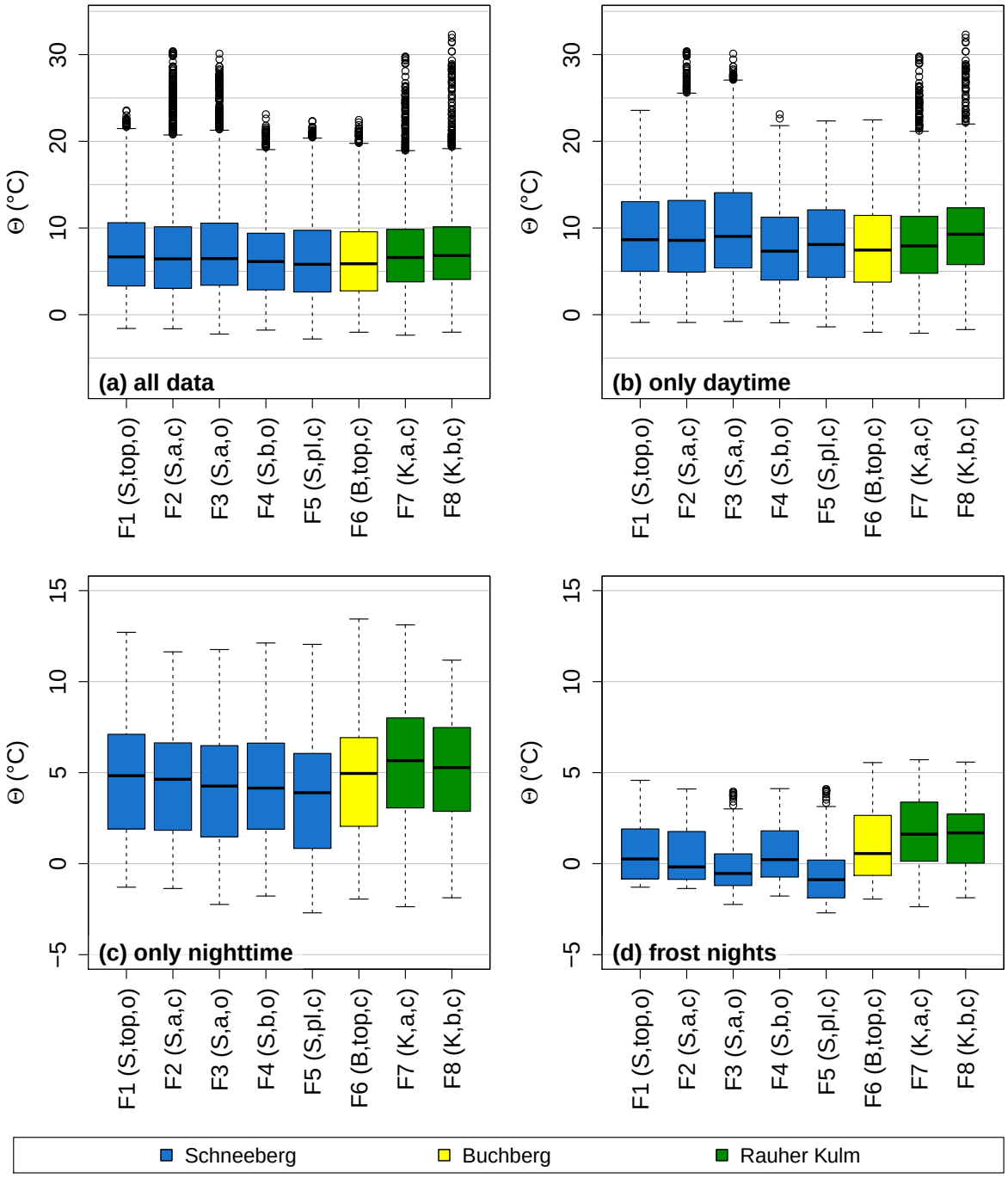

Figure B.9.: Boxplots of potential temperature Θ at a reference elevation of 871 m above sea level per stationary thermohygrometer (STH) and subset: (a) complete data set from 30.04.2019–23.05.2019, (b) only daytime values (05:50–18:30), (c) only nighttime values (21:00–03:20), (d) only frost night values (see Tab. 2.3). Parentheses in axis labels describe the location of each STH: S = Schneeberg, B = Buchberg, K = Rauher Kulm, top = summit, a = above block field, b = below block field, pl = plantation, o = open to the sky, c = under canopy. The bold line marks the median, the box encompasses the 25th to 75th percentile, whiskers encompass the range of all data except for outliers, dots are outliers.

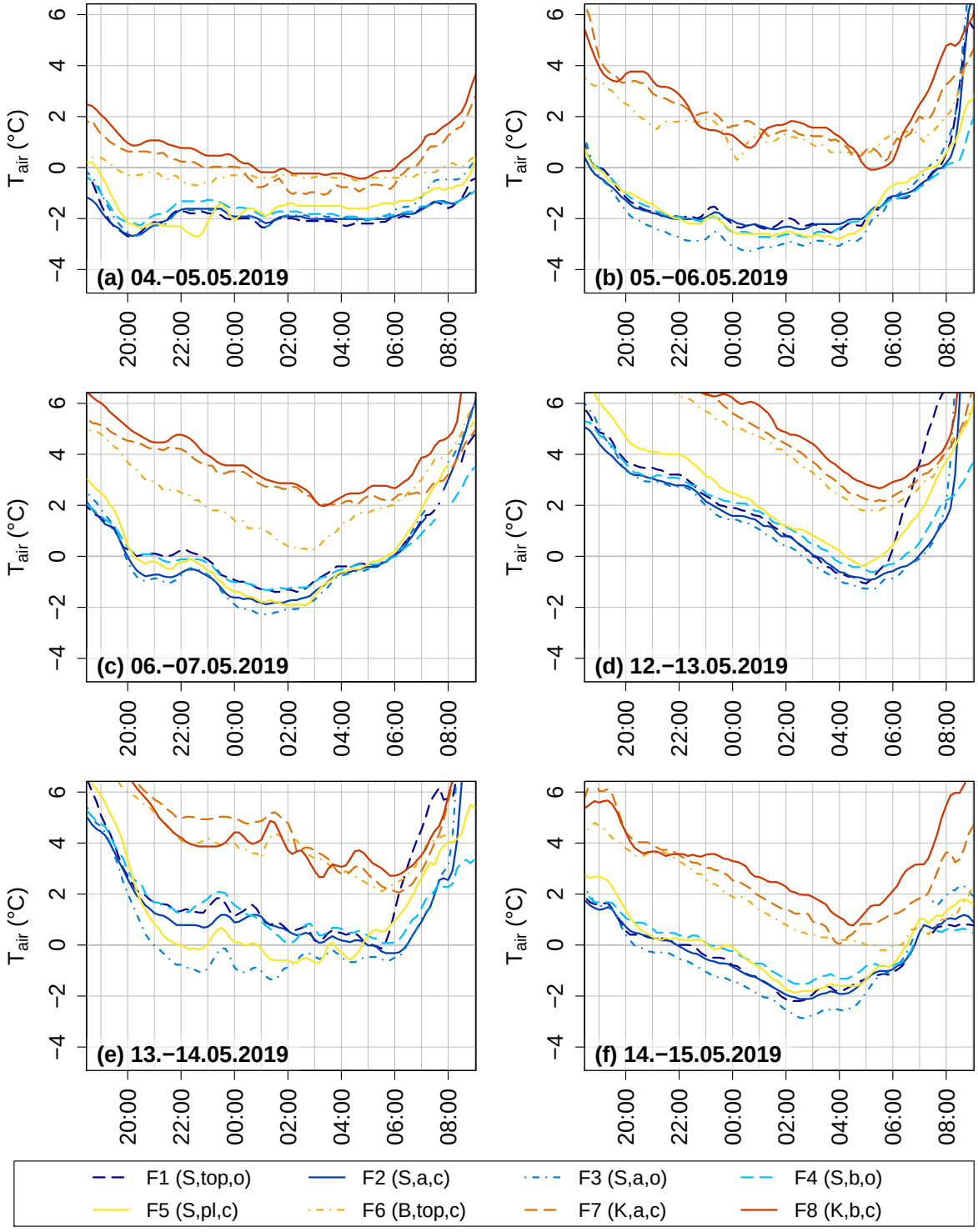

Figure B.10.: Air temperature T_{air} measurements of stationary thermohygrometers (STHs) during the six frost nights. Parentheses in plot legend describe the location of each STH: S = Schneeberg, B = Buchberg, K = Rauher Kulm, top = summit, a = above block field, b = below block field, pl = plantation, o = open to the sky, c = under canopy.

C. Block field surface temperature

$T_{surface}$ of the block field in relation to the forest canopy varied (Fig. C.1). On 05.05.2019 and 14.05.2019, the block field was much warmer than the surrounding forest, whereas on 07.05.2019, $T_{surface}$ was similar to the forest. On 15.05.2019, $T_{surface}$ of the block field was very heterogeneous according to the IR camera, with the skyward pointing edges of the blocks very cold and the spaces in between the blocks very warm. The small anthropogenic block heap directly at the summit of Schneeberg where F1 was located was warmer than the surrounding grass on the first measuring day, of similar $T_{surface}$ on 07.05.2019 and very heterogeneous on the last two measuring days (Fig. C.2).

On the first two measuring days, the IR camera measured sky temperatures higher than $-10.0\,°C$, indicating cloudy conditions, whereas on the last two measuring days, the sky temperature was around $-20.0\,°C$ to $-40.0\,°C$, meaning that the sky was clear. While the sky temperatures in relation to the $T_{surface}$ differences between block field and canopy seem to indicate that under clear-sky conditions like on 15.05.2019, the blocks cool down more strongly than the forest, it is more likely that the low block $T_{surface}$ measured by the IR camera on this day is an artifact of the underlying physics. The reflectivity of longwave radiation is angular dependent (Cole, 1976), therefore the blocks, depending on the angle toward the sky and the IR camera, reflect the sky temperature toward the camera at varying degrees. The effect of the distortion is the larger the colder the sky is, therefore it is largest for the last two measuring days. However, for the shallow angle between the camera and the block field in combination with the crystalline structure of the rock surface, which provides a spectrum of scattering angles, the magnitude of this measurement error should not be very large.

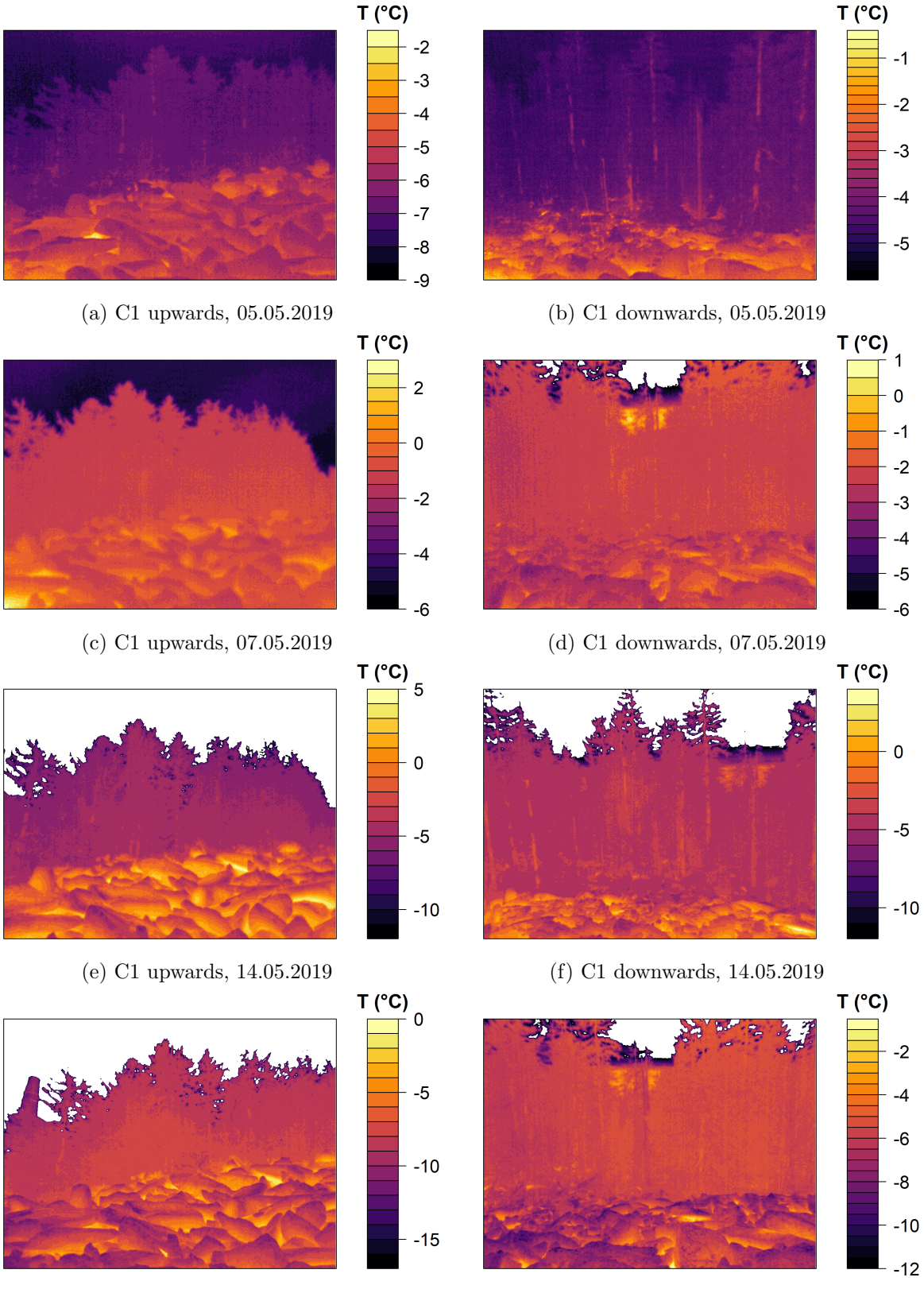

(a) C1 upwards, 05.05.2019

(b) C1 downwards, 05.05.2019

(c) C1 upwards, 07.05.2019

(d) C1 downwards, 07.05.2019

(e) C1 upwards, 14.05.2019

(f) C1 downwards, 14.05.2019

(g) C1 upwards, 15.05.2019

(h) C1 downwards, 15.05.2019

Figure C.1.: Surface brightness temperature $T_{surface}$ of the block field and the forest edge above (left) and below (right) on each measuring day, images taken at infrared camera location C1 using an emissivity of 0.95. White areas indicate temperatures outside of the range of the color bar.

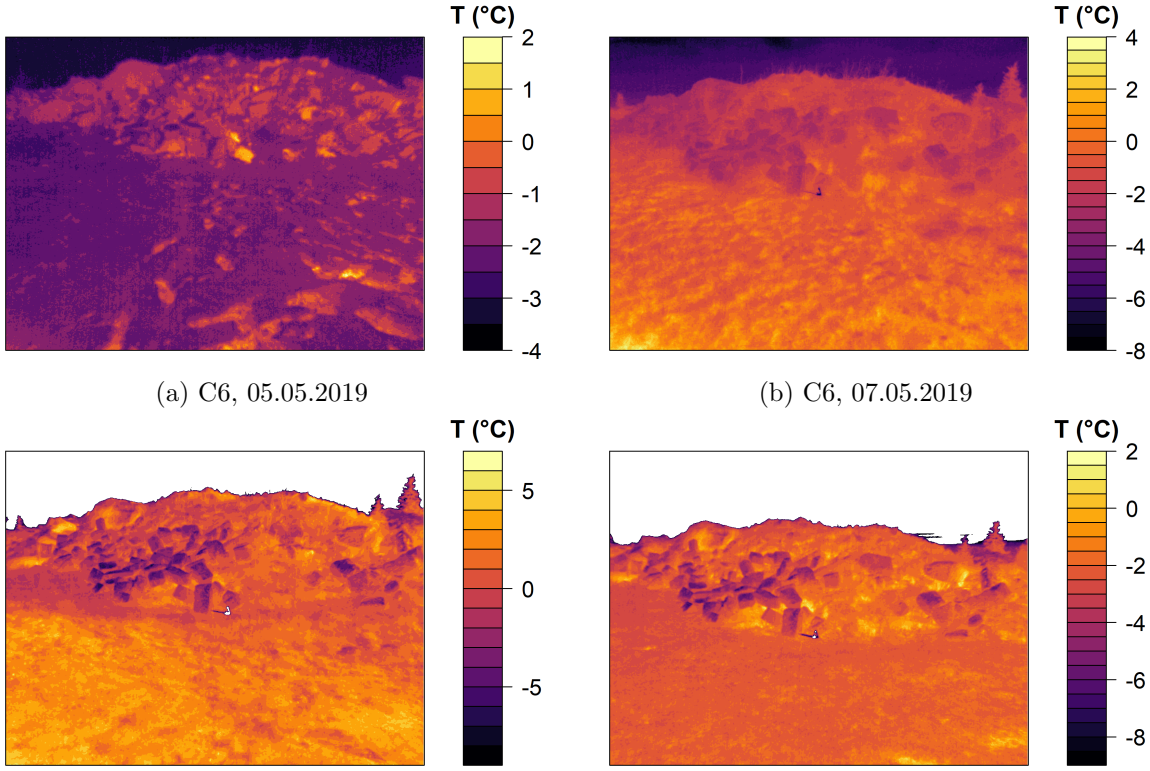

(a) C6, 05.05.2019

(b) C6, 07.05.2019

(c) C6, 14.05.2019

(d) C6, 15.05.2019

Figure C.2.: Surface brightness temperature $T_{surface}$ of the small anthropogenic block heap at Schneeberg summit on each measuring day, images taken at infrared camera location C6 using an emissivity of 0.95. White areas indicate temperatures outside of the range of the color bar.

Declaration of authorship

Hereby, I declare that I have authored the master thesis titled

"*Late-frost limitation of European beech*
in the Fichtelgebirge mid-range mountains, Germany"

independently and unaidedly based on my own work. All direct or indirect sources used are acknowledged as references. This thesis has not been published or previously submitted to any other examination board.

Location, date	Judith Eisenbacher